Design, Preparation and Characterization of Broad Spectral Response Photocatalysts

LI, Chuanhao

A Thesis Submitted in Partial Fulfillment

of the Requirements for the Degree of

Doctor of Philosophy

in

Chemistry

The Chinese University of Hong Kong

July 2011

ProQuest LLC.
789 East Eisenhower Parkway
P.O. Box 1346
Ann Arbor, MI 48106 - 1346

Thesis/Assessment Committee

Professor To NGAI (Chair)

Professor Jimmy C. M. YU (Thesis Supervisor)

Professor Quan LI (Committee Member)

Professor Shun-cheng LEE (External Examiner)

Professor Nianqiang WU (External Examiner)

Abstract

This thesis focuses on the fabrication of photocatalysts with responsive range in the visible light and near infrared regions. The preparation of small band gap semiconductor-sensitized TiO_2 with high visible-light photocatalytic activity has been investigated. Upconversion materials are used to extend the photoresponse into the NIR region.

The first chapter describes an effective method for the incorporation CdS and gold nanoparticles into highly ordered TiO_2 nanotube arrays (TNAs) by sonication. CdS severs as a visible-light photon acceptor. The absorption ability of CdS is further enhanced by gold nanoparticle due to the surface plasma-induced localized electromagnetic field enhancement effect. Compared with TNAs/CdS, the TNAs/CdS/Au composite exhibits higher photocatalytic activity under visible light irradiation.

Another study is the fabrication of a new visible-light photocatalyst by embedding Cu_2ZnSnS_4 (CZTS) nanocrystals into mesoporous TiO_2. TEM, EDX and XRD results confirm the formation of the composite. According to the UV-visible diffuse reflectance spectrum, the composite shows a broad absorption band in UV-visible region within 300 and 800 nm. The new material has high visible-light photocatalytic activity and excellent cyclability.

Because of their unique optical property to convert NIR to visible light, upconversion materials are promising candidates to realize NIR photocatalysis. A

facile self-assembly method has been developed to prepare nanoporous $NaYF_4$:Yb,Er upconversion single crystals with strong red emission peaks upon NIR excitation. The effects of reaction time and surfactant concentration on the porous structure were studied. And the upconversion luminescent properties for the obtained porous crystals have been investigated. The porous upconversion materials exhibited high ability to adsorb protein molecules. To demonstrate the potentials of this material, the energy transfer from porous $NaYF_4$:Yb, Er to chlorophylls and methylene blue were investigated.

Then a NIR photocatalyst was prepared by coupling a low energy band gap semiconductor CdS with an upconversion material $NaYF_4$: Yb, Tm. Particles of CdS and $NaYF_4$:Yb, Tm were pretreated with thioglycolic acid and mercaptoethanol. The reaction between these two organic molecules caused the formation of $NaYF_4$: Yb,Tm/CdS composite. Energy transfer from $NaYF_4$: Yb,Tm to CdS was confirmed by the upconversion and fluorescence decay properties. Hydroxyl radicals were generated upon NIR irradiation on the composite material. The NIR photocatalytic activity of the $NaYF_4$: Yb,Tm/CdS composite was investigated by degrading Rhodamine B and methylene blue. A mechanism for NIR-driven photocatalysis was proposed.

摘要

本學位論文主要探討了具有可見光和近紅外光回應的光催化材料的製備。窄帶半導體敏化的二氧化鈦具有很高可見光催化活性。上轉換材料被用於將光催化回應延伸至近紅外光區。

第一章介紹了一種利用超聲將硫化鎘和金納米顆粒引入到高度有序的二氧化鈦納米管陣列中的方法。作為一種窄帶半導體，硫化鎘可以俘獲可見光子。金納米顆粒所引起的表面等離子體共振吸收，使得硫化鎘表面局域電磁場增強，最終使得硫化鎘的吸收可見光的能力增強，產生更多的光生電子-空穴對。實驗證明，相對二氧化鈦陣列/硫化鎘體系，二氧化鈦陣列/硫化鎘/金的複合材料具有更高的可見光催化活性。

另一項研究是將硫化銅鋅錫納米晶嵌入到介孔二氧化鈦中，以製備高活性的可見光催化劑。透射電子顯微鏡，電子能譜和 X-射線衍射結果證實了複合物的形成。根據紫外-可見漫反射光譜，所製備的複合材料在紫外-可見光區從 300 到 800 nm 範圍內有很強的吸收帶。這種新材料具有較高的可見光催化活性和良好的重複使用的性能。

由於其獨特的可將近紅外光轉換成可見光的光學特性，上轉換材料可用於實現近紅外光催化。首先我們介紹了一種簡便的通過自組裝方法製備納米多孔上轉換 $NaYF_4$：Yb, Er 的方法。研究表明，反應時間和表面活性劑濃度對產物形貌和孔結構具有很重要的影響，所獲得的多孔晶體在近紅外光激發下可以發射較強的紅光。這種多孔上轉換材料對蛋白質分子具有很強的吸附能力。在近紅外光激發下，這種材料所輻射出來的能量可被傳遞到亞甲基藍和

葉綠素分子上，為實現近紅外光動力療法和近紅外光合作用提供了一定的理論依據。

第四章討論了一種新型的近紅外光驅動的光催化劑。這種催化劑由上轉換材料 $NaYF_4$:Yb, Tm 和硫化鎘複合而成。首先，$NaYF_4$:Yb, Tm 表面被巰基乙醇修飾，硫化鎘被巰基乙酸修飾。然後巰基乙醇和巰基乙酸之間的反應將兩者結合成複合材料。上轉換光譜和時間分辨光譜證實了從 $NaYF_4$:Yb,Tm 到硫化鎘之間的能量傳遞。在近紅外光照射下，此複合材料可以產生羥基自由基，對羅丹明 B 和亞甲基藍具有一定的降解作用，此外我們還提出了近紅外光催化機理。

Acknowledgement

This dissertation was made possible by the help and support of many people. First of all, I would like to express my sincere gratitude and appreciation to my supervisor, Prof. Jimmy C. Yu, for providing me with this unique research opportunity, and for his expert guidance and support all the way in my 3-year period of study and preparation of this thesis. Throughout my study and research project, he has constantly given me insightful advice. I have not only learnt a lot from him but have also been inspired by his dedicated attitude to science. I am also deeply impressed by his profound knowledge in research. I shall benefit from this experience in my future work and life. It has been a truly wonderful learning experience.

My heartfelt thanks must also go to Prof. Jiangfang Wang, Dr. Xianfeng Yang, Dr. Huanjun Chen, Dr. Xianluo Hu, Dr. Guisheng Li and Dr. Dieqing Zhang for their helpful discussions. Their constructive comments were essential to the completion of this dissertation. I am also grateful to Mr. Man Hau Yueng for his HRTEM analysis. I am also indebted to Prof. Kok Wai Cheah and Dr. King Fai Li for their valuable help in the life time measurement. Thanks to Dr. Wing Kei Ho and Dr. Jianhui Huang for UV-vis reflectance spectra measurements. Thank you to all the subjects who have dedicated their valuable time and effort, without whom this study could not have been possible.

My sincere thanks are also extended to my groupmates for their generous help, support and encouragement. They have made my Ph.D. life so fantastic and provided me an enjoyable environment in which to work. I would like to acknowledge all the staff members in the Department of Chemistry for the contribution to an active academic atmosphere. In addition, this research work was made possible by the generous financial support of the Research Grants Council of Hong Kong.

Lastly, and most importantly, I feel very grateful to my parents and my love, Tingting for their unconditional love, concern, support and patience for the pursuit of my Ph.D. They are the source of my motivation and happiness. Thanks must also go to all my friends, who have constantly offered me words of encouragement. Thank you for always being there for me. You all have helped to make my Ph.D. study inspiring and rewarding.

May 2011

List of Figures

porous particles before (A) and after (B) BSA treatment. The porous products used in all measurements are prepared at 160°C, 3h (SDS 10mM).

Figure 4.11 (a) Room temperature upconversion emission spectrum of $NaYF_4$:Yb, Er particles in ethanol (5 mg/mL) upon 976 nm NIR excitation and (b) absorption spectrum of chlorophylls.

Figure 4.12 (a) Room temperature upconversion fluorescence spectra of the $NaYF_4$:Yb,Er ethanol suspension (1mL, 5mg/mL) with the addition of different volume of original chlorophylls. A-Q: 0, 50, 100, 150, 200, 250, 300, 350, 400, 450, 500, 600, 700, 800, 900, 1000, 2000 μL, respectively. (b) Magnified spectra of Figure 4.12a. (c) The first-order plots for the upconversion emission intensity located at 660 nm and the volume of substance added. A-D: original, ×1/2, ×1/5 chlorophylls and pure ethanol, respectively. I_0 is the intensity at 660nm of the original upconversion suspension. I is the intensity after adding corresponding substance. (d) Room temperature upconversion fluorescent spectra of A) the original chlorophylls solution, B) two-times dilution, C) five-times dilution.

Figure 4.13 Schematic illustration of FRET mechanism from upconversion materials to chlorophylls upon 976 nm NIR irradiation.

Figure 4.14 (a) Room temperature upconversion emission spectrum of $NaYF_4$:Yb, Er particles in ethanol (5 mg/mL) upon 976 nm NIR excitation and absorption spectrum of MB (40ppm). (b) Room temperature upconversion fluorescence spectra of the $NaYF_4$:Yb,Er ethanol suspension (1mL, 5mg/mL) with the addition

of different volume of MB (40ppm). A-G: 0, 50, 100, 150, 200, 400, 800 μL, respectively. (c) The first-order plots for the upconversion emission intensity located at 660 nm and the volume of MB added.

Figure 5.1 Strategy for the preparation of $NaYF_4$: Yb,Tm/CdS composite.

Figure 5.2 SEM (a, b, d, e, f), TEM (c, g, h, i) images and pictures (j, k) of the products. (a-c): pure $NaYF_4$: Yb,Tm (d-i): $NaYF_4$: Yb,Tm/CdS composite. Figure h and i are the corresponding high-resolution TEM images from the areas outlined by the rectangles marked in (g). Pictures show the colors of (j) pure $NaYF_4$: Yb,Tm and (k) $NaYF_4$: Yb,Tm/CdS.

Figure 5.3 SEM images of the products obtained from control experiments without surface modification.

Figure 5.4 EDX line scan profiles (a) and TEM (b) image of the $NaYF_4$: Yb,Tm/CdS composite. Points A, B and C in (a) are corresponding to the same points shown in (b). In Figure (a), Y, Cd, and S data are plotted as blue triangles, red dots, and black rectangles, respectively.

Figure 5.5 XRD pattern of the prepared $NaYF_4$: Yb,Tm/ CdS composite

Figure 5.6 (a) (A)-Upconversion emission spectrum of $NaYF_4$: Yb,Tm and (B)-absorption spectrum of CdS. (b, c) Upconversion emission spectra of (A)-$NaYF_4$: Yb,Tm and (B)-$NaYF_4$: Yb,Tm/CdS. (c) is the magnified spectrum of (b). (d) Time-resolved fluorescence decay curves of Tm^{3+} (λ_{em}= 476 nm) of (A)-$NaYF_4$: Yb,Tm and (B)-$NaYF_4$: Yb,Tm/CdS. All the upconversion emission

spectra were recorded upon 976 nm NIR excitation.

Figure 5.7 (a) Reaction between the formed OH radicals and probe molecules, terephthalic acid. (b) Time-dependent fluorescence spectra of the terephthalic acid solution ($4*10^{-4}$M) containing 20 mg of $NaYF_4$: Yb,Tm/CdS composite upon NIR irradiation. (c) Fluorescence intensity of the emission peak at 420nm as a function of NIR irradiation time.

Figure 5.8 Time-dependent absorption spectra of Rhodamine B (a) and methylene blue (c) solution containing $NaYF_4$: Yb,Tm/CdS composite upon NIR irradiation. Rhodamine B (b) and methylene blue (d) reduction in UV-vis absorption spectra at 550 nm as a function of NIR irradiation time for different samples.

Figure 5.9 (a) Time-dependent absorption spectra of a 50 ppm Rhodamine B solution containing NaYF4: Yb, Tm/CdS composite upon visible-light irradiation. (b) Photocatalytic degradation of Rhodamine B as a function of visible-light irradiation time.

Figure 5.10 SEM (a) and TEM (b) images of the $NaYF_4$: Yb,Tm/CdS composite after NIR photocatalysis (3h).

Figure 5.11 Schematic illustration of energy transfer mechanism from $NaYF_4$: Yb,Tm to CdS upon 976 nm NIR irradiation.

List of Tables

Table of Contents

Chapter One

Introduction

1.1 Semiconductor-mediated photocatalysis

A rapid increase in human population and global economic development require more and more energy. Almost 90% of the world's energy that we rely on is the non-renewable fossil fuel such as oil, petroleum and natural gas. The consumption of fossil fuels generates a large amount of air pollutants and greenhouse gases. Chemical waste is another pressing issue. It is reported that the yearly consumption of organic dyes and pigments is over 0.7 million tons on a global scale, mainly for use in the textile, industrial painting, food, plastics, cosmetics, and consumer electronic sectors.[1] A significant fraction of the discharge from the above industries is disposed on the land and water each year. This causes serious environmental problems.[2]

To address the problems, many approaches have been developed. The most conventional methods are related to physical processes such as adsorption by activated carbon and ultrafiltration.[1] These non-destructive approaches can only transfer pollutants from one phase to the other one, such as from aqueous to adsorbent. Another common approach is biodegradation, a time consuming process. Meanwhile it can't be used to degrade all kinds of organic pollutants. In

industry some methods have already been used to decompose the hazardous chemical wastes such as high temperature incineration, anaerobic digestion. However, these methods consumed too much energy.

Semiconductor-mediated photocatalysis is an attractive environmental remediation technology to treat pollutants both in gas and in liquid phase because it makes use of the clean, safe, and renewable sunlight to solve environmental problems.[3-5]

The general mechanism of photocatalysis is well established and briefly summarized in the following process as shown in Figure 1.1: [3-6]

For a semiconductor photocatalyst, there is a filled valence band with lower energy, and an empty conduction band with higher energy. The energy between these two bands is called the band gap energy (Eg). When a photon with an energy of hv matches or exceeds the band gap energy (Eg) of the semiconductor, an electron in the valence band (VB) is excited into the conduction band (CB), leaving a positive hole in VB. Both reductive and oxidative processes can occur at/or near the surface of the photoexcited semiconductor particle.

The electron can reduce appropriate electron acceptors molecules. In aerated aqueous suspensions, oxygen can capture electrons to form superoxide ions ($O_2^{\bullet -}$) and hydroperoxyl radical ($HO_2^{\bullet}$):[3-8]

$$O_2 + e^- \rightarrow O_2^{\bullet -} \quad (1)$$

$$O_2^{\bullet -} + H^+ \rightarrow HO_2^{\bullet} \quad (2)$$

The positively charged holes oxidize appropriate donor molecules (D), such as water and hydroxide molecules to give hydroxyl radicals:

$$H_2O + h^+ \rightarrow HO\bullet + H^+ \quad (3)$$

The whole process ends up with the complete mineralization of organic compounds.

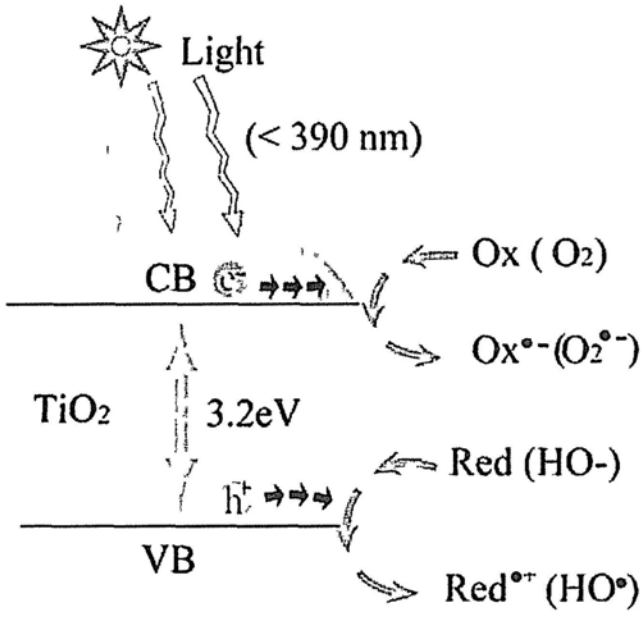

Figure 1.1 Photoexcitation of a semiconductor (e.g., TiO_2) and the subsequent generation of an electron and hole, which are trapped by an oxidant (Ox) and a reductant (Red), respectively. For TiO_2 photocatalysis, the "Ox" is a surface-adsorbed oxygen molecule, and the "Red" is a surface-bound hydroxyl group.[6]

During the past decade, the scientific and engineering interests in the

application of semiconductor photocatalysis have grown rapidly and have drawn from a number of scientific disciplines Researchers have focused much effort to develop solar energy-driven photocatalyst to solve environmental problems.

Figure 1.2 shows the whole solar spectrum. Solar energy mainly distributed in ultraviolet light (UV, 4%), visible light (46%) and infrared light (IR, 47%). To more efficiently use solar energy for photocatalysis, the evolution of photocatalysts can be divided into three stages. In the very beginning, researcher focused on investigating UV light-driven photocatalyst and developed various strategies to improve photocatalytic activity. Then much progress has been made to extend photocatalysis response to visible light. Very recently NIR-driven photocatalysis has been reported.

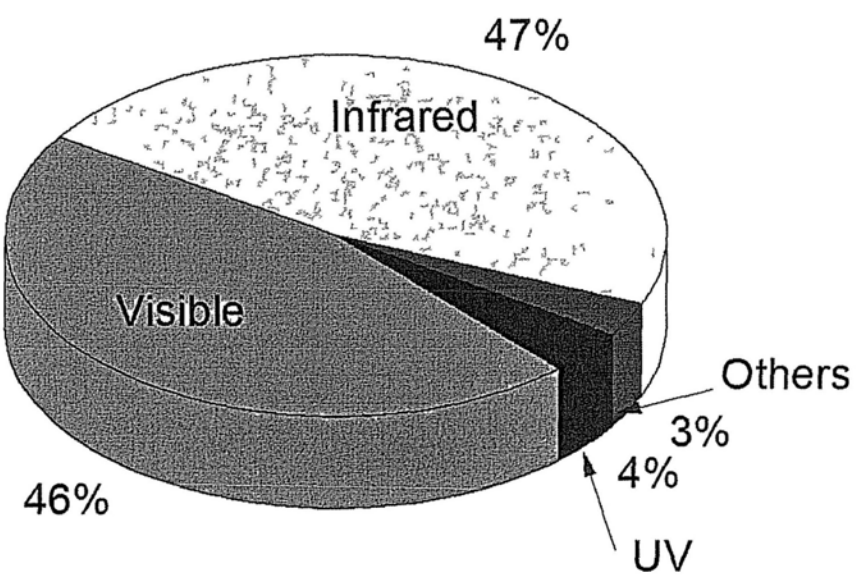

Figure 1.2 Solar energy distributions

1.2 UV light photocatalyst

In 1972, Fujishima and Honda achieved ultraviolet (UV) light induced water cleavage using a titanium dioxide photoanode in combination with a platinum counter electrode soaked in an electrolyte aqueous solution.[9] Since then TiO_2 has been widely studied as an efficient photocatalyst because of its appropriate electronic band structure, strong oxidizing power, photostability, chemical inertness, and commercial availability.[10-14] Various strategies have been applied to improve the photocatalytic efficiency, such as surface modification,[15-17] developing porous materials,[10, 18, 19] constructing one-dimensional structure and so on.[20-22]

1.2.1 Surface modification

As discussed above, photocatalytic activity is highly dependent on the lifetime of the electron-hole pairs. If it is too short, the photogenerated electrons and holes recombine and dissipate the input energy as heat very quickly, which is the main problem that limits the photocatalysis efficiency. Various approaches have been developed to inhibit the recombination. A promising solution is to derivatize the surface of semiconductor with some trapping materials to inhibit the recombination. Various organic molecules having functional groups including hydroxyl, carboxyl, silanyl, phosphonate groups have been demonstrated as efficient trapping molecules.[8, 23] For example, enhanced photoreduction of lead

ions was observed by using cysteine modified TiO_2 nanoparticles in the study of Rajh et al.[24] The proposed mechanism is shown in Figure 1.3. For unmodified TiO_2, upon excitation, photogenerated electrons were trapped at metal centers as Ti (III), while the holes were trapped on the surface OH groups as a $(TiO_2)_nTi^{IV}O^{\cdot}$. Recombination of electrons and holes occurred easily as the separation distance was short. However, in the case of cysteine-modified TiO_2, the holes were trapped on cysteine to form carboxyl radical, while the electrons were trapped on the TiO_2 particle. The resulting increased separation distance inhibited the electron/hole recombination.

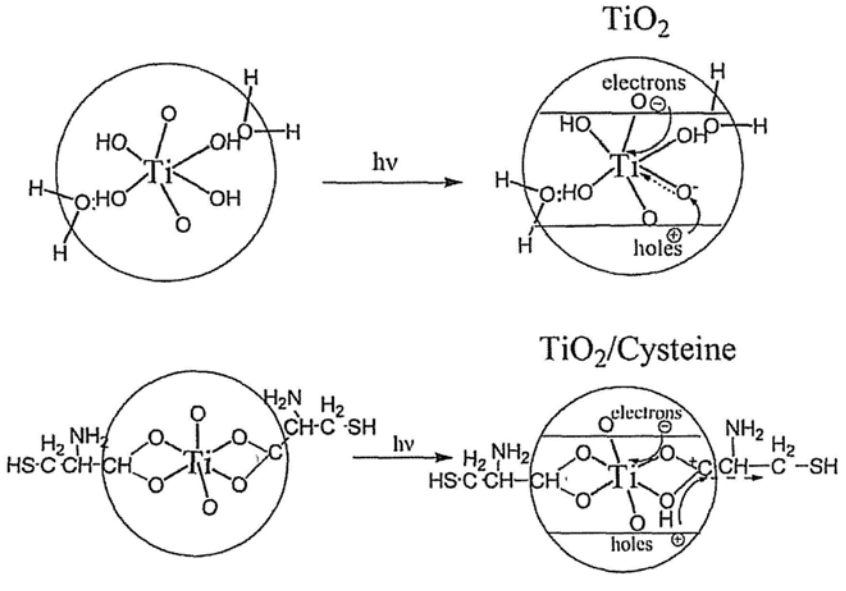

Figure 1.3 Schematic presentation of structure and electron transfer reactions in (a) TiO_2, (b) TiO_2/Cysteine.[24]

1.2.2 Porous structure

After excitation, the formed electron-hole pairs migrate to the semiconductor surface. The electrons and holes are thought to induce various redox processes at the semiconductor/solution interface. It is reasonable that large surface area will be beneficial for the contact between the holes (or electrons) and the pollutant molecules. Thus increasing the surface area is another promising method to enhance photocatalytic activity.[8]

Based on the well known fact that the specific surface area increase dramatically as the size of a material decreases, ultrafine TiO_2 nanocrystals have been widely studied. Compared with the bulk materials, TiO_2 nanocrystals have larger surface area and much higher photocatalytic activity.

Introducing porosity in photocatalyst has been proven as an effective method to enhance photocatalytic activity. The enhancement is attributed to two aspects: (a) a high density of active centers for photocatalytic reactions, (2) an enhanced light harvesting because of light reflection and scattering in the pores.[25]

The sacrificial template strategy has been widely used to fabricate porous photocatalysts. Based on the nature of the templates, two general approaches are involved: the hard and soft templates. Silica, metal oxide, carbons, alumina, cellulose fibers etc., all have been widely used as hard templates.[25] The typical soft templates are some single organic molecules and surfactant micelles. After

removing the templates by appropriate solvent or calcination, a porous photocatalyst is obtained. For example, poly(alkyleneoxide) block copolymer, (abbreviated as Pluronic F-127, BASF) has been widely used as soft templates to prepare porous TiO_2-based materials.[26]

1.2.3 One dimensional nanostructure

For the conventional TiO_2 nanoparticles the electron transport time constants are very low. Such low electron diffusion coefficients within is due to defects, surface states, grain boundaries etc. that act as electron trapping sites, thus slowing down electron flow, enhancing recombination.[27, 28]

In order to overcome this issue, recently research has been focused on the use of one-dimensional nanostructures of TiO_2, such as, nanotubes, nanorods, nanowires. Especially, the highly ordered TiO_2 nanotube arrays (TNAs) synthesized by anodic oxidation of titanium had generated considerable scientific interests. Compared with random nanoparticle systems, the precisely oriented nature of the crystalline nanotube arrays could improve the electron transport properties because of a directional smooth electron mobility (limiting random walk in the wide nanocrystalline network) and decreased intercrystalline contacts (accelerating electron transport and lowering the recombination probability). Furthermore, the TNAs with high surface area provide more opportunities to harvest sunlight for energy conversion or photodegradation.[27]

As initially reported by Zwilling and co-workers in 1999, the first generation titania nanotube arrays fabricated by anodizing a Ti-based alloy in an aqueous HF based electrolyte could reach a length of about 500 nm.[29] Then in the subsequent work, the nanotube array length was increased to even 1000μm by using a non-aqueous, polar organic electrolyte such as formamide, dimethylsulfoxide and ethylene glycol.[30-34]

The growth mechanism has also been widely studied. As shown in Figure 1.4, it involves four steps:[30-34]

(1) Metal atoms at the surface were oxidized by O_2 or OH^- ions to form an initial oxide layer (Figure 1.4a). The overall reactions for the formation of titanium oxide can be shown as:

$$2H_2O \rightarrow O_2 + 4e + 4H^+$$

$$Ti + O_2 \rightarrow TiO_2$$

(2) Small pits are formed due to the localized dissolution of the oxide (Figure 1.4b), represented by the following reaction.

$$TiO_2 + 6F^- + 4H^+ \rightarrow TiF_6^{2-} + 2H_2O$$

(3) The electric field intensity across the remaining barrier layer is increased due to the formation of the small pits, resulting in the growth of the small pits into bigger pores (Figure 1.4c).

(4) As the pores become deeper, the electric field in these protruded metallic

regions increases. The field-assisted oxide growth and oxide dissolution is further enhanced. As a result, the nanotube arrays formed (Figure 1.4d, e).

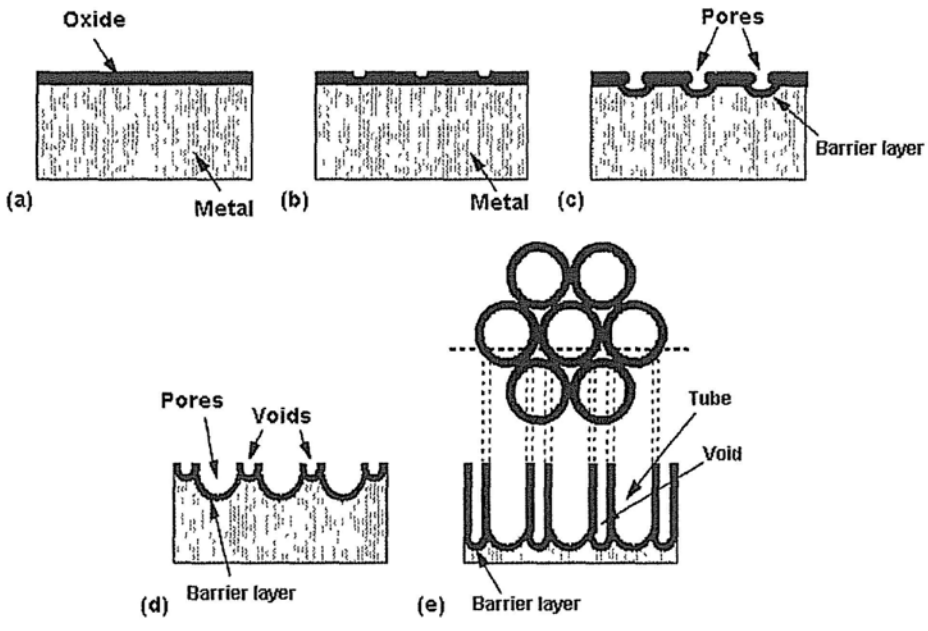

Figure 1.4 Schematic diagram of the evolution of a nanotube array at constant anodization voltage: (a) oxide layer formation, (b) pit formation on the oxide layer, (c) growth of the pit into scallop shaped pores, (d) metallic part between the pores undergoes oxidation and field assisted dissolution, and (e) fully developed nanotube array with a corresponding top view.[28]

It has been shown that TNAs exhibit higher photocatalytic activity than comparable nanoparticle. This photocatalytic activity can be further enhanced by applying an external bias.[35] The unique properties make TNAs excellent candidates for various applications, such as dye-sensitized solar cells, gas sensors, photocatalysts, water-splitting catalysts for hydrogen generation, and so forth.[36]

1.3 Visible light photocatalyst

TiO_2 exhibits high photocatalytic, deodorizing, antibacterial and self-cleaning properties under UV illumination. Due to the large band gap, pristine anatase and rutile TiO_2 photocatalysts can only be activated by ultraviolet photons. However UV only occupies about 4% of the solar spectrum. To more efficiently use the solar energy, great attention has been paid to the development of visible-light-induced photocatalysts, which are able to operate effectively not only under UV but also under the most environmentally ideal energy source, sunlight.

Various approaches have been developed to extend the response of photocatalysts into the visible light region. These include doping metallic and nonmetallic elements in conventional photocatalysts to decrease the band gap to accommodate the visible light photon energy,[37-40] directly using some low band gap semiconductors as novel photocatalysts,[41-44] fabricating composite semiconductors.[45-48]

1.3.1 Metal and non-metal doping

The optical response of a photocatalyst is largely dependent on its underlying electronic structure which is related to its chemical composition, atomic arrangement, and physical dimension. For TiO_2, both the metal (titanium) and the nonmetal (oxygen) component can be replaced to alter its optical properties.[3, 5]

To maintain the integrity of the crystal structure, various transition metals have

been doped into TiO_2 to substitute the Ti^{4+} cations. The dopant cations create intermediate states between the CB and VB of TiO_2, which induce visible light absorption at the sub-bandgap energies. Figure 1.5 presents a typical mechanism for the absorption of visible light for metal-doped TiO_2.[49] When TiO_2 was doped with V, a V t_{2g} level formed. The visible light absorption for the V-doped TiO_2 can be due to a donor transition from the V t_{2g} level into the CB and the acceptor transition from the VB to the V t_{2g} level. Many metal dopants involving Ag, Cr, Al, Fe, Au, Mn, Ni have been studied.[49]

Non-metal dopants including C,[50] N,[51] S,[39] F[37] can also create intra-band-gap states close to the VB edges. For example, Asahi et al reported the good visible photocatalytic activity of N-doped TiO_2 films.[52] They found that nitrogen atoms substituted the lattice oxygen sites and narrowed the band gap by mixing the N_{2p} and O_{2p} states.

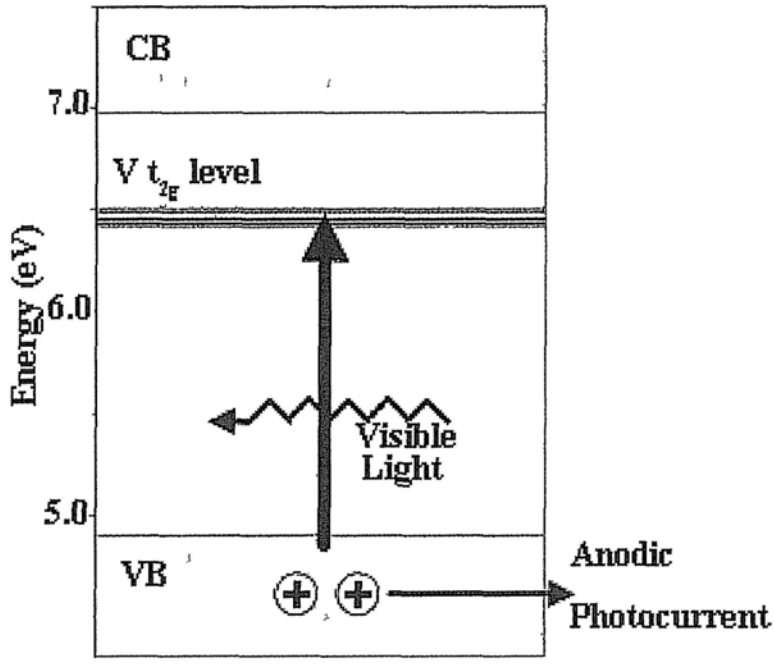

Figure 1.5 Schematic diagram to illustrate the photoexcitation process under visible light of the V-doped TiO_2[49]

1.3.2 Low band gap semiconductor photocatalysts

Another approach to extend photoresponse to visible light is to use low band gap semiconductors. There are at least two requirements to employ such semiconductors as visible light photocatalysts. Firstly, the band gap energy should be lower than 3.1eV to capture visible light photons. Also the chemical potential of VB and CB should be at a suitable position so that they are powerful to oxide or reduce pollutant molecules. Based on these factors, many kinds of low band gap photocatalysts have been developed. Figure 1.6 shows several widely studied

visible light-driven photocatalysts.

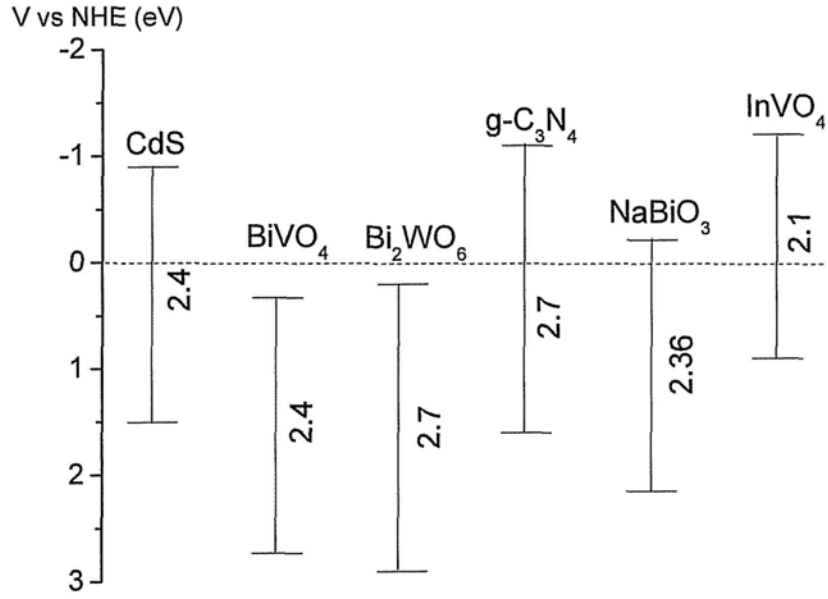

Figure 1.6 Band position of selective visible light photocatalyst[46, 53-57]

Metal sulfides are very attractive visible light photocatalysts due to their narrow band gaps with valence bands at relatively negative potentials. CdS is well-known visible light photocatalyst. Various methods have been developed to prepare CdS-based photocatalyst, such as solution precipitation,[58] chemical vapor deposition,[59] hydrothermal[60] and photochemical methods.[61] Size and morphology-dependent photocatalytic activity were widely investigated. In addition to the higher photocatalytic activity, CdS has also shown good activity for visible light photocatalytic hydrogen production.[62]

However, for CdS the separation efficiency of the electron-hole pair is very low. Moreover, the photostability of CdS is very poor.[63] Under strong UV or visible

light irradiation, CdS is prone to photoerosion because CdS itself could be oxidized by the photogenerated holes to release Cd^{2+}. Thus the photocatalytic activity could not be repeated for many times. And the released Cd^{2+} ions cause environmental issues. Surface modification is a common approach to overcome these problems. It has been reported that polyaniline modified CdS show enhanced visible light photocatalytic activity and anti-photoerosion performance.[64] Upon visible light irradiation, the photogenerated holes in the valence band of CdS were transferred to polyaniline on the photocatalysts surface. The improved separation efficiency of electron-hole pairs leads to higher photoactivity and excellent anti-photocorrosion property.[64]

Although some metal sulfide semiconductors have very low bandgap and high absorption coefficient, they are not good photocatalysts. For example, the bandgap of Cu_2ZnSnS_4 (CZTS) is only about 1.5eV and its absorption coefficient is very large ($>10^4$ cm^{-1}).[65, 66] However it can not be directly used as photocatalyst because of high recombination efficiency.

1.3.3 Composite semiconductors

There are drawbacks for the single low bandgap semiconductor photocatalyst, such as narrow-spectrum response and photoerosion. Many researchers focus their efforts on the design and development of composite photocatalysts composed of a large and a low band gap semiconductor. A typical example is TiO_2/CdS

composite. Figure 1.7 shows the general mechanism for the charge-transfer process involved in the TiO_2/CdS composite.[67] CdS is low bandgap semiconductor, which can be activated by visible light. The conduction band of TiO_2 is less negative than that of CdS. Thus under visible light irradiation the photogenerated electrons on the conduction band of CdS are quickly injected into that of TiO_2. As a result more efficient charge-carrier separation can be achieved, resulting in improved photocatalytic activity.

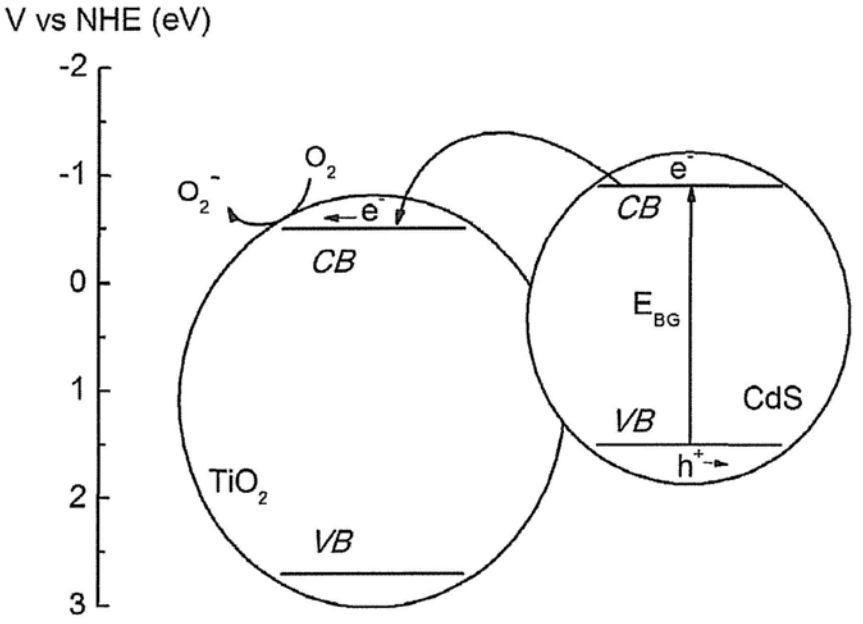

Figure 1.7 Schematic diagram to illustrate the mechanism of visible light photocatalysis for TiO_2/CdS composite[67]

To prepare the composite photocatalysts, various approaches have been developed. Li et al synthesized CdS quantum dots sensitized ordered mesoporous

TiO_2 by planting CdO as a seed into the TiO_2 network and then converting it to CdS by ion-exchange at room temperature.[46] TiO_2@CdS core-shell nanorods films have been fabricated by using a simple and low-cost chemical bath deposition method.[68] As described above TNAs exhibit higher photocatalytic activity. Thus decoration of TNAs with CdS nanoparticles has been widely used to fabricate visible light photocatalyst by using sonication-assisted synthesis[69] or electrochemical methods[70].

Furthermore CdSe,[45] MoS_2,[71] and WS_2[71]-sensitized TiO_2 nanoparticles have been synthesized by ultrasound-driven, in situ photoreduction deposition and microemulsion-mediated solvothermal methods.

1.4 Near infrared-driven photocatalyst

The whole solar energy spectrum includes near infrared (NIR, 44%), visible (47%), and UV (4%) light. Previous studies have been mainly focused on the utilization of UV and visible light for photocatalysis. However, the utilization of NIR which constitutes almost half of the solar spectrum is still a formidable task.

Near infrared (NIR) light is electromagnetic radiation with a wavelength starting from the nominal edge of visible red light at 700nm, and extending conventionally to 1.4μm. Due to the relatively low photon energy (lower than 1.7eV), NIR can not be directly captured by conventional semiconductors.

Recently researchers have noticed the importance of NIR in solar applications.

Considerable attention has been focused on the preparation of some special organic dyes whose absorption extends to NIR. For example, Vasseur et al used lead phthalocyanine (PbPc) films to construct solar cell.[72] PbPc films exhibit an strong NIR absorption peak at a wavelength of λ=900 nm. Thus the solar conversion response is extended to NIR region. Various organic dyes with NIR absorbing ability have been synthesized for dye-sensitized solar cells.[73-75] However due to the poor stability these organic dyes are not suitable for photocatalysis. They could be decomposed by the photogenerated free radicals. Thus NIR-driven photocatalysis for pollutant degradation has not been reported before.

Recently great progress has been made in the preparation of upconversion materials which can emit visible or UV light by absorbing two or more near-infrared (NIR) photons.[76, 77] The unique optical properties and excellent stability make it possible to combine upconversion materials with conventional photocatalysts to realize NIR-driven photocatalysis.

1.4.1 Upconversion materials

Together with second harmonic generation (SHG)[78, 79] and two-photon absorption (TPA)[80, 81], upconversion is one of the most widely studied nonlinear optical processes which convert long-wavelength excitation photons into shorter wavelength output photons.[76, 77, 82] However unlike SHG and TPA, upconversion

is based on the existence of at least two metastable intermediate states as shown in Figure 1.8. [82] Thus compared with SHG and TPA, upconversion is more efficient.

1.4.1.1 Upconversion mechanism

A variety of different UC mechanisms have been established. Most of them involve absorption and nonradiative energy transfer steps. The three well know ones are shown in Figure 1.8.[76, 77, 82]

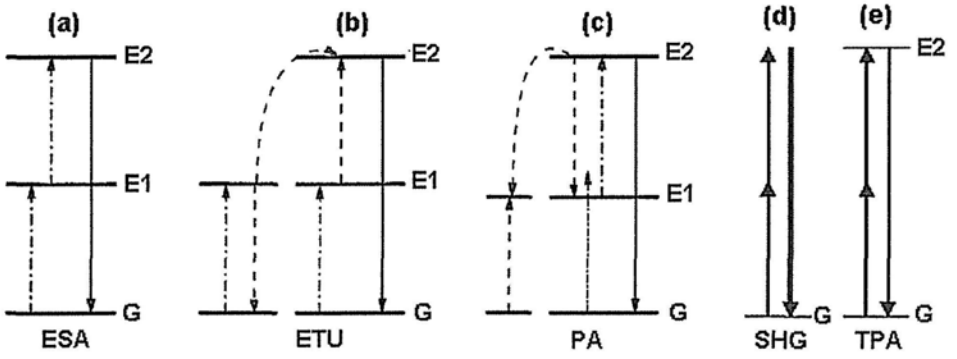

Figure 1.8 Energy schemes for different two photon luminescence processes: (a) excited state absorption (ESA), (b) energy transfer upconversion (ETU), (c) photon avalanche (PA). (d) second Harmonic Generation (SHG) and (f) two photon absorption (TPA).[76, 77]

The simplest one is the excited state absorption (ESA, Figure 1.8a).[77] The process is caused by the successive absorption of pump photons in a single ion. When excitation energy satisfies the transition from ground level G to excited metastable level E1, an ion will be promoted from G to E1 state. It is called

ground state absorption (GSA). Subsequently, a second photon further promotes the ion to the higher-lying excited state E2, resulting in upconversion emission.

Energy transfer upconversion (ETU) is another mechanism.[77] Similar to ESA, ETU also involves the sequential absorption of two photons. However ETU is a cooperative process between two neighboring ions. As shown in Figure 1.8b, GSA generates two ions in their E1 states. Then the non-radiative energy transfer promotes one of the ions to E2 state, while the donor ion relaxes back to G state.

Photon avalanche (PA) phenomenon was first reported by Chivian in Pr^{3+}-based materials.[83] PA-induced upconversion requires a pump intensity above a certain threshold value. Figure 1.8c shows the general energy diagram of the PA process. A non-resonant weak GSA process populates a E1 state, followed by the generation of E2 state by a resonant ESA. Then a cross-relaxation energy transfer from the excited ion in E2 state to a neighboring ground state ion populates two ions in E1 states. The two ions could further populate level E2 to initiate cross-relaxation by ESA. So the amount of ions in E2 states exponentially increased, producing strong UC emission as an avalanche process.

The upconversion efficiency in the three processes is as the following order: PA>ETU>ESA. Although PA is the most efficient one, its disadvantages are also obvious, including pump power dependence and slow response to excitation. ETU is instant and pump power independent. Compared with ESA, ETU is two orders of magnitude higher in efficiency. Thus ETU has been widely used to offer highly

efficient upconversion in the past decade.

1.4.1.2 Requirements for upconversion

The typical upconversion materials are composed of the crystalline host and rare earth dopants. The most efficient upconversion materials are rare earth co-doped materials, including three parts: host crystal, activator and sensitizer.

Host crystals provide space for upconversion. The selection of host material is based on two considerations.[84] The first requirement is close atomic size and lattice to the dopant ions. This is to make sure that the dopant ions experience the same environment to minimize crystal defect which could inhibit the upconversion efficiency.[76, 77] As all trivalent rare earth ions exhibit similar ionic size and chemical properties, their inorganic compounds are ideal host materials.

The other requirement is that host materials should have low lattice phonon energy.[76, 77] Phonons represent energy propagation in the lattice through atomic vibrations. Phonon energy can interact with the electronic states of an atom. Thus the amount of ions in high energy states decreased, resulting in low upconversion efficiency. Heavy halides including chlorides, bromides and iodides have low phonon energies less than 300 cm^{-1}, but they are hygroscopic. Oxides exhibit high stability. However their photon energies are higher than 500cm^{-1}. The relatively low photon energies and high chemical stability make fluorides excellent host materials for upconversion.[85, 86] It have been widely accepted that $NaYF_4$ is the best host material for upconversion.[87-89]

It has been reported that co-doped upconversion materials show higher efficiency than singly doped upconversion materials. In co-doped upconversion materials, the role of sensitizer is to absorb NIR light. To enhance upconversion efficiency, a sensitizer should exhibit high absorption cross-section in the NIR region. And the energy level of the sensitizer must be close to the activator ions to realize ETU process between the two ones. Trivalent Yb has only one excited 4f level of $2F_{5/2}$ which corresponds to the absorption band around 980nm. And the absorption cross section is lager than the other lanthanide ions. Furthermore the $^2F_{7/2}$-$^2F_{5/2}$ transition of Yb^{3+} matches very well with many f–f transitions of typical upconverting lanthanide ions (Er^{3+}, Tm^{3+}, and Ho^{3+}). Thus Yb^{3+} is the common sensitizer used in upconversion materials. To enhance the absorbance the concentration of sensitizer should be higher than 20% and lower than 40% to minimize the back-transfers.[76, 77]

Activators that emit the radiation are the most important part in upconversion materials. According to the upconversion mechanisms, the basic requirement for activators is the metastable intermediate states. The lanthanides are enriched such metastable states because their 4f electrons are well shielded by the completed filled 5s and 5p sub-shells. The efficient shielding results in weak electron-phonon coupling that is responsible for the presence of various excited f-f states. And the lifetime of the metastable states are relatively long (up to 0.1 s). These unique properties allow the lanthanides to be excellent activator for upconversion

process.[76, 77]

1.4.1.3 Typical energy transfer in upconversion process

In the co-doped upconversion materials, ETU is the major process. To realize efficient energy transfer from sensitizer, the energy gaps of the activator should be close to those of sensitizers. Er^{3+}, Tm^{3+}, and Ho^{3+} with such ladder-like arranged energy levels are frequently used activators.

Figure 1.9 shows the appropriate energy level diagrams with the principal radiative and nonradiative processes for Yb/Er and Yb/Tm upconversion materials.[77] A typical upconversion mechanism for Yb/Tm system involves a multi-photon process through four successive energy-transfer steps as shown in the following part:

(1) A Yb^{3+} ion absorbs a 976nm NIR photon to be promoted to $^2F_{5/2}$ level. Then a Tm^{3+} ion is excited into the its $^3H_5$ level by energy transfer from the first excited Yb^{3+} ion, and then relaxes into its $^3F_4$ level;

(2) The Tm^{3+} could be further excited from $^3H_4$ to the $^3F_2$ level by capturing the energy released from the second excited Yb^{3+} ion. And then it relaxes to its $^3H_4$ level.

(3) The released excited energy from the third excited Yb^{3+} ion promote the Tm^{3+} ion to the $^1G_4$ state. Blue light is emitted when the Tm^{3+} drop back to its ground state. Also the red emission 650 nm when it relaxes into the $^3F_4$ state.

(4) The fourth excitation of Tm^{3+} generates the $^1D_2$ level. The relaxation from

$^1D_2$ to ground state also causes blue emission.

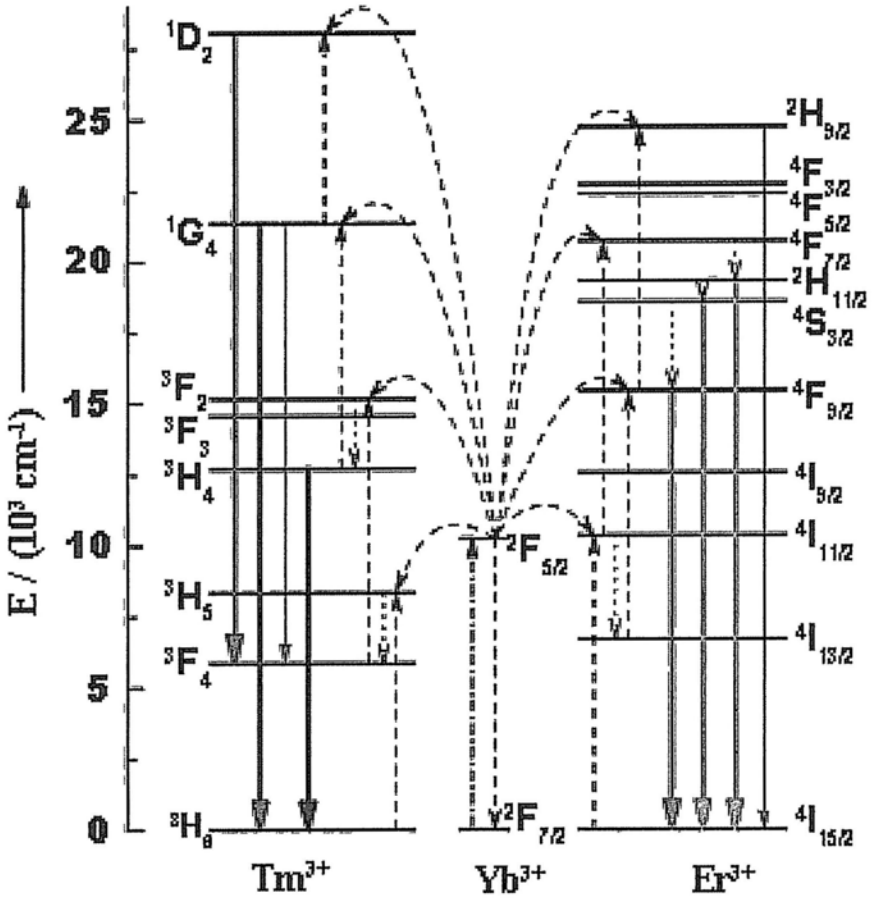

Figure 1.9 Proposed energy transfer mechanisms showing the UC processes in Er^{3+}, Tm^{3+}, and Yb^{3+} doped crystals under 980-nm diode laser excitation.[77] The dashed-dotted, dashed, dotted, and full arrows represent photon excitation, energy transfer, multiphonon relaxation, and emission processes, respectively. Only visible and NIR emissions are shown here.

1.4.2 $NaYF_4$-based highly efficient upconversion materials

The trivalent Y^{3+} exhibits close atomic size to rare earth elements. And the phonon energy of $NaYF_4$ is lower than $500cm^{-1}$.[77] Thus $NaYF_4$-based upconversion materials have been widely considered as the most efficient upconversion materials.[87-89] For example, the green emission of $NaYF_4$;Yb, Er and blue emission of $NaYF_4$:Yb, Tm are visual by naked eyes under very weak 980nm NIR irradiation.

The efficiency of $NaYF_4$-based upconversion materials is phase-dependent. According to the previous reports, hexagonal phase (β-phase) $NaYF_4$ offers about an order-of magnitude enhancement of upconversion efficiency relative to its cubic phase (α-phase) counterpart.[90-94] As shown in Figure 1.10, the phase-dependent property is due to the different crystal-fields around trivalent lanthanide ions in matrices of various symmetries.[95] Hexagonal structure has a lower symmetry than cubic phase. Low symmetry corresponds to a crystal-field containing more uneven components around the dopant ions than high symmetry counterparts. The uneven components enhance the electronic coupling between 4f energy levels and higher electronic configuration and subsequently increase f–f transition probabilities of the dopant ions.

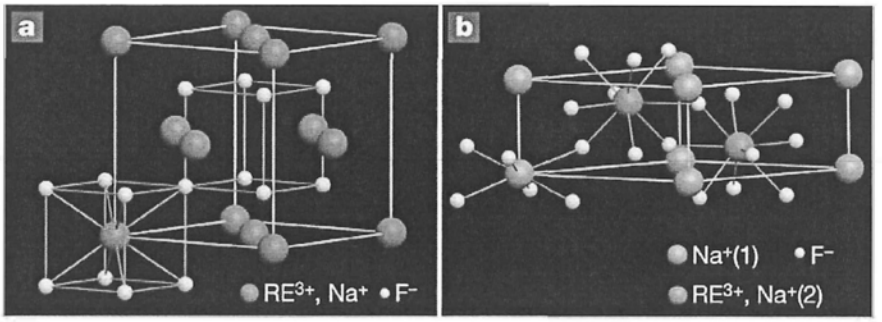

Figure 1.10 a, b, Schematic presentation of cubic- and hexagonal-phase $NaREF_4$ nanostructures, respectively. In the cubic phase, equal numbers of F^- cubes contain cations and vacancies. In the hexagonal phase, an ordered array of F^- ions offers two types of cation sites: one occupied by Na^+ and the other occupied by RE^{3+} and Na^+.[95]

Various approaches have been developed to prepare $NaYF_4$-based upconversion materials, including coprecipitation,[90] hydrothermal and solvothermal,[96-98] thermal-decomposition methods.[99-102] The effect of morphology on the upconversion efficiency has been investigated by using rare earth-doped $NaYF_4$ nanospheres,[88, 103] nanoplates,[101] nanorods,[104, 105] nanodisks.[106] Surface modification has been used not only to improve the efficiency and photostability, but also to provide more opportunities to attach biological molecules for biological applications.[107-109]

The unique NIR to visible optical property have been widely used in a variety of applications, including solid-state lasers,[110] NIR quantum counting devices,[83] biotechnology[111, 112] etc. Recently the fluorescence resonance energy transfer

(FRET) from upconversion materials to downconversion fluorescent materials and metal nanoparticles has attracted great research interests.[113-115] For example, Zhang et al synthesized mesoporous-silica-coated $NaYF_4$ nanoparticles.[116] Photosensitizers were incorporated into the porous silica shell. The resulting materials were used photodynamic therapy. Upon NIR irradiation, the nanocrystals convert NIR to visible light, which further triggers the photosensitizer to release reactive singlet oxygen to kill cancer cells. Wang and coworkers have incorporated $NaYF_4$:Yb, Er into dye sensitized solar cell.[117] The dyes can efficiently absorb the up-converting luminescence emitted by $NaYF_4$:Yb, Er under NIR irradiation.

Near infrared (NIR) photocatalysis involving YF_3: Yb,Tm/TiO_2 core/shell nanoparticles has been reported recently.[118] The upconversion YF_3: Yb,Tm particles absorb NIR light and emit a very weak UV light which excites TiO_2 for photocatalysis. NIR to UV conversion is obviously a difficult process, and it would be much easier to convert NIR to visible-light.

1.5 Summary

This chapter gives a brief introduction on the mechanism of semiconductor-mediated photocatalysis. Furthermore the strategies to improve the photocatalytic activity of UV light photocatalysts are presented. Then the approaches to fabricate visible light photocatalysts are discussed. Finally the

fundaments of upconversion materials are described, including mechanism, requirements of construct upconversion materials, and applications.

1.6 Aim of This Research and its Significance

According to the energy distribution (Figure 1.2), over 80% of solar energy is in the visible and near infrared light spectral region. To harvest this part of solar spectrum, it is very important to develop broad spectral photocatalysts. In this thesis, firstly we are focusing on improving the photocatalytic efficiency of visible light photocatalysts. Then the photoresponse of photocatalysis is further extended into NIR region.

The improvement of visible light photocatalytic efficiency is realized by two approaches: fabricating a composite semiconductor by combining a novel low bandgap semiconductor CZTS with mesoporous TiO_2; incorporating CdS and gold nanoparticles into TNAs.

NIR-driven photocatalysis is prepared based on the upconversion materials. A facile self-assembly method is developed to prepare porous $NaYF_4$:Yb,Er upconversion nanocrystals. Then NIR-driven photocatalysts are synthesized by coupling $NaYF_4$:Yb,Tm with conventional visible photocatalyst CdS. The NIR-driven photocatalytic activity is studied.

It is believed that the broad spectral photocatalysts are of interests in the field of photochemistry, catalysis, as well as environment science. It will open up new

possibilities for the development of efficient solar-induced photocatalysts.

1.7 References

[1] Rajeshwar, K.; Osugi, M. E.; Chanmanee, W.; Chenthamarakshan, C. R.; Zanoni, M. V. B.; Kajitvichyanukul, P.; Krishnan-Ayer, R. *J. Photochem. Photobiol., C*, **2008**, *9*, 171.

[2] Nowotny, J. *Energy Environ. Sci.*, **2008**, *1*, 565.

[3] Hoffmann, M. R.; Martin, S. T.; Choi, W. Y.; Bahnemann, D. W. *Chem. Rev.*, **1995**, *95*, 69.

[4] Ahmed, S.; Rasul, M. G.; Martens, W. N.; Brown, R.; Hashib, M. A. *Desalination*, **2010**, *261*, 3.

[5] Chen, X.; Mao, S. S. *Chem. Rev.*, **2007**, *107*, 2891.

[6] Hu, X. L.; Li, G. S.; Yu, J. C. *Langmuir*, **2010**, *26*, 3031.

[7] Zhang, D. Q.; Li, G. S.; Yu, J. C. *J. Mater. Chem.*, **2010**, *20*, 4529.

[8] Li, C. H.; Wang, F.; Yu, J. C. *Energy Environ. Sci.*, **2011**, *4*, 100.

[9] Fujishima, A.; Honda, K. *Nature*, **1972**, *238*, 37.

[10] Wu, L.; Yu, J. C.; Wang, X. C.; Zhang, L. Z.; Yu, J. G. *J. Solid State Chem.*, **2005**, *178*, 321.

[11] Yu, J. C.; Zhang, L. Z.; Yu, J. G. *Chem. Mater.*, **2002**, *14*, 4647.

[12] Yu, J. C.; Ho, W. K.; Lin, J.; Yip, K. Y.; Wong, P. K. *Environ. Sci. Technol.*,

2003, *37*, 2296.

[13] Hu, C.; Yu, J. C.; Hao, Z. P.; Wong, P. K. *Appl. Catal., B*, **2003**, *42*, 47.

[14] Wu, L.; Yu, J. C.; Zhang, L. Z.; Wang, X. C.; Ho, W. K. *J. Solid State Chem.*, **2004**, *177*, 2584.

[15] Libanori, R.; Giraldi, T. R.; Longo, E.; Leite, E. R.; Ribeiro, C. *J. Sol-Gel Sci. Technol.*, **2009**, *49*, 95.

[16] Dozzi, M. V.; Chiarello, G. L.; Selli, E. *J. Adv. Oxid. Technol.*, **2010**, *13*, 305.

[17] Sharma, R.; Das, P. P.; Misra, M.; Mahajan, V.; Bock, J. P.; Trigwell, S.; Biris, A. S.; Mazumder, M. K. *Nanotechnology*, **2009**, *20*.

[18] Arconada, N.; Castro, Y.; Duran, A. *Appl. Catal., A*, **2010**, *385*, 101.

[19] Xu, X. J.; Fang, X. S.; Zhai, T. Y.; Zeng, H. B.; Liu, B. D.; Hu, X. Y.; Bando, Y.; Golberg, D. *Small*, **2011**, *7*, 445.

[20] Yu, J. G.; Dai, G. P.; Cheng, B. *J. Phys. Chem. C*, **2010**, *114*, 19378.

[21] Dessombz, A.; Pasquier, C. R.; Davidson, P.; Chaneac, C. *J. Phys. Chem. C*, **2010**, *114*, 19799.

[22] Zhang, H. M.; Liu, P. R.; Liu, X. L.; Zhang, S. Q.; Yao, X. D.; An, T. C.; Amal, R.; Zhao, H. J. *Langmuir*, **2010**, *26*, 11226.

[23] Toma, S. H.; Bonacin, J. A.; Araki, K.; Toma, H. E. *Surf. Sci.*, **2006**, *600*, 4591.

[24] Rajh, T.; Ostafin, A. E.; Micic, O. I.; Tiede, D. M.; Thurnauer, M. C. *J. Phys. Chem.*, **1996**, *100*, 4538.

[25] Pan, J. H.; Dou, H. Q.; Xiong, Z. G.; Xu, C.; Ma, J. Z.; Zhao, X. S. *J. Mater. Chem.*, **2010**, *20*, 4512.

[26] Braun, P. V.; Osenar, P.; Tohver, V.; Kennedy, S. B.; Stupp, S. I. *J. Am. Chem. Soc.*, **1999**, *121*, 7302.

[27] Roy, P.; Kim, D.; Lee, K.; Spiecker, E.; Schmuki, P. *Nanoscale*, **2010**, *2*, 45.

[28] Mor, G. K.; Varghese, O. K.; Paulose, M.; Shankar, K.; Grimes, C. A. *Sol. Energy Mater. Sol. Cells*, **2006**, *90*, 2011.

[29] Zwilling, V.; Darque-Ceretti, E.; Boutry-Forveille, A.; David, D.; Perrin, M. Y.; Aucouturier, M. *Surf. Interface Anal.*, **1999**, *27*, 629.

[30] Paulose, M.; Shankar, K.; Yoriya, S.; Prakasam, H. E.; Varghese, O. K.; Mor, G. K.; Latempa, T. A.; Fitzgerald, A.; Grimes, C. A. *J. Phys. Chem. B*, **2006**, *110*, 16179.

[31] Prakasam, H. E.; Shankar, K.; Paulose, M.; Varghese, O. K.; Grimes, C. A. *J. Phys. Chem. C*, **2007**, *111*, 7235.

[32] Shankar, K.; Mor, G. K.; Fitzgerald, A.; Grimes, C. A. *J. Phys. Chem. C*, **2007**, *111*, 21.

[33] Shankar, K.; Mor, G. K.; Prakasam, H. E.; Yoriya, S.; Paulose, M.; Varghese, O. K.; Grimes, C. A. *Nanotechnology*, **2007**, *18*.

[34] Yoriya, S.; Prakasam, H. E.; Varghese, O. K.; Shankar, K.; Paulose, M.; Mor, G. K.; Latempa, T. J.; Grimes, C. A. *Sens. Lett.*, **2006**, *4*, 334.

[35] Macak, J. M.; Zlamal, M.; Krysa, J.; Schmuki, P. *Small*, **2007**, *3*, 300.

[36] Wang, D. A.; Liu, Y.; Yu, B.; Zhou, F.; Liu, W. M. *Chem. Mater.*, **2009**, *21*, 1198.

[37] Ho, W.; Yu, J. C.; Lee, S. *Chem. Commun.*, **2006**, 1115.

[38] Wang, X. C.; Yu, J. C.; Chen, Y. L.; Wu, L.; Fu, X. Z. *Environ. Sci. Technol.*, **2006**, *40*, 2369.

[39] Yu, J. C.; Ho, W. K.; Yu, J. G.; Yip, H.; Wong, P. K.; Zhao, J. C. *Environ. Sci. Technol.*, **2005**, *39*, 1175.

[40] Yu, J. C.; Li, G. S.; Wang, X. C.; Hu, X. L.; Leung, C. W.; Zhang, Z. D. *Chem. Commun.*, **2006**, 2717.

[41] Huang, Y. Y.; Sun, F. Q.; Wang, H. J.; He, Y.; Li, L. S.; Huang, Z. X.; Wu, Q. S.; Yu, J. C. *J. Mater. Chem.*, **2009**, *19*, 6901.

[42] Li, G. S.; Zhang, D. Q.; Yu, J. C. *Chem. Mater.*, **2008**, *20*, 3983.

[43] Li, G. S.; Zhang, D. Q.; Yu, J. C.; Leung, M. K. H. *Environ. Sci. Technol.*, **2010**, *44*, 4276.

[44] Wang, H. J.; Sun, F. Q.; Zhang, Y.; Li, L. S.; Chen, H. Y.; Wu, Q. S.; Yu, J. C. *J. Mater. Chem.*, **2010**, *20*, 5641.

[45] Ho, W. K.; Yu, J. C. *J. Mol. Catal. A: Chem.*, **2006**, *247*, 268.

[46] Li, G. S.; Zhang, D. Q.; Yu, J. C. *Environ. Sci. Technol.*, **2009**, *43*, 7079.

[47] Li, G. S.; Zhang, D. Q.; Yu, J. C. *Phys. Chem. Chem. Phys.*, **2009**, *11*, 3775.

[48] Zhang, L. S.; Wong, K. H.; Chen, Z. G.; Yu, J. C.; Zhao, J. C.; Hu, C.; Chan, C. Y.; Wong, P. K. *Appl. Catal., A*, **2009**, *363*, 221.

[49] Umebayashi, T.; Yamaki, T.; Itoh, H.; Asai, K. *J. Phys. Chem. Solids*, **2002**, *63*, 1909.

[50] Park, Y.; Kim, W.; Park, H.; Tachikawa, T.; Majima, T.; Choi, W. *Appl. Catal., B*, **2009**, *91*, 355.

[51] Higashimoto, S.; Azuma, M. *Appl. Catal., B*, **2009**, *89*, 557.

[52] Asahi, R.; Morikawa, T. *Chem. Phys.*, **2007**, *339*, 57.

[53] Chang, X. F.; Huang, J.; Cheng, C.; Sha, W.; Li, X.; Ji, G. B.; Deng, S. B.; Yu, G. *J. Hazard. Mater.*, **2010**, *173*, 765.

[54] Long, M.; Cai, W. M.; Cai, J.; Zhou, B. X.; Chai, X. Y.; Wu, Y. H. *J. Phys. Chem. B*, **2006**, *110*, 20211.

[55] Shi, R.; Huang, G. L.; Lin, J.; Zhu, Y. F. *J. Phys. Chem. C*, **2009**, *113*, 19633.

[56] Wang, X. C.; Maeda, K.; Thomas, A.; Takanabe, K.; Xin, G.; Carlsson, J. M.; Domen, K.; Antonietti, M. *Nat. Mater.*, **2009**, *8*, 76.

[57] Xiao, G. C.; Wang, X. C.; Li, D. Z.; Fu, X. Z. *J. Photochem. Photobiol., A*, **2008**, *193*, 213.

[58] Merkoci, A.; Marin, S.; Castaneda, M. T.; Pumera, M.; Ros, J.; Alegret, S. *Nanotechnology*, **2006**, *17*, 2553.

[59] Zheng, J.; Song, X. B.; Chen, N.; Li, X. G. *Cryst. Growth Des.*, **2008**, *8*, 1760.

[60] Li, Y. X.; Hu, Y. F.; Peng, S. Q.; Lu, G. X.; Li, S. B. *J. Phys. Chem. C*, **2009**, *113*, 9352.

[61] Marandi, M.; Taghavinia, N.; Zad, A. I.; Mahdavi, S. M. *Nanotechnology*, **2006**, *17*, 1230.

[62] Kim, Y. K.; Park, H. *Energy Environ. Sci.*, **2010**, *4*, 685.

[63] Yu, J. C.; Wu, L.; Lin, J.; Li, P. S.; Li, Q. *Chem. Commun.*, **2003**, 1552.

[64] Zhang, H.; Zhu, Y. F. *J. Phys. Chem. C*, **2010**, *114*, 5822.

[65] Pawar, S. M.; Pawar, B. S.; Moholkar, A. V.; Choi, D. S.; Yun, J. H.; Moon, J. H.; Kolekar, S. S.; Kim, J. H. *Electrochim. Acta*, **2010**, *55*, 4057.

[66] Guo, Q.; Ford, G. M.; Yang, W. C.; Walker, B. C.; Stach, E. A.; Hillhouse, H. W.; Agrawal, R. *J. Am. Chem. Soc.*, **2010**, *132*, 17384.

[67] Wu, L.; Yu, J. C.; Fu, X. Z. *J. Mol. Catal. A: Chem.*, **2006**, *244*, 25.

[68] Jia, H. M.; Xu, H.; Hu, Y.; Tang, Y. W.; Zhang, L. Z. *Electrochem. Commun.*, **2007**, *9*, 354.

[69] Xie, Y.; Ali, G.; Yoo, S. H.; Cho, S. O. *ACS Appl. Mater. Interfaces*, **2010**, *2*, 2910.

[70] Wang, C. L.; Sun, L.; Yun, H.; Li, J.; Lai, Y. K.; Lin, C. J. *Nanotechnology*, **2009**, *20*.

[71] Ho, W. K.; Yu, J. C.; Lin, J.; Yu, J. G.; Li, P. S. *Langmuir*, **2004**, *20*, 5865.

[72] Vasseur, K.; Rand, B. P.; Cheyns, D.; Froyen, L.; Heremans, P. *Chem. Mater.*, **2010**, *23*, 886.

[73] Yamaguchi, T.; Miyabe, T.; Ono, T.; Arakawa, H. *Chem. Commun.*, **2010**, *46*, 5802.

[74] Wang, X. Z.; Wang, Q. W.; Yan, L.; Wong, W. Y.; Cheung, K. Y.; Ng, A. N.; Djurisic, A. B.; Chan, W. K. *Macromol. Rapid Commun.*, **2010**, *31*, 861.

[75] Burckstummer, H.; Kronenberg, N. M.; Meerholz, K.; Wurthner, F. *Org. Lett.*, **2010**, *12*, 3666.

[76] Auzel, F. *Chem. Rev.*, **2004**, *104*, 139.

[77] Wang, F.; Liu, X. G. *Chem. Soc. Rev.*, **2009**, *38*, 976.

[78] Dalton, L. R.; Harper, A. W.; Ghosn, R.; Steier, W. H.; Ziari, M.; Fetterman, H.; Shi, Y.; Mustacich, R. V.; Jen, A. K. Y.; Shea, K. J. *Chem. Mater.*, **1995**, *7*, 1060.

[79] Kautek, W.; Sorg, N.; Kruger, J. *OPTICAL 2ND-HARMONIC GENERATION (SHG) ON SEMICONDUCTOR ELECTRODES BY MEANS OF FEMTOSECOND AND NANOSECOND-PULSE LASERS*, 1995 pp. 285.

[80] Das, G. P.; Yeates, A. T.; Dudis, D. S. *Chem. Phys. Lett.*, **2004**, *393*, 76.

[81] Prior, Y.; Vogt, H. *J. Opt. Soc. Am.*, **1978**, *68*, 1423.

[82] Suyver, J. F.; Aebischer, A.; Biner, D.; Gerner, P.; Grimm, J.; Heer, S.; Kramer, K. W.; Reinhard, C.; Gudel, H. U. *Opt. Mater.*, **2005**, *27*, 1111.

[83] Chivian, J. S.; Case, W. E.; Eden, D. D. *Appl. Phys. Lett.*, **1979**, *35*, 124.

[84] Hewes, R. A.; Sarver, J. F. *Physical Review*, **1969**, *182*, 427.

[85] Braud, A.; Girard, S.; Doualan, J. L.; Thuau, M.; Moncorge, R.; Tkachuk, A. M. *Phys. Rev. B: Condens. Matter*, **2000**, *61*, 5280.

[86] Bril, A.; Sommerdijk, J. L.; Jager, A. W. D. *J. Electrochem. Soc.*, **1975**, *122*,

660.

[87] Kramer, K. W.; Biner, D.; Frei, G.; Gudel, H. U.; Hehlen, M. P.; Luthi, S. R. *Chem. Mater.*, **2004**, *16*, 1244.

[88] Li, Z. Q.; Zhang, Y. *Nanotechnology*, **2008**, *19*.

[89] Yi, G. S.; Chow, G. M. *Adv. Funct. Mater.*, **2006**, *16*, 2324.

[90] Heer, S.; Kompe, K.; Gudel, H. U.; Haase, M. *Adv. Mater.*, **2004**, *16*, 2102.

[91] Qian, H. S.; Zhang, Y. *Langmuir*, **2008**, *24*, 12123.

[92] Wei, Y.; Lu, F. Q.; Zhang, X. R.; Chen, D. P. *Chem. Mater.*, **2006**, *18*, 5733.

[93] Zeng, J. H.; Su, J.; Li, Z. H.; Yan, R. X.; Li, Y. D. *Adv. Mater.*, **2005**, *17*, 2119.

[94] Zhuang, J. L.; Wang, J.; Yang, X. F.; Williams, I. D.; Zhang, W.; Zhang, Q. Y.; Feng, Z. M.; Yang, Z. M.; Liang, C. L.; Wu, M. M.; Su, Q. *Chem. Mater.*, **2009**, *21*, 160.

[95] Wang, F.; Han, Y.; Lim, C. S.; Lu, Y. H.; Wang, J.; Xu, J.; Chen, H. Y.; Zhang, C.; Hong, M. H.; Liu, X. G. *Nature*, **2010**, *463*, 1061.

[96] Li, C. X.; Yang, J.; Quan, Z. W.; Yang, P. P.; Kong, D. Y.; Lin, J. *Chem. Mater.*, **2007**, *19*, 4933.

[97] Li, C. X.; Quan, Z. W.; Yang, J.; Yang, P. P.; Lin, J. *Inorg. Chem.*, **2007**, *46*, 6329.

[98] Chen, Z. G.; Tian, Q. W.; Song, Y. L.; Yang, J. M.; Hu, J. Q. *J. Alloys Compd.*, **2010**, *506*, L17.

[99] Mai, H. X.; Zhang, Y. W.; Sun, L. D.; Yan, C. H. *J. Phys. Chem. C*, **2007**, *111*, 13721.

[100] Boyer, J. C.; Vetrone, F.; Cuccia, L. A.; Capobianco, J. A. *J. Am. Chem. Soc.*, **2006**, *128*, 7444.

[101] Mai, H. X.; Zhang, Y. W.; Si, R.; Yan, Z. G.; Sun, L. D.; You, L. P.; Yan, C. H. *J. Am. Chem. Soc.*, **2006**, *128*, 6426.

[102] Boyer, J. C.; Cuccia, L. A.; Capobianco, J. A. *Nano Lett.*, **2007**, *7*, 847.

[103] Shan, J. N.; Ju, Y. G. *Nanotechnology*, **2009**, *20*.

[104] Yu, X. F.; Li, M.; Xie, M. Y.; Chen, L. D.; Li, Y.; Wang, Q. Q. *Nano Research*, **2010**, *3*, 51.

[105] Yang, L. W.; Han, H. L.; Zhang, Y. Y.; Zhong, J. X. *J. Phys. Chem. C*, **2009**, *113*, 18995.

[106] Zhang, F.; Wan, Y.; Yu, T.; Zhang, F. Q.; Shi, Y. F.; Xie, S. H.; Li, Y. G.; Xu, L.; Tu, B.; Zhao, D. Y. *Angew. Chem. Int. Ed.*, **2007**, *46*, 7976.

[107] Li, Z. Q.; Zhang, Y. *Angew. Chem. Int. Ed.*, **2006**, *45*, 7732.

[108] Sivakumar, S.; Diamente, P. R.; van Veggel, F. C. *Chem. Eur. J.*, **2006**, *12*, 5878.

[109] Schafer, H.; Ptacek, P.; Zerzouf, O.; Haase, M. *Adv. Funct. Mater.*, **2008**, *18*, 2913.

[110] Rumbles, G. *Nature*, **2001**, *409*, 572.

[111] Xiong, L. Q.; Chen, Z. G.; Yu, M. X.; Li, F. Y.; Liu, C.; Huang, C. H.

Biomaterials, **2009**, *30*, 5592.

[112] van de Rijke, F.; Zijlmans, H.; Li, S.; Vail, T.; Raap, A. K.; Niedbala, R. S.; Tanke, H. J. *Nat. Biotechnol.*, **2001**, *19*, 273.

[113] Li, Z. Q.; Zhang, Y.; Jiang, S. *Adv. Mater.*, **2008**, *20*, 4765.

[114] Wang, L. Y.; Yan, R. X.; Hao, Z. Y.; Wang, L.; Zeng, J. H.; Bao, H.; Wang, X.; Peng, Q.; Li, Y. D. *Angew. Chem. Int. Ed.*, **2005**, *44*, 6054.

[115] Wang, L. Y.; Li, Y. D. *Chem. Commun.*, **2006**, 2557.

[116] Qian, H. S.; Guo, H. C.; Ho, P. C. L.; Mahendran, R.; Zhang, Y. *Small*, **2009**, *5*, 2285.

[117] Chen, Z. G.; Zhang, L. S.; Sun, Y. G.; Hu, J. Q.; Wang, D. Y. *Adv. Funct. Mater.*, **2009**, *19*, 3815.

[118] Qin, W. P.; Zhang, D. S.; Zhao, D.; Wang, L. L.; Zheng, K. Z. *Chem. Commun.*, **2010**, 2304.

Chapter Two

Construction of Au and CdS Loaded TiO_2 Nanotube Arrays with Enhanced Visible Light Photocatalytic Activity

2.1 Introduction

Among the widely used semiconductor photocatalysts, TiO_2 is currently the most promising one because of its unique properties, such as high photocatalytic activity, stability and chemical stability.[1-3] Considerable effort has been made to further improve the photocatalytic activity of TiO_2. Recently the highly ordered, vertically aligned TiO_2 nanotube arrays (TNAs) fabricated by Ti anodization have generated significant research interests.[4-7] The highly ordered structure offers large specific surface areas to efficiently capture solar energy. And the precisely oriented nature makes them excellent electron percolation pathways for vectorial charge transfer.[8-11] However, as a wide band gap semiconductor (3.2V) TiO_2 can only activated by UV light. To shift the photoresponse of TNAs to visible light, various approaches have been developed, for example, nonmetal (C-,[12] N-,[13] B-[14]) and metal (Ag-,[15] Fe-,[16] Zr-[17]) doped TANs show enhanced visible light

photocatalytic activity. Another method is to construct semiconductor composite, such as TNAs/CdS,[18] TNAs/CdSe.[19]

Although CdS is of low band gap (2.6eV) and large absorption cross section, the serious photoerosion limit its use as an efficient visible light photocatalyst. However many researches have indicated that the photostability of CdS is highly improved after combining with TiO_2. And the photocatalytic activity is also enhanced because of efficient electron transfer.[20, 21] Thus CdS-sensitized TNAs with efficient visible light photocatalytic activity have been widely investigated. Gao et al have reported a close space sublimation technique to prepare TNAs/CdS composite.[22] Peng et al fabricated a coaxial heterogeneous structure of TNAs with CdS as a super-thin coating by modified electrochemical atomic layer deposition.[18] Wang et al used developed a single-step sonoelectrodeposition method to prepare TNAs/CdS.[23]

Due to the unique optical properties, plasmon resonant nanostructures have generated considerable interests in many fields, including near-field optics,[24] surface enhanced spectroscopy[25] and medicine.[26] Au,[27] Ag,[28] Pt[29] particles have been widely loaded into TiO_2 to act as electrons trap to enhance photocatalytic activity. In recent years, plasmonic nanoparticles closely coupled to absorbing semiconductors have been utilized to enhance absorption in ultrathin film solar cells.[30, 31]

In this study we develop an effective method to prepare TNAs/CdS/Au

composite with the assistance of sonication. CdS sever as visible light photon acceptor. Through the surface plasma effect gold nanoparticle enhance the absorption ability of CdS. Thus the photocatalytic activity was enhanced compared with TNAs/CdS.

2.2 Experimental Section

2.2.1 Synthesis of TiO_2 nanotube arrays

Highly ordered TiO_2 nanotube arrays were fabricated by an anodic oxidation approach in a two-electrode electrochemical cell. Ethylene glycol (96.5 wt %) solution with additions of 0.5 wt % of NH_4F and 2.0 wt % of deionized (DI) water was used as electrolyte. Ti foil (2cm x 2.5cm) was used as a working electrode, and a platinum (1cm x 3cm) foil served as a counter electrode. Prior to the anodization, Ti foils were washed with ethanol, acetone by ultrasonication to remove the contamination, subsequently rinsed with DI water and then dried in a N_2 stream. Anodization is carried out by immersing Ti foils in as-prepared electrolyte at room temperature. The effect of anodization time periods and voltage on the morphology and size of the prepared nanotube array were investigated. After anodization the samples were removed from the electrode cell, washed with DI water, and then sonicated in ethanol for 2 min to remove the surface debris.

2.2.2 Synthesis of CdS-Sensitized TNAs

TNAs were firstly modified by mercaptoacetic acid (MAA). TNAs were immersed MAA aqueous solution for 2h, then washed by DI-water several time. The modified TNAs were sequentially dipped in four different beakers for 1 min in each beaker during sonication. The first beaker contained 0.025 M cadmium chloride ($CdCl_2$), the next contained 0.025M sodium sulfide (Na_2S) solution. And the other two contained DI water for rinsing the samples. Such preparation procedure was repeated a number of times. In this study, 1, 2, 3 and 4 cycles of CdS deposition were performed (denoted as TNAs/1-CdS, TNAs/2-CdS, TNAs/3-CdS, TNAs/4-CdS, respectively).

2.2.3 Synthesis of TNAs/CdS/Au

TNAs/3-CdS films were immersed into 1, 2-ethanedithiol ethanol solution for 2h, then washed by ethanol and DI water several times. The prepared films were sequentially dipped in four different beakers for 1 min in each beaker during sonication. The first beaker contained 0.001 M gold chloride hydrate ($HAuCl_4.3H_2O$), the next contained 0.001M Sodium borohydride ($NaBH_4$) solution. And the other two contained DI water for rinsing the samples. Such preparation procedure was repeated twice (denoted as TNAs/3-CdS/2-Au). Then

the prepared films were washed by DI-water and dried. A subsequent heating at 400 °C for 1 h with a temperature increasing rate of 1 °C min^{-1} in air was applied to improve crystallization.

2.2.4 Materials Characterization

The general morphology of the products was characterized by a field-emission scanning electron microscope (FESEM, FEI, Quanta 400 FEG) equipped with an energy-dispersive spectroscopy instrument. TEM images and EDX profiles were taken on a Philips CM-120 electron microscopy instrument coupled with an energy-dispersive X-ray (EDX) spectrometer. X-ray diffraction (XRD) patterns were recorded using a Bruker D8 Advance diffractometer with high-intensity Cu $K\alpha_1$ irradiation (λ=1.5406 Å). UV-vis spectra were recorded on a Varian Cary 100 Scan UV-visible system. X-ray photoelectron spectroscopy (XPS, Versa Probe PHI 5000) was employed to determine surface electronic states. The shift of the binding energy due to relative surface charging was corrected using the C_{1S} level at 284.8 eV as an internal standard.

2.2.5 Photocatalytic Degradation of Methylene Blue

Methylene blue (MB) was considered as a model contaminant to test the photocatalytic activity of the samples. Briefly, the prepared TNAs, TNAs/CdS and TNAs/CdS/Au were placed on the bottom of the beaker containing 20 mL MB aqueous solution (10 ppm). Above the beaker a 300W tungsten halogen lamp

with a 400 nm cutoff filter was used as visible light source. A cooling system was used to lower the temperature of MB solution. After 12 h of adsorption/desorption equilibrium, the photocatalytic degradation of methylene blue was initiated. Photodegradation was monitored by measuring the absorbance of the solution at 664 nm.

2.3 Results and Discussion

Figure 2.1 shows the fabrication process for TNAs/CdS/Au composite. According to the literatures, many OH groups existed on the surface of TiO_2 nanotubes. Based on the strong coupling between OH and COOH groups, the surface of TNAs are functionalized by thioglycolic acid molecules and terminated with many SH groups. In the next step, the strong interaction between the –SH groups and cadmium ions facilitates the formation of CdS nanoparticles inside the nanotubes. The subsequent functionalization with 1, 2-ethanedithiol forms many SH groups on the surface of CdS nanoparticles. Then gold nanoparticles deposited in situ on the surface of CdS nanoparticles.

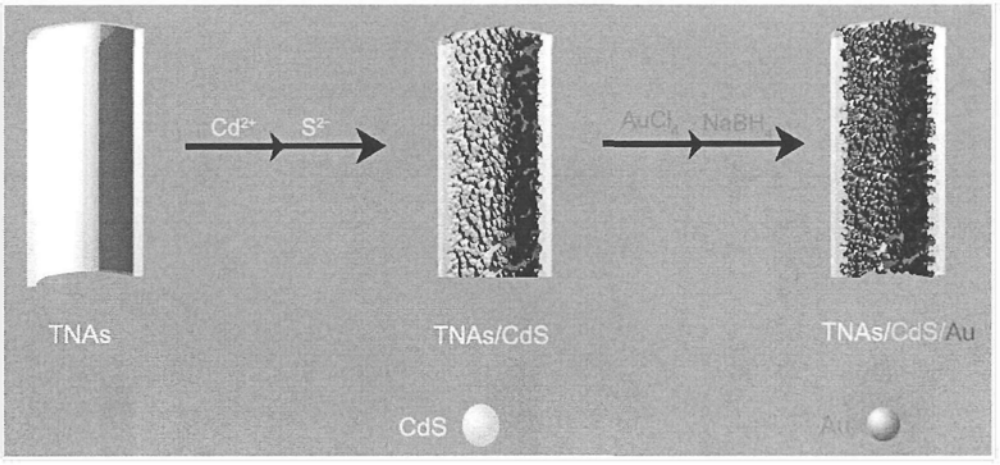

Figure 2.1 Strategy for the preparation of TNAs/CdS/Au composite.

2.3.1 Morphology and Composition study

2.3.1.1 Pure TNAs

The morphologies of the TNAs films were examined using FESEM. Figure 2.2 presents the typical FESEM images with top, bottom and side views of the prepared TNAs film. The TNAs were covered with a large amount of debris (Figure 2.2a), which could be removed by sonication cleaning in ethanol (Figure 2.2b-e). Uniform nanotube arrays with the tubes open on the top and close at the bottom could be clearly observed. The average inner diameter of the nanotube is about 130 nm with a wall thickness of 10-20 nm. From the cross sectional image (Figure 2.2f), it can be clearly seen that the TNAs are highly ordered, compact (nanotubes were well-attached to each other) and vertically oriented (straight). The tube length is about 20μm, corresponding to a high aspect ratio of about 150. The hollow structure could be more clearly seen from TEM images in Figure 2.3.

Both inner and outer surface of the nanotubes are rather smooth. The mechanism for the formation of TNAs in fluoride ion containing electrolytes involves three simultaneously occurring processes:[32] (i) TiO_2 formation at the surface of the metal due to interaction of the metal with O_2 or OH^- ions, (ii) field assisted dissolution of TiO_2 in electrolyte and (iii) chemical dissolution of Ti and TiO_2 due to the etching by fluoride ions.

The evolution of pore size and length of the prepared TNAs were further investigated by adjusting the anodization voltage (Figure 2.4a) and reaction time (Figure 2.4b). From Figure 2.4a it is seen that at low anodization voltages (10 V and 20 V), the electrochemical anodization speed was very low and the products had very small pore sizes and length. With the increase of anodization voltage, the pore size and length greatly increase. It might be due to the high electrochemical anodization speed. Although the pore size and length further increase at 80V, the increment speed from 60 to 80V is lower than that from 40 to 60V, indicating that that the dissolution speed is higher than electrochemical anodization speed. The similar phenomenon was observed in the time-dependent evolution as shown in Figure 2.4b.

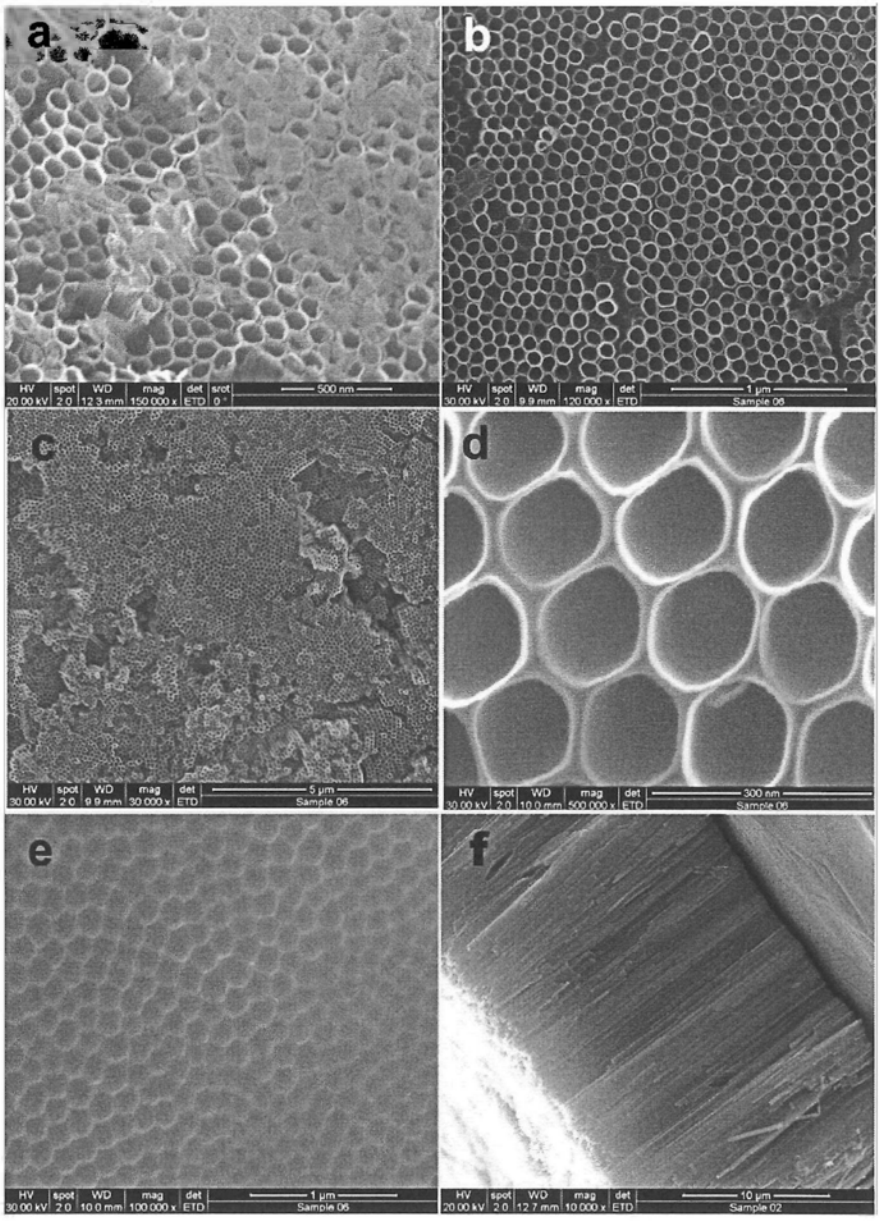
a
HV 20.00 kV | spot 2.0 | WD 12.3 mm | mag 150 000 x | det ETD | srot 0 ° | 500 nm
b
HV 30.00 kV | spot 2.0 | WD 9.9 mm | mag 120 000 x | det ETD | 1 µm | Sample 06
c
HV 30.00 kV | spot 2.0 | WD 9.9 mm | mag 30 000 x | det ETD | 5 µm | Sample 06
d
HV 30.00 kV | spot 2.0 | WD 10.0 mm | mag 500 000 x | det ETD | 300 nm | Sample 06
e
HV 30.00 kV | spot 2.0 | WD 10.0 mm | mag 100 000 x | det ETD | 1 µm | Sample 06
f
HV 20.00 kV | spot 2.0 | WD 12.7 mm | mag 10 000 x | det ETD | 10 µm | Sample 02

Figure 2.2 FESEM images of TNAs grown from a 0 5 wt % NH_4F ethylene glycol electrolyte for 3 h at 60 V. Typical top (a-d), bottom (e) and cross sectional view images were obtained. (a) before ultrasound treatment (b-f) after ultrasound treatment.

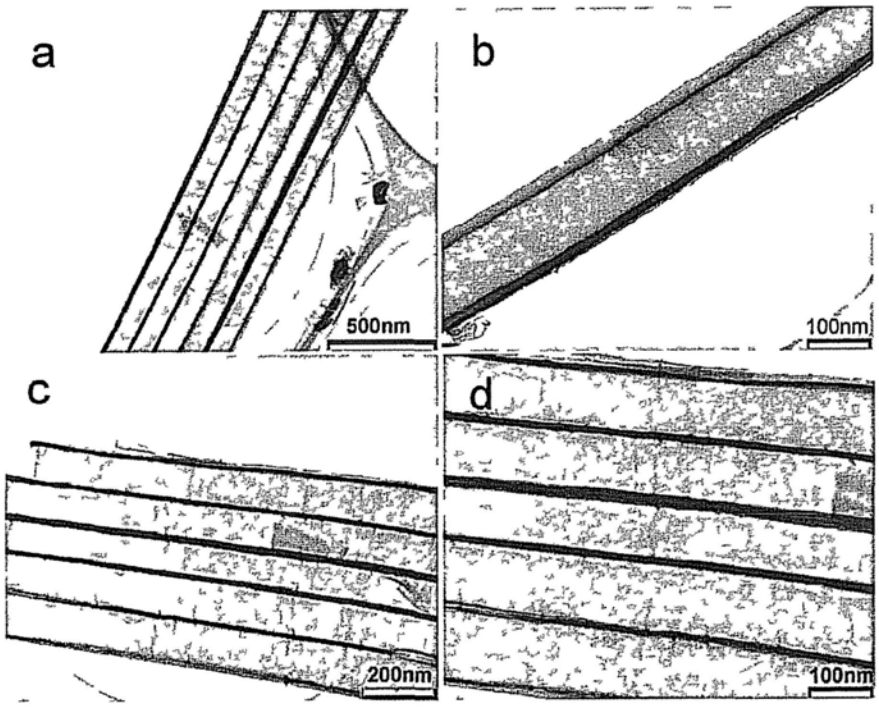

Figure 2.3 TEM images of TNAs grown from a 0 5 wt % NH_4F ethylene glycol electrolyte for 3 h at 60 V.

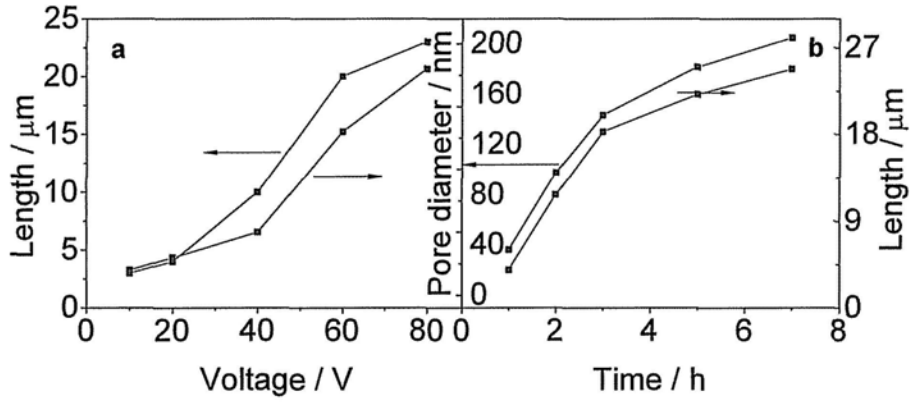

Figure 2.4 Voltage- (a) and time-(b) dependent evolution of pore size and length of TNAs. The anodization time and voltage in figure a and b are 3h and 60V, respectively.

2.3.1.2 TNAs/CdS

In order to facilitate the filling of CdS, TNAs were functionalized by MAA molecules. Thus more Cd^{2+} can be anchored on the surface of TNAs through the interaction between SH groups and Cd^{2+}, favoring the in situ formation of CdS nanoparticles. The morphologies and composition of the as-prepared TNAs/CdS was studied by SEM and EDX, as shown in Figure 2.5. Clearly, CdS deposition process did not destroy the ordered TiO_2 nanotube array structure. For TNAs/1-CdS (Figure 2.5a), some CdS nanoparticles with diameters smaller than 20 nm are observed on inner surface of the regularly arranged tube. The corresponding EDX analysis (inset in Figure 2.5a) confirms the presence of CdS nanoparticles. For TNAs/2-CdS (Figure 2.5b) and TNAs/3-CdS (Figure 2.5c), the amount of CdS nanoparticles greatly increased. A uniform coaxial heterogeneous

structure was formed. When the amount of CdS is further increased to form TNAs/4-CdS (Figure 2.5d), the entrance of the TNAs was blocked by many large CdS nanoparticles. These large particles could block the light to get inside the nanotube. As a result the photocatalytic activity is decreased.

EDX quantitative analysis confirmed that the stoichiometric ratio of Cd to S for every sample approximately equals to 1:1, as expected for the format of CdS compound. The atomic ratio of Cd/Ti increases with the amount of CdS, which agrees well with our experiment conditions (Figure 2.5e).

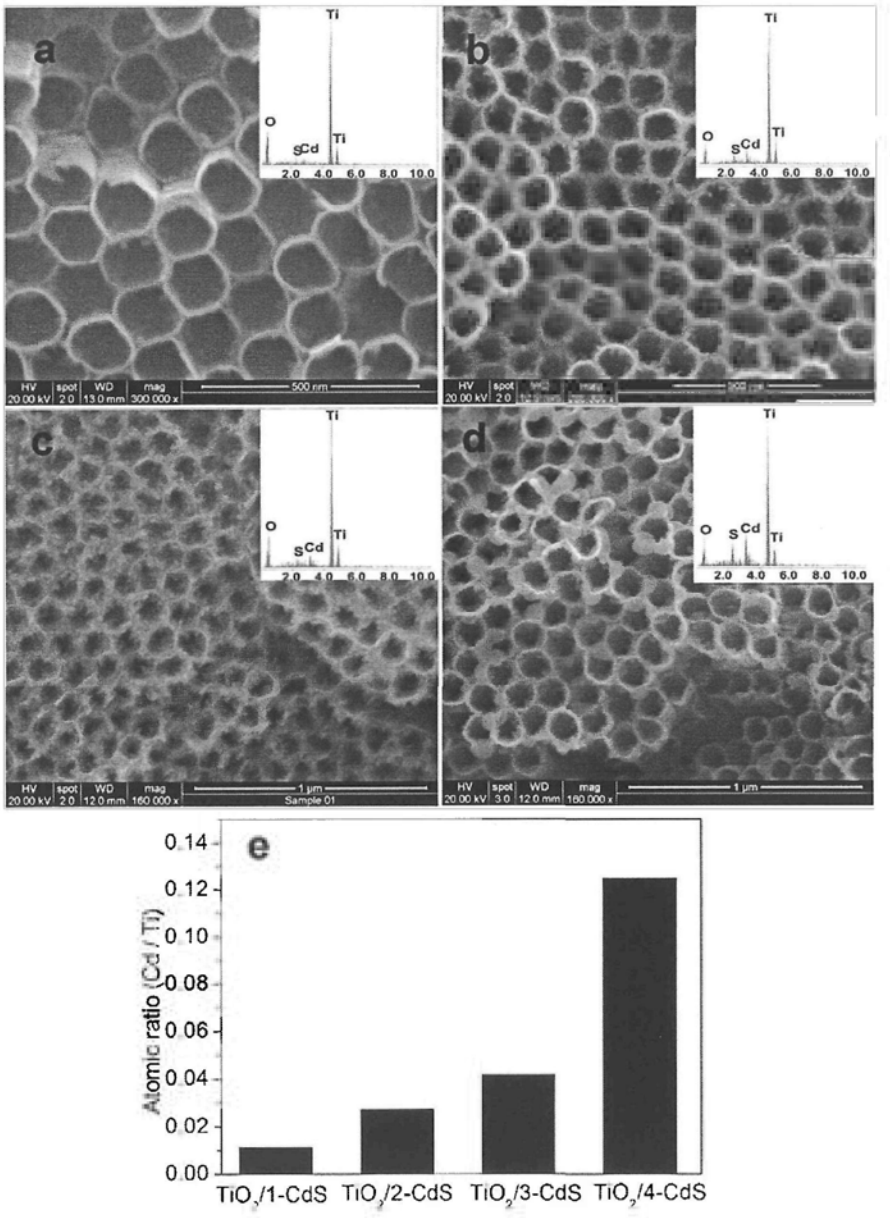

Figure 2.5 FESEM images and EDX analysis of TNAs/CdS composite with different amount of CdS grown

(a) TNAs/1-CdS (b) TNAs/2-CdS (c) TNAs/3-CdS (d) TNAs/4-CdS. The insets are the corresponding EDX analysis. Figure e shows the atomic ratios of Cd/Ti for different samples.

SEM observations confirm the formation of CdS nanoparticles on the inner surface of TiO_2 nanotubes at the opening area. To determine whether the CdS particles were introduced on the outer surface and deep into the TNAs, the TNAs/3-CdS film was further investigated by TEM (Figure 2.6). Compared with Figure 2.3, it is obvious that many CdS nanoparticles are seen inside the whole tube. And the outer surface is rather smooth, indicating that this method can effectively suppresses the deposition of the CdS on the outer surface of the nanotube.

Compared with the reported methods,[33, 34] lower precursor (Cd^{2+}) concentration and less recycling treatment are involved to prepare uniform TNAs/CdS in our method. It might be due to both the assistance of ultrasonication and surface modification.

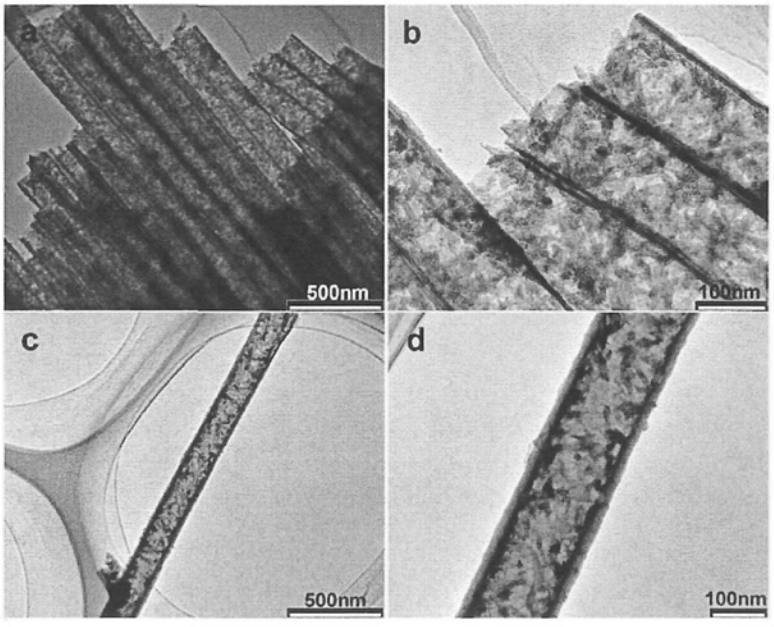

Figure 2.6 TEM images of TNAs/3-CdS

2.3.1.3 TNAs/CdS/Au

To prepare gold nanoparticles around CdS, 1, 2-ethanedithiol ethanol was used to functionalize TNAs/3-CdS. The two SH- groups connect the CdS with gold together. The morphologies and composition of the asprepared TNAs/CdS was studied by SEM, TEM and EDX, as shown in Figure 2.7. SEM and TEM observations (Figure 2.7a-d) are similar to TNAs/CdS. Many nanoparticles could be seen inside the whole tube. The difference between TNAs/3-CdS and TNAs/3-CdS/2-Au could be distinguished from EDX analysis (Figure 2.7e and f). For TNAs/3-CdS/2-Au, EDX analysis shows a strong signal of gold along with Ti, Cd and S. And the atomic ratio of Ti: Cd: S: Au is determined to be 28:1.02:1.18:1.25, indicating the formation of TNAs/CdS/Au composite.

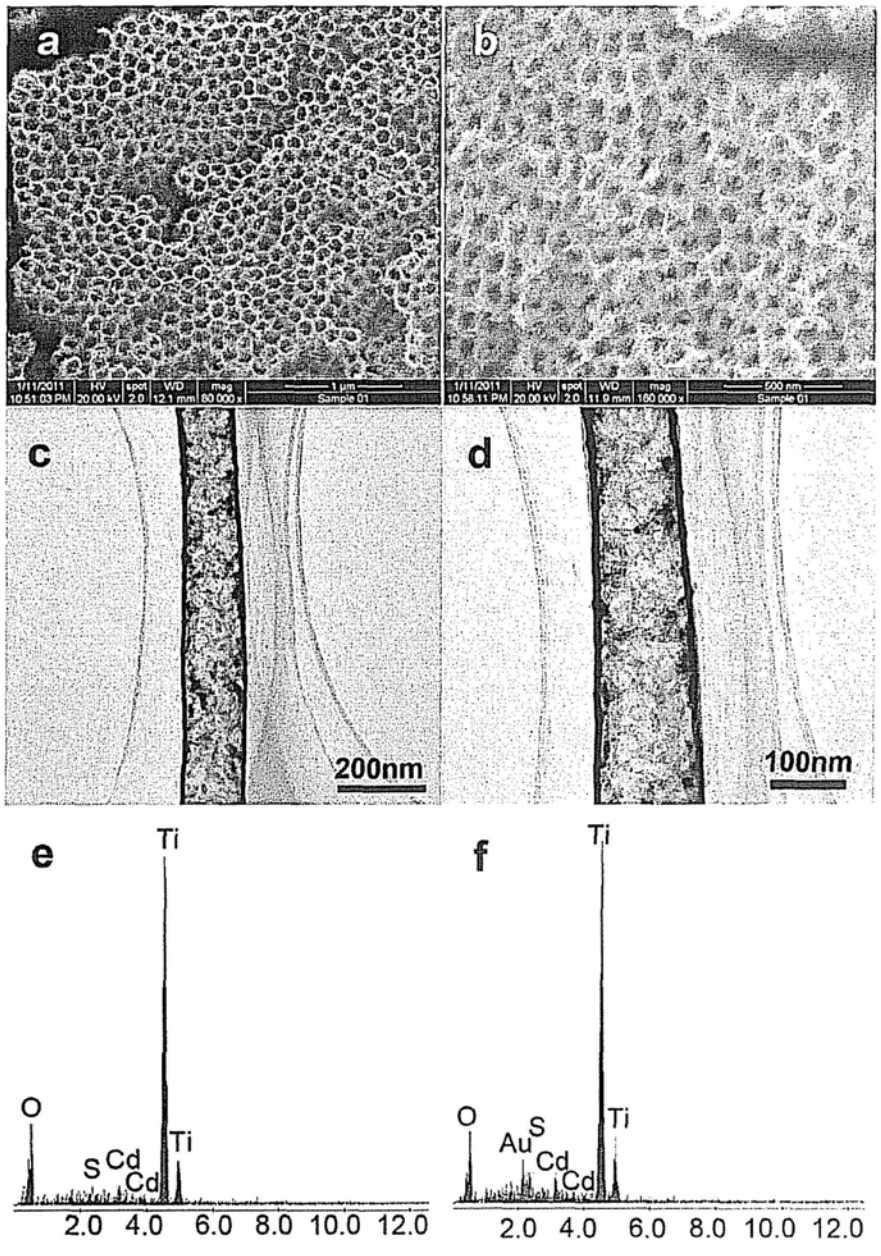

Figure 2.7 SEM, TEM images and EDX analysis of the prepared films

(a- d, f) TNAs/3-CdS/2-Au (e) TNAs/3-CdS

2.3.2 XRD and XPS Measurements

The structures of the products are also investigated by XRD, as shown in Figure 2.8. Figure 2.8a shows the typical XRD pattern for the pure Ti foil, which is consistent with the standard (JCPDF 44-1294). In Figure 2.8b, the diffraction peaks at 2θ of 25.3, 37.0, 37.8, 38.5, 48.1, 53.9, 55.1, 62.7, 68.7, 70.3, 75.0 and 76.1° match very well with anatase-TiO_2 (JCPDF 21-1272). And the strong intensity indicates good crystallinity. Compared with Figure 2.8b, Figure 2.8c shows four new peaks centered at 2θ of 26.5, 28.3, 44.4 and 64.6°. They are attributed to (002), (101) crystal plans of hexagonal CdS phase (JCPDF 41-1049) and (200), (220) plans of cubic phase gold (JCPDF 04-0784), respectively. It should be mentioned that these peaks are rather weak due to the smaller amount compared with TiO_2. The other diffraction peaks of CdS and gold are not clearly observed because of the overlap with anatase TiO_2.

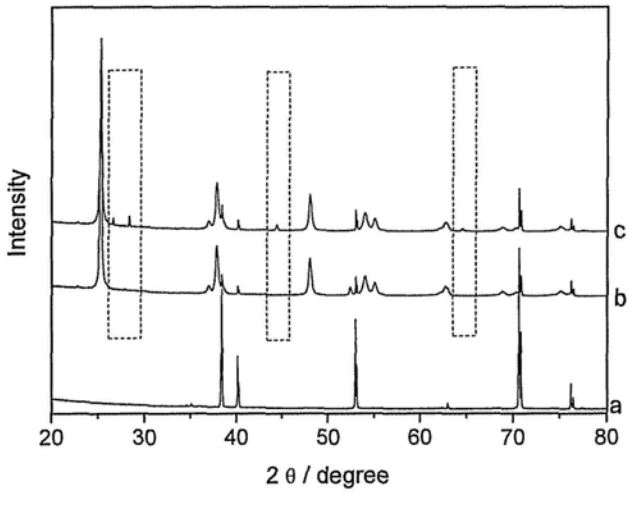

Figure 2.8 XRD patterns for (a) Ti foil, (b)TNAs and (c)TNAs/CdS/Au

XPS was carried out to analyze the chemical composition of the prepared TNAs/3-CdS/2-Au. Figure 2.9 shows high-resolution XPS spectra of the four different elements. The spin–orbit components (2p3/2 and 2p1/2) of the Ti 2p peak were well deconvolved by two curves at approximately 458.8 and 464.7 eV, corresponding to Ti^{4+} in a tetragonal structure (Figure 2.9a). The Cd $3d_{5/2}$and Cd $3d_{3/2}$ peaks are centered at 405.4 and 412.3 eV with a spin-orbit separation of 6.9 eV (Figure 2.9b). It is in good agreement with published values for CdS.[35] The S 2p core level spectrum given in Figure 2.9c indicates two chemically distinct species because of the presence of S 2p3/2 and S 2p1/2. The peak at 161.3 eV is for sulfide. The area ratio is about 2:1, which matches very well with published values for CdS.[35] The peaks observed at 83.6 and 86.9 eV confirmed the formation of metallic gold.

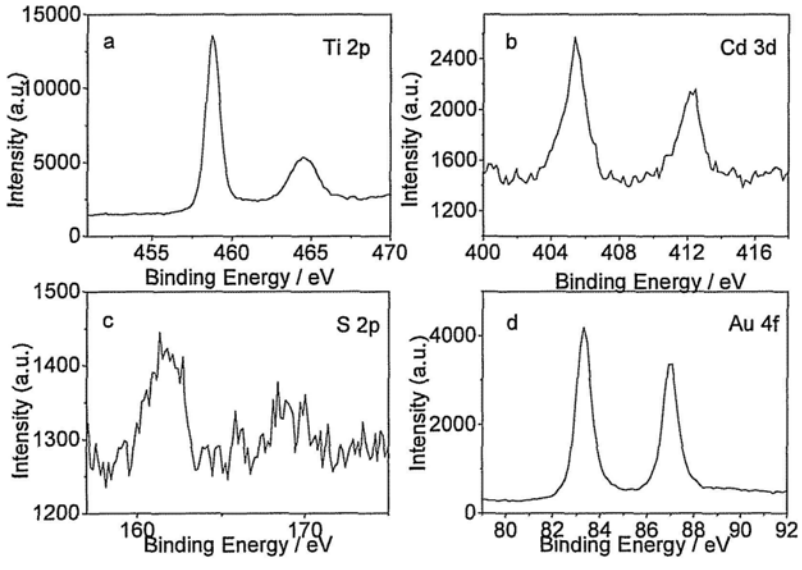

Figure 2.9 High-resolution XPS spectra of (a) Ti 2p, (b) Cd 3d, (c) S 2p and (d) Au 4f for the TNAs/3-CdS/2-Au composite

2.3.3 UV-visible Spectra

UV-visible diffuse reflectance spectroscopy (DRS) was used to characterize the electronic states of the as prepared samples. As shown in Figure 2.10a, pure TNAs show strong absorption in UV region (below 400 nm) due to the intrinsic interband transition absorption. Compared with pure TNAs, TNAS/CdS exhibits a broad absorbance band in visible light region with the absorption onset at 550 nm (Figure 2.10b). This indicates that CdS can be used to assist TNAs to capture visible light. For TNAS/CdS/Au composite, the broad peak centered at 565 nm is corresponding to plasmon resonance absorption of Au nanoparticles (Figure 2.10c). The absorbance is so intense that the CdS absorption is overlapped. And the absorption intensity in both UV and visible region is highly enhanced. Such absorption enhancement might be due to the plasmon-induced local field effect.

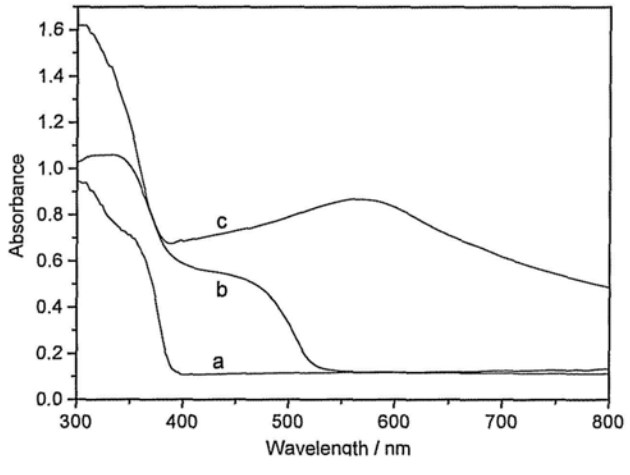

Figure 2.10 UV-visible absorption spectra of (a) TNAs, (b) TNAs/3-CdS and (c) TNAs/3-CdS/2-Au

2.3.4 Photocatalytic Activity

To evaluate and compare the photocatalytic activity of the samples, the degradation of methylene blue was used as a probe photoreaction. Figure 2.11 illustrates the results of the photocatalytic evaluation. It can be clearly seen from Figure 2.11a that TNAs/3-CdS is efficient in the photodegradation of methylene blue under visible light irradiation. The concentration of methylene blue dropped to about 55% after 3h irradiation. Enhanced photocatalytic activity is achieved for TNAs/3-CdS/2-Au as shown in Figure 2.11b. And the final concentration of methylene blue is only about 28% after 3h irradiation. This is because gold nanoparticles can enhance the light absorption ability of CdS, which has been demonstrated by UV-visible absorption spectra. Thus more electrons are promoted into conduction band of CdS under visible light irradiation. Consequently, the number of electrons transferred from CdS to TiO_2 is also increased.

The recyclability of TNAs/3-CdS/2-Au is also investigated. After the photocatalytic reactions the substrate was removed from the solution and dried for the subsequent photoreaction cycle. As shown in Figure 2.12, the TNAs/3-CdS/2-Au composite showed good stability. And the photocatalytic activity maintained very well after three reaction cycles.

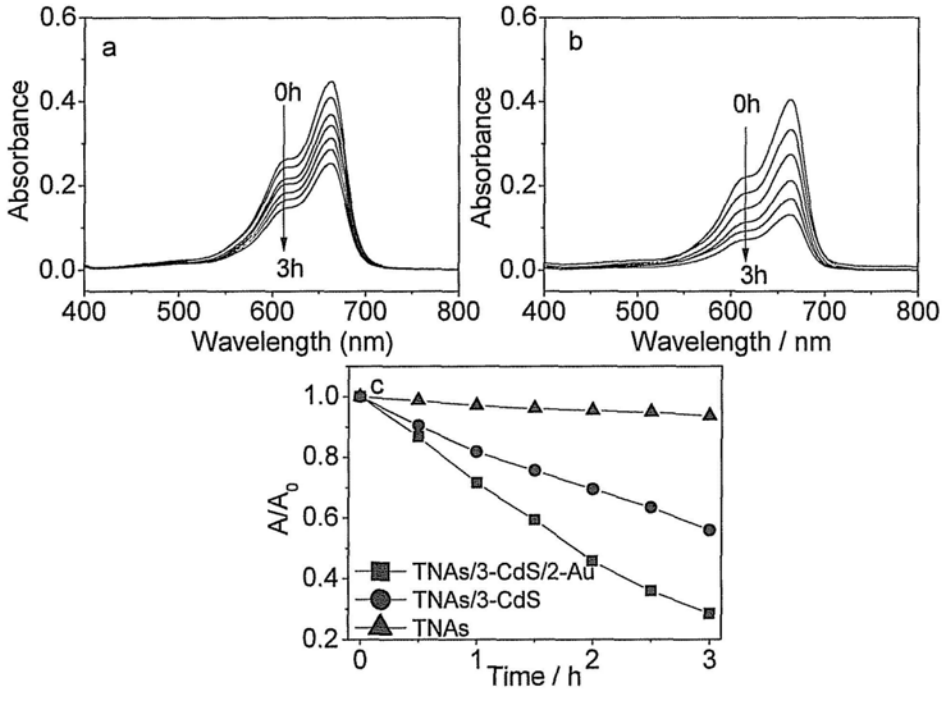

Figure 2.11 Photodegradation of methylene blue for (a) TNAs/3-CdS and (b) TNAs/3-CdS/2-Au under visible light irradiation ($\lambda > 400$ nm). (c) A comparison of the photoactivities for TNAs/3-CdS/2-Au and TNAs/3-CdS. A is the absorbance of methylene blue ($\lambda_{max} = 664$ nm) and A_0 is the initial absorbance.

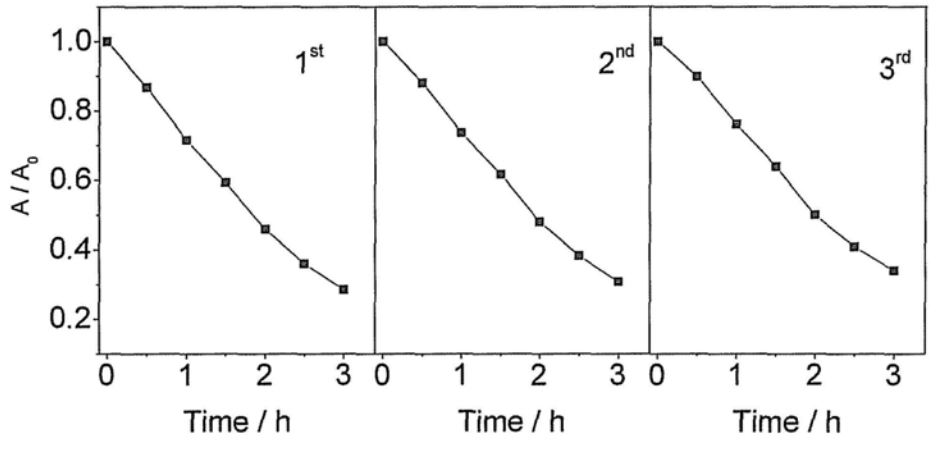

Figure 2.12 The cyclability of photocatalytic activity for TNAs/3-CdS/2-Au

2.3.5 Mechanism

In TNAs/CdS composite, the low band gap semiconductor CdS could capture visible light photons. Then the photogenerated electrons are injected into the conduction bands of TiO_2 to trigger photocatalysis (Figure 2.13a).

In TNAs/CdS/Au composite (Figure 2.13b), the absorbance in the visible light region is much larger than TNAs/CdS as shown in UV-visible absorption spectra (Figure 2.10). This is because gold nanoparticles have a strong surface plasmon absorption peak in visible light region. The surface plasmon excitation can provide large electromagnetic field enhancements on the surfaces of metals.[36-39] Then the localized field amplification can greatly enhance the absorption of the CdS that have been closely coupled to gold nanoparticles. Then more electrons are promoted into the conduction bands of CdS. Thus the photocatalytic activity is enhanced.

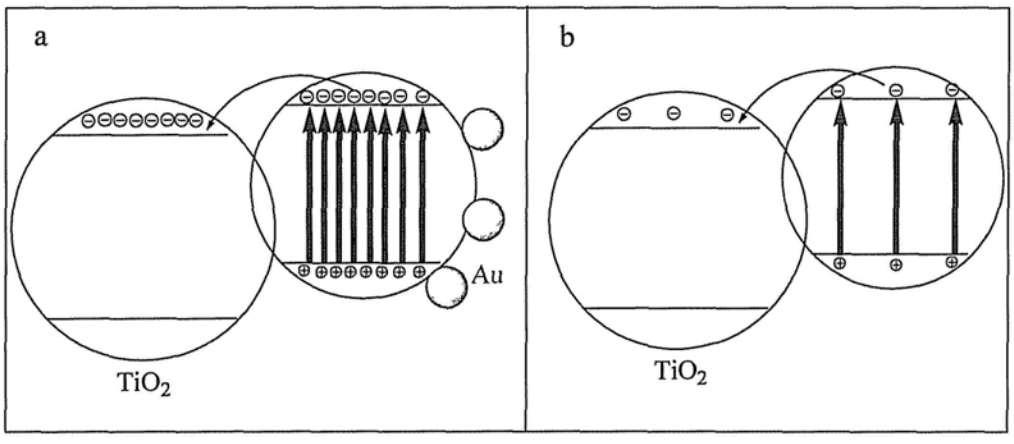

Figure 2.13 Schematic diagram representing the inter-particle charge transfer process in TNAs/CdS and TNAs/CdS/Au composite.

2.4 Conclusions

A surface modification approach has been used for the fabrication of TNAs/CdS/Au composite. According to the photocatalytic activity investigations, TNAs/CdS/Au composite exhibits higher efficiency than TNAs/CdS. The enhancement is because of the plasmon-enhanced optical absorption.

2.5 References

[1] Dong, F.; Wang, H. Q.; Sen, G.; Wu, Z. B.; Lee, S. C. *J. Hazard. Mater.*, **2011**, *187*, 509.

[2] Chen, X.; Mao, S. S. *Chem. Rev.*, **2007**, *107*, 2891.

[3] Xiang, Q. J.; Yu, J. G.; Jaroniec, M. *Chem. Commun.*, **2011**, *47*, 4532.

[4] Mor, G. K.; Kim, S.; Paulose, M.; Varghese, O. K.; Shankar, K.; Basham, J.; Grimes, C. A. *Nano Lett.*, **2009**, *9*, 4250.

[5] Allam, N. K.; Grimes, C. A. *Langmuir*, **2009**, *25*, 7234.

[6] Allam, N. K.; Grimes, C. A. *J. Phys. Chem. C*, **2009**, *113*, 7996.

[7] Yoriya, S.; Grimes, C. A. *J. Mater. Chem.*, **2011**, *21*, 102.

[8] Mor, G. K.; Shankar, K.; Paulose, M.; Varghese, O. K.; Grimes, C. A. *Nano Lett.*, **2006**, *6*, 215.

[9] Shankar, K.; Mor, G. K.; Prakasam, H. E.; Varghese, O. K.; Grimes, C. A. *Langmuir*, **2007**, *23*, 12445.

[10] Yoriya, S.; Paulose, M.; Varghese, O. K.; Mor, G. K.; Grimes, C. A. *J. Phys. Chem. C*, **2007**, *111*, 13770.

[11] Prakasam, H. E.; Shankar, K.; Paulose, M.; Varghese, O. K.; Grimes, C. A. *J. Phys. Chem. C*, **2007**, *111*, 7235.

[12] Park, J. H.; Kim, S.; Bard, A. J. *Nano Lett.*, **2006**, *6*, 24.

[13] Xu, J. J.; Ao, Y. H.; Chen, M. D.; Fu, D. G. *Appl. Surf. Sci.*, **2010**, *256*, 4397.

[14] Lu, N.; Zhao, H. M.; Li, J. Y.; Quan, X.; Chen, S. *Sep. Purif. Technol.*, **2008**, *62*, 668.

[15] Zhang, S. S.; Peng, F.; Wang, H. J.; Yu, H.; Zhang, S. Q.; Yang, J. A.; Zhao, H. J. *Catal. Commun.*, **2011**, *12*, 689.

[16] Tu, Y. F.; Huang, S. Y.; Sang, J. P.; Zou, X. W. *Mater. Res. Bull.*, **2010**, *45*, 224.

[17] Liu, H. J.; Liu, G. G.; Zhou, Q. X. *J. Solid State Chem.*, **2009**, *182*, 3238.

[18] Zhu, W.; Liu, X.; Liu, H. Q.; Tong, D. L.; Yang, J. Y.; Peng, J. Y. *J. Am. Chem. Soc.*, **2010**, *132*, 12619.

[19] Shin, K.; Il Seok, S.; Im, S. H.; Park, J. H. *Chem. Commun.*, **2010**, *46*, 2385.

[20] Wu, L.; Yu, J. C.; Fu, X. Z. *J. Mol. Catal. A: Chem.*, **2006**, *244*, 25.

[21] Yu, J. C.; Wu, L.; Lin, J.; Li, P. S.; Li, Q. *Chem. Commun.*, **2003**, 1552.

[22] Gao, X. F.; Sun, W. T.; Hu, Z. D.; Ai, G.; Zhang, Y. L.; Feng, S.; Li, F.; Peng, L. M. *J. Phys. Chem. C*, **2009**, *113*, 20481.

[23] Wang, C. L.; Sun, L.; Yun, H.; Li, J.; Lai, Y. K.; Lin, C. J. *Nanotechnology*,

2009, *20*, 295601.

[24] Maier, S. A.; Brongersma, M. L.; Kik, P. G.; Meltzer, S.; Requicha, A. A. G.; Atwater, H. A. *Adv. Mater.*, **2001**, *13*, 1501.

[25] Vanduyne, R. P.; Hulteen, J. C.; Treichel, D. A. *J. Chem. Phys.*, **1993**, *99*, 2101.

[26] Sha, M. Y.; Xu, H.; Penn, S. G.; Cromer, R. *Nanomedicine*, **2007**, *2*, 725.

[27] Jung, J. M.; Wang, M.; Kim, E. J.; Park, C.; Hahn, S. H. *Appl. Catal., B*, **2008**, *84*, 389.

[28] Cheng, B.; Le, Y.; Yu, J. G. *J. Hazard. Mater.*, **2010**, *177*, 971.

[29] Ma, Y. S.; Chang, C. N.; Chiang, Y. P.; Sung, H. F.; Chao, A. C. *Chemosphere*, **2008**, *71*, 998.

[30] Schaadt, D. M.; Feng, B.; Yu, E. T. *Appl. Phys. Lett.*, **2005**, *86*, 063106.

[31] Rand, B. P.; Peumans, P.; Forrest, S. R. *J. Appl. Phys.*, **2004**, *96*, 7519.

[32] Hou, Y.; Li, X. Y.; Zhao, Q. D.; Quan, X.; Chen, G. H. *Adv. Funct. Mater.*, **2010**, *20*, 2165.

[33] Lin, C. J.; Yu, Y. H.; Liou, Y. H. *Appl. Catal., B*, **2009**, *93*, 119.

[34] Xie, Y.; Ali, G.; Yoo, S. H.; Cho, S. O. *ACS Appl. Mater. Interfaces*, **2010**, *2*, 2910.

[35] Yin, Y. X.; Jin, Z. G.; Hou, F. *Nanotechnology*, **2007**, *18*, 495608.

[36] Panoiu, N. C.; Osgood, R. M. *Opt. Lett.*, **2007**, *32*, 2825.

[37] Qu, D.; Liu, F.; Yu, J. F.; Xie, W. L.; Xu, Q.; Li, X. D.; Huang, Y. D. *Appl.*

Phys. Lett., **2011**, *98*.

[38] Nakayama, K.; Tanabe, K.; Atwater, H. A. *Appl. Phys. Lett.*, **2008**, *93*.

[39] Lieberman, I.; Shemer, G.; Fried, T.; Kosower, E. M.; Markovich, G. *Angew. Chem. Int. Ed.*, **2008**, *47*, 4855.

Chapter Three

Cu_2ZnSnS_4 Nanocrystals Embedded Mesoporous TiO_2 as a New Visible Light-induced Photocatalyst

3.1 Introduction

In recent years a great deal of effort has been focused on the semiconductor-induced photocatalysis for environmental applications such as air purification,[1-3] water disinfection,[4-6] hazardous waste decomposition.[7-10] Titanium dioxide is the most widely used photocatalyst because of its superior photoreactivity, nontoxicity, high photocorrosion resistance and low price.[11-15] Various strategies have been developed to enhance photocatalytic activity of TiO_2-based materials, such as doping different elements,[16-18] surface modification,[19-21] etc. Incorporating pores in bulk materials is a promising approach.[22-24] The porous architectures with large surface area and interwoven porous network would improve the photoabsorption and the mass-transfer of materials, resulting in enhanced photocatalytic activity.[22-24]

However the TiO_2 photocatalyst generally suffers from a relatively low quantum efficiency due to its large band gap. It can only be activated by ultraviolet irradiation, which only occupies 4% of the solar radiation. As a result, the abundant visible light in solar spectrum or artificial light sources cannot be

utilized. The development of broad spectral photocatalyst, especially visible light-driven photocatalysts, attracted great attention in photocatalysis research.[25, 26]

Coupling a small bandgap semiconductor with TiO_2 is an effective method to realize visible light photocatalysis.[27-29] The enhanced photocatalytic activity is beneficial from two unique properties of the composite semiconductor. The first important feature of the coupled semiconductor system is that the photo-generated electrons and holes can transfer from one semiconductor to another. Thus the recombination rate of the pair was decreased. Another one is that the small band gap semiconductor help TiO_2 absorb visible light.

Cu_2ZnSnS_4 (CZTS) composed of earth abundant and non-toxic elements has received wide research interests because of its potential as an absorber material for solar energy applications.[30-32] The small bandgap (1.4-1.6eV) and large absorption coefficient (up to 10^4 cm^{-1}) make it an excellent candidate for the application of thin-film solar cells.[33, 34] Katagiri and co-workers have fabricated CZTS thin film solar cells by sputtering and vapor deposition techniques with efficiencies of up to 6.7%.[35] CZTS thin films have also been applied as photoelectrodes for H_2 evolution from water under solar light. And the solar energy conversion efficiency in H_2 production using modified CZTS reached 1.2%.[36, 37] However CZTS has not been reported as a photocatalyst to decompose pollutants. It might be due to the short life time of photogenerated electrons and

the weak oxidation ability of the photogenerated holes.

Herein we reported a new efficient and stable visible light driven-photocatalyst, in which CZTS nanocrystals were incorporated into mesoporous TiO_2. The introduction of CZTS nanocrystals into the TiO_2 mesoporous structure can extend the photoresponse of TiO_2 to the visible-light region. And enhanced visible-light photocatalytic performance is therefore realized.

3.2 Experimental Section

3.2.1 Synthesis of CZTS nanocrystals[38]

In a typical reaction, 0.26 g of $Cu(AcAc)_2$ (99.9%), 0.109 g of $Zn(Ac)_2.2H_2O$ (99.9%), 0.1128 g of $SnCl_2.2H_2O$ (99.9%), 0.065 g of S (99.9%) were added to 20 mL of oleylamine (70%) in a 100 mL three-neck flask. The reaction mixture was degassed under vacuum for 2 h, purged with argon for 30 min at 110 °C, heated to 280 °C for 1 h, and then cooled to room temperature. The nanocrystals were then isolated by precipitation with ethanol followed by centrifugation. Solid reaction byproducts and poorly capped nanocrystals were removed by redispersion in cyclohexane and centrifugation at 10000 rpm for 2 min. The nanocrystals were washed three more times by solvent/ antisolvent precipitation with cyclohexane/ethanol. A typical reaction yielded about 100 mg of nanocrystals.

3.2.2 Synthesis of TiO_2/CZTS composites

In a typical synthesis procedure, 0.5 g of poly(alkyleneoxide) block copolymer (Pluronic F-127, BASF) was dissolved in 6 mL of ethanol (EtOH) containing 0.05 g of CZTS nanocrystals. To this solution was added 0.6 ml of titanium tetrachloride (Aldrich) under vigorous stirring for 0.5 h. The resulting sol solution was gelled in an open Petri dish at 40 °C in air for 1 day. The as-prepared sample was then calcined at 400 °C for 4 h in air. Finally, 0.4356g of gray powder was obtained. Thus the ratio of CZTS in the composite is about 11%.

3.2.3 Materials Characterization

TEM images and EDX profiles were taken on a Philips CM-120 electron microscopy instrument coupled with an energy-dispersive X-ray (EDX) spectrometer. Samples were dispersed into to cyclohexane and were dropped onto a carbon-coated gold grid followed by solvent evaporation in air at room temperature. X-ray diffraction (XRD) patterns were recorded using a Bruker D8 Advance diffractometer with high-intensity Cu $K\alpha_1$ irradiation (λ=1.5406 Å). UV-vis spectra were recorded on a Varian Cary 100 Scan UV-visible system. X-ray photoelectron spectroscopy (XPS, Versa Probe PHI 5000) was employed to determine surface electronic states. The shift of the binding energy due to relative surface charging was corrected using the C_{1S} level at 284.8 eV as an internal standard. The N_2-sorption isotherms were recorded at 77 K in a Micromeritics

ASAP 2010 instrument. All the samples were degassed at 150 °C and 10^{-6} Torr for 24 h prior to the measurement. The Brunauer-Emmett-Teller approach was used to determine the surface area. The diffuse reflectance spectra of the samples over a range of 200-800 nm were recorded by a Varian Cary 100 Scan UV-vis system equipped with a Labsphere diffuse reflectance accessory.

3.2.4 Photocatalytic Degradation of Rhodamine B

Rhodamine B was considered as a model contaminant to test the photocatalytic activity of the samples. Briefly, the prepared CZTS, TiO_2/CZTS and pure TiO_2 were placed on the bottom of the beaker containing 20 mL Rhodamine B aqueous solution (10 ppm). Above the beaker a 300W tungsten halogen lamp with a 400 nm cutoff filter was used as visible light source. After 12 h of adsorption/desorption equilibrium, the photocatalytic degradation of methylene blue was initiated. Photodegradation was monitored by measuring the absorbance of the solution at 553 nm.

3.3 Results and Discussion

3.3.1 TEM and EDX analysis

The morphology and size of the prepared samples are investigated by TEM and EDX analysis. Figure 3.1a and b show typical TEM images of pure CZTS nanocrystals. The particles have an average diameter of 20nm. A typical EDX

spectrum of the particles is shown in Figure 3.1e. The average composition of the nanocrystals determined by EDX analysis of 20 nanocrystals is $Cu_{2.07}Zn_{1.00}Sn_{1.28}S_{3.82}$. The slightly tin rich and sulfur-deficient nature is similar to the reported phenomenon.[38] The signal of gold in the spectrum comes from the carbon-coated gold grid. To facilitate electron transfer, mesoporous TiO_2 was selected to load CZTS nanoparticles. From Figure 3.1c and d it can be clearly observed that many nanoparticles distributed evenly into the mesoporous TiO_2. The corresponding EDX analysis confirms the presence of CZTS (Figure 3.1f). It indicates the formation of TiO_2/CZTS composite.

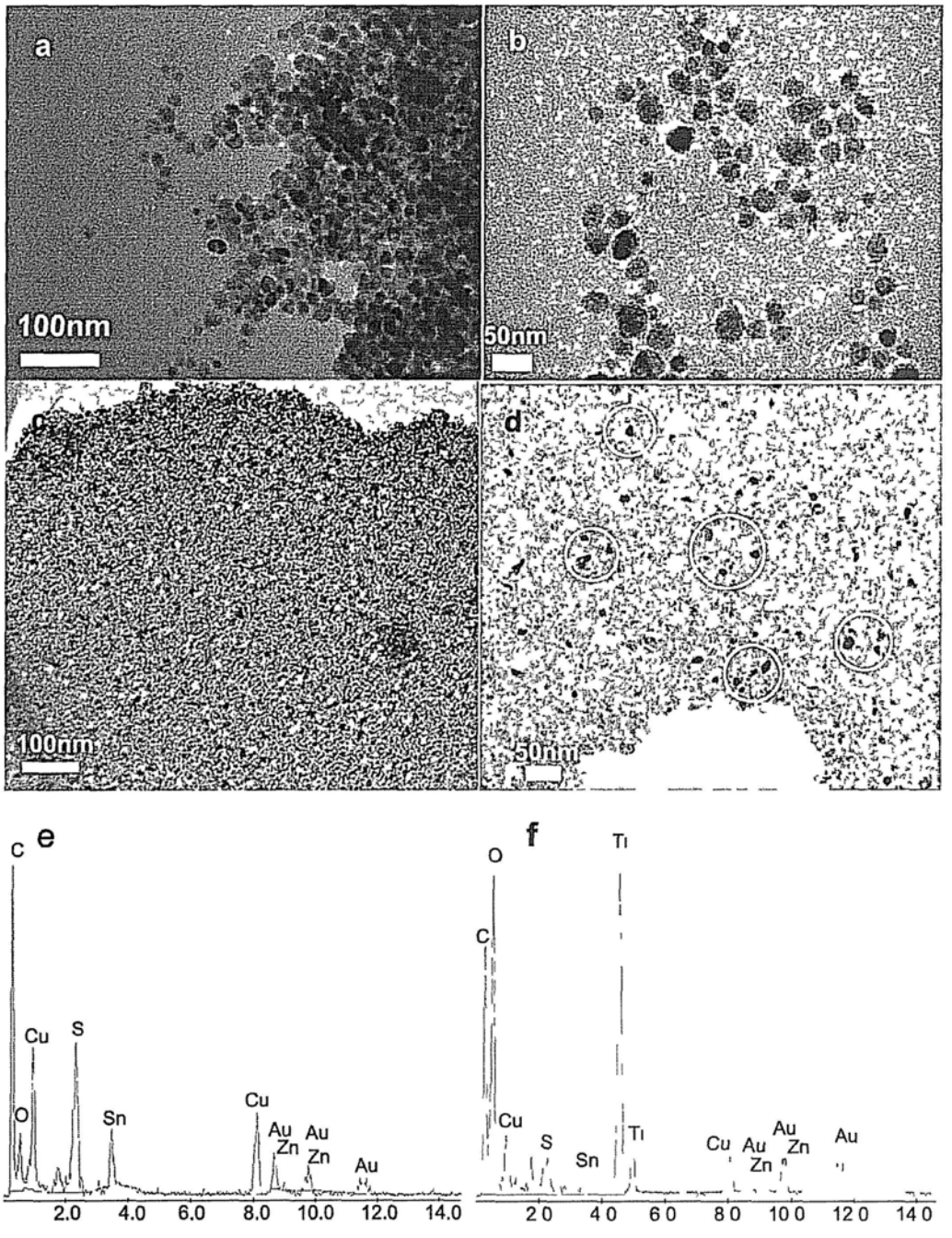

Figure 3.1 TEM images and EDX analysis of CZTS nanocrystals (a, b, e) and TiO_2/CZTS composite (c, d, f).

3.3.2 XRD Measurements

X-ray diffraction (XRD) was used to identify the crystalline phase of the CZTS and TiO_2/CZTS sample. As shown in Figure 3.2a the prepared CZTS nanocrystals are indexed to the typical kesterite structure. Kesterite is composed of a tetragonal unit cell, with sulfur atoms located in a face centered- cubic sublattice.[38] The Cu, Zn, and Sn atoms occupy half the tetrahedral interstitial sites within the S sublattice, with compositional order. Figure 3.2b presents the XRD pattern of TiO_2/CZTS composite. The diffraction peaks at 2θ of 25.2, 37.9, 48.1, 53.8, 55.4, 62.6, and 75.3° are attributed to anatase-TiO_2 (JCPDF 21-1272). The diffraction peak at 2θ of 28.2° is corresponding to the (112) crystal plane of CZTS, as seen in Figure 3.2c. The other diffraction peaks of CZTS can not clearly be observed because they overlapped with that of anatase TiO_2.

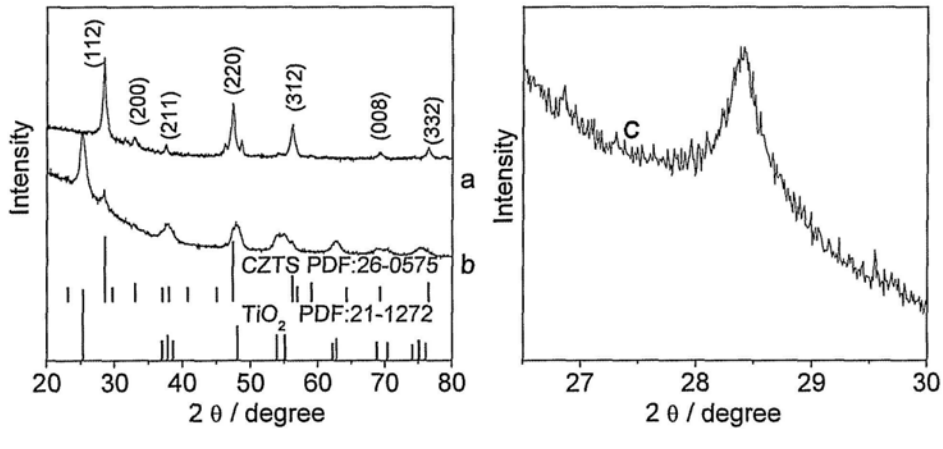

Figure 3.2 XRD patterns of CZTS (a) and TiO_2/CZTS (b, c). (c) is the fine scan within 26.5 and 30 degree.

3.3.3 UV-visible Spectra

UV-visible diffuse reflectance spectroscopy (DRS) was performed to determine the electronic states of the as prepared samples. Figure 3.3 shows the UV-visible absorption spectra of mesoporous TiO_2, CZTS and TiO_2/CZTS samples. As a large energy gap semiconductor (3.2 eV), the pure anatase TiO_2 shows significant absorbance in the UV region (Figure 3.3a). The absorption onset of the small bandgap semiconductor CZTS is extended to 800nm (Figure 3.3b). As shown in Figure 3.3c, the TiO_2/CZTS composite exhibits a broad absorption bands in UV-visible region within 300 and 800 nm, suggesting the effective photoabsorption property for the composite photocatalyst system. The visible light absorption property provides clear evidence for the formation of CZTS nanocrystals embedded in the mesoporous TiO_2. The enhanced ability to absorb visible-light makes it a promising photocatalyst for solar-driven applications.

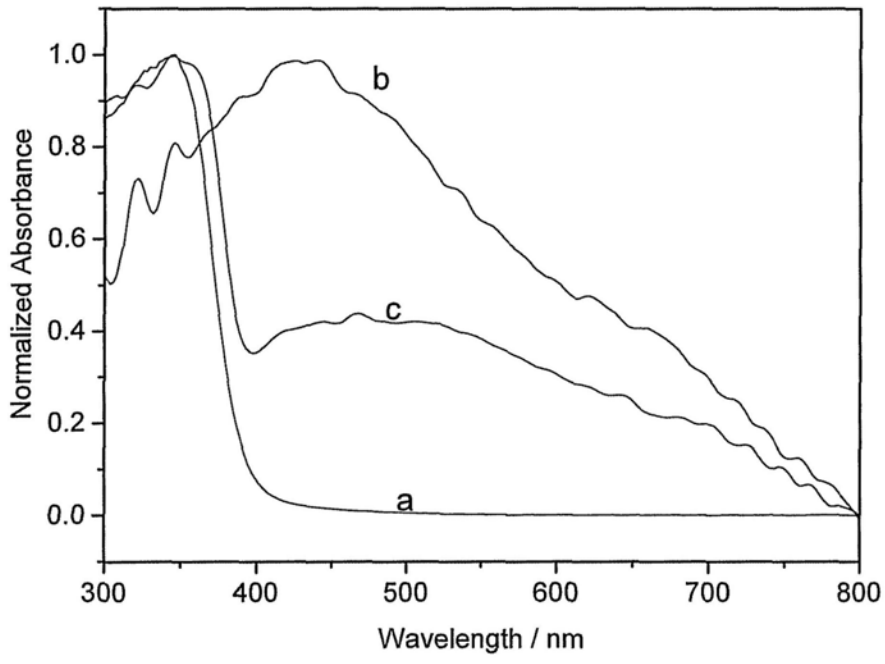

Figure 3.3 UV-visible absorption spectra of (a) Pure TiO_2, (b) CZTS and (c) TiO_2/CZTS

3.3.4 BET Analysis

To study the porous structure, N_2 adsorption-desorption isotherm was investigated. Figure 3.4 shows the pore size distribution plots and N_2-sorption isotherms (inset) for the mesoporous TiO_2 and TiO_2/CZTS. Both samples show typical type-IV curves of mesoporous materials. Brunauer-Emmett-Teller (BET) method was used to determine the specific surface area and pore volume. For pure TiO_2 they are 136 m^2g^{-1} and 0.17 m^3g^{-1}, respectively. According to the desorption branch of the isotherm, the mean pore diameter is determined to be 6.4 nm with a narrow distribution.

The TiO_2/CZTS composite exhibits a specific surface area of 123 m^2g^{-1} and a pore volume of 0.2 m^3g^{-1}. The average pore diameter is about 4.8, which could be considered to be identical with the pure TiO_2 sample because of a typical uncertainty of 5% for BET surface area measurements.

The BET results also demonstrate that after embedding CZTS, the mesoporous structure of TiO_2 was not destroyed. Such mesoporous architecture with large surface area plays an important role in catalyst design for its being able to improve the molecular transport of reactants and products.

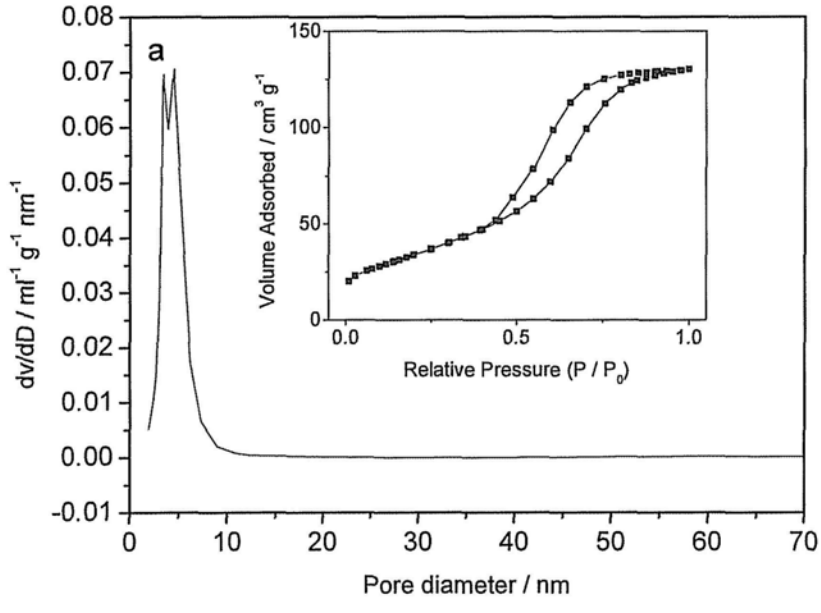

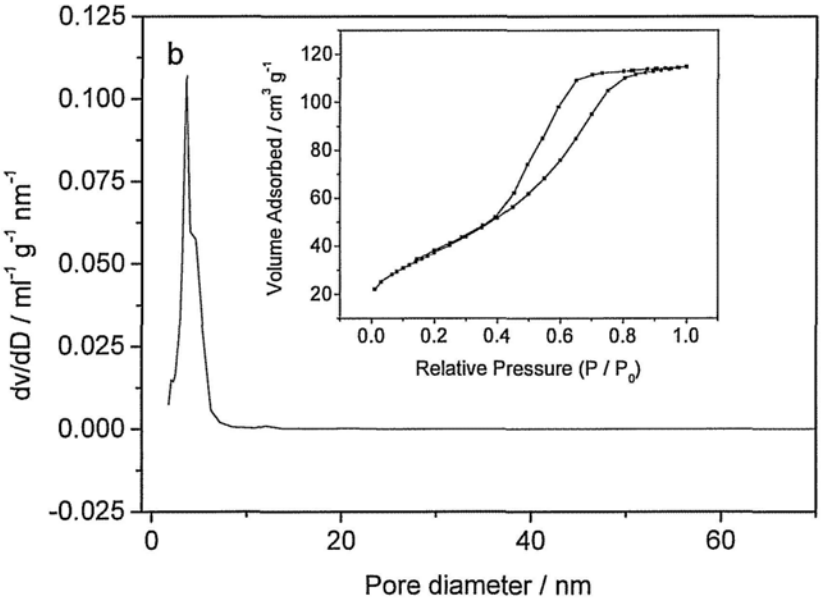

Figure 3.4 N_2 adsorption-desorption isotherms (inset) and corresponding pore-size distribution curves for pure TiO_2 (a) and TiO_2/CZTS (b). The pore-size distribution was determined from desorption branch of the isotherm.

3.3.5 Photocatalytic activity

In order to evaluate the photocatalytic activity of the samples, the degradation of Rhodamine B was used as a probe photoreaction. Results of the photocatalytic evaluation are summarized in Figure 3.5. It is clear that the TiO_2/CZTS composite exhibit high photocatalytic activity under visible light irradiation. And the degradation follows a first-order rate law. Both pure TiO_2 and CZTS show no activity for the degradation of Rhodamine B under visible light.

To investigate the recyclability of the TiO_2/CZTS photocatalyst, the sample powders after the photocatalytic reactions were collected by centrifugation and

dried for the subsequent photoreaction cycle. As shown in Figure 3.6, the TiO_2/CTTS composite shows excellent stability and maintain a similar level of photocatalytic activity after three reaction cycles.

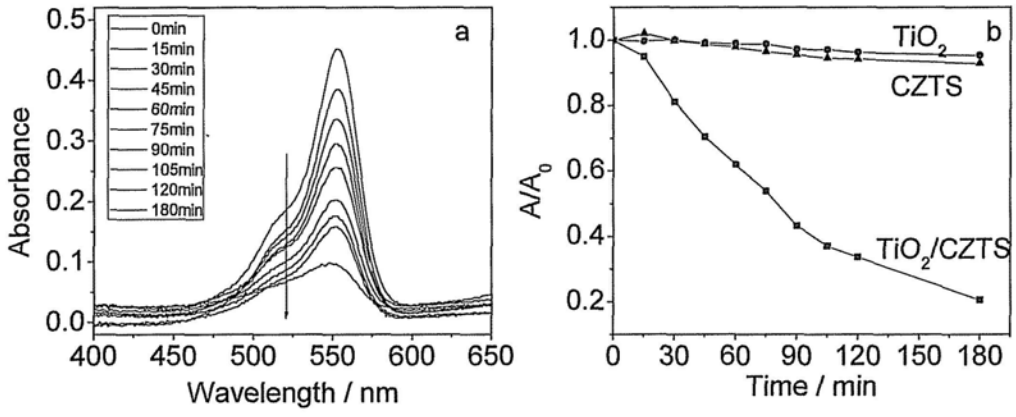

Figure 3.5 (a) Time-dependent absorption spectra of Rhodamine B (10ppm) solution containing TiO_2/CZTS composite under visible light irradiation ($\lambda > 400$ nm). (b) A comparison of the photoactivities for TiO_2, CZTS and TiO_2/CZTS. A is the absorbance of Rhodamine B (λ_{max} = 553 nm) and A_0 is the initial absorbance.

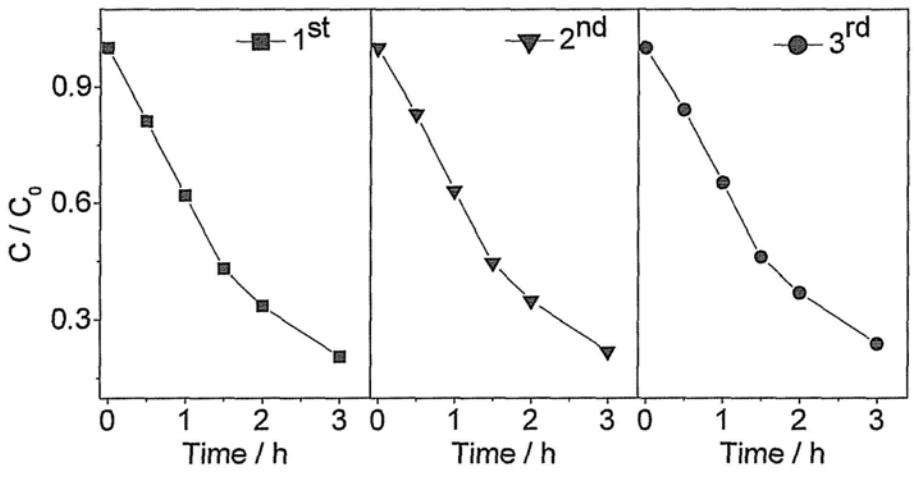

Figure 3.6 The cyclability of photocatalytic activity for TiO_2/CZTS

3.3.6 Photocatalysis Mechanism

Due to its low bandgap the embedded CZTS nanocrystals could absorb visible light photons to produce electron-hole pair. Although the absorption coefficient of CZTS is very large, the visible light photocatalytic activity of pure CZTS is very weak. It might be due to two reasons. The potential of photogenerated holes in the conduction bands are too positive to oxidize pollutant molecules. And the recombination of the electron-hole pair is very quick. The TiO_2/CZTS composite exhibit enhanced photocatalytic activity. It is because the appropriate energy levels of the conduction and valence bands allow CZTS to act as sensitizers for visible light photocatalysis (Figure 3.7). Under visible light irradiation, the photogenerated electrons in the conduction band of CZTS are quickly injected into that of TiO_2 and accumulate at the lower-lying conduction band of TiO_2. Thus

efficient charge separation is achieved. Consequently, the photo-generated electron is scavenged by the oxygen in water, hence forming highly reactive free radicals to degrade pollutant molecules.

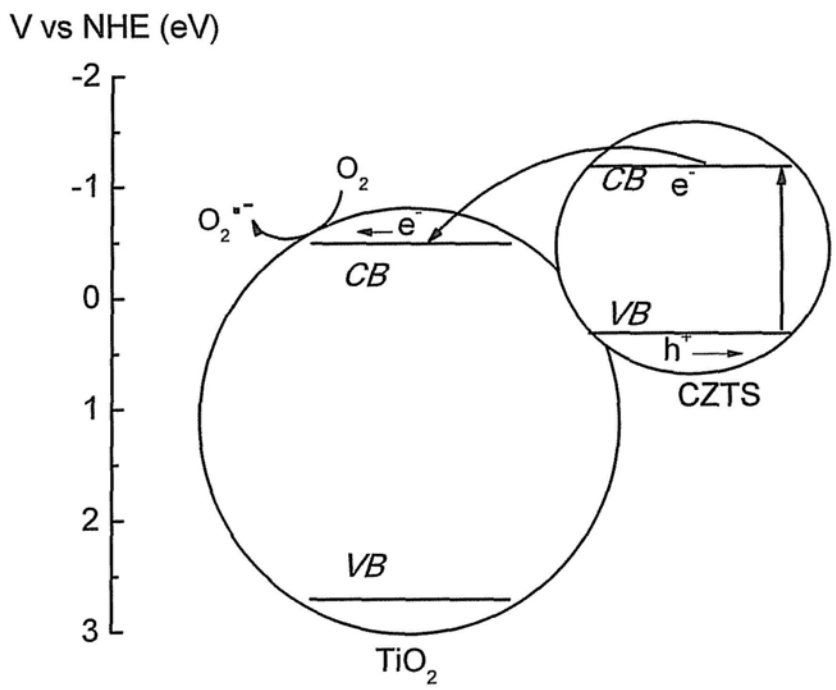

Figure 3.7 Schematic diagram representing the inter-particle charge transfer process in a TiO_2/CZTS composite.

3.4 Conclusions

As a novel low band gap semiconductor, CZTS nanocrystals were incorporated into mesoporous TiO_2. The prepared TiO_2/CZTS composite exhibits excellent photocatalytic activity and photostability under visible light irradiation. This study

demonstrates semiconductor composite is a promising system to realize broad spectral photocatalysis.

3.5 References

[1] Besov, A. S.; Vorontsov, A. V.; Parmon, V. N. *Appl. Catal., B*, **2009**, *89*, 602.

[2] Sarantopoulos, C.; Puzenat, E.; Guillard, C.; Herrmann, J. M.; Gleizes, A. N.; Maury, F. *Appl. Catal., B*, **2009**, *91*, 225.

[3] Mo, J. H.; Zhang, Y. P.; Xu, Q. J.; Lamson, J. J.; Zhao, R. Y. *Atmos. Environ.*, **2009**, *43*, 2229.

[4] Villen, L.; Manjon, F.; Garcia-Fresnadillo, D.; Orellana, G. *Appl. Catal., B*, **2006**, *69*, 1.

[5] Paleologou, A.; Marakas, H.; Xekoukoulotakis, N. P.; Moya, A.; Vergara, Y.; Kalogerakis, N.; Gikas, P.; Mantzavinos, D. *Catal. Today*, **2007**, *129*, 136.

[6] Zhang, D. Q.; Li, G. S.; Yu, J. C. *J. Mater. Chem.*, **2010**, *20*, 4529.

[7] Zhang, D. Q.; Li, G. S.; Yang, X. F.; Yu, J. C. *Chem. Commun.*, **2009**, 4381.

[8] Li, G. S.; Zhang, D. Q.; Yu, J. C. *Chem. Mater.*, **2008**, *20*, 3983.

[9] Li, G. S.; Zhang, D. Q.; Yu, J. C. *Environ. Sci. Technol.*, **2009**, *43*, 7079.

[10] Li, G. S.; Zhang, D. Q.; Yu, J. C.; Leung, M. K. H. *Environ. Sci. Technol.*, **2010**, *44*, 4276.

[11] Chen, Y.; Dionysiou, D. D. *Appl. Catal., B*, **2006**, *69*, 24.

[12] Guillard, C.; Beaugiraud, B.; Dutriez, C.; Herrmann, J.-M.; Jaffrezic, H.; Jaffrezic-Renault, N.; Lacroix, M. *Appl. Catal., B*, **2002**, *39*, 331.

[13] Xiang, Q. J.; Yu, J. G.; Jaroniec, M. *Chem. Commun.*, **2011**, *47*, 4532.

[14] Chen, X.; Mao, S. S. *Chem. Rev.*, **2007**, *107*, 2891.

[15] Dong, F.; Wang, H. Q.; Sen, G.; Wu, Z. B.; Lee, S. C. *J. Hazard. Mater.*, **2011**, *187*, 509.

[16] Higashimoto, S.; Azuma, M. *Appl. Catal., B*, **2009**, *89*, 557.

[17] Iliev, V.; Tomova, D.; Bilyarska, L.; Eliyas, A.; Petrov, L. *Appl. Catal., B*, **2006**, *63*, 266.

[18] Park, Y.; Kim, W.; Park, H.; Tachikawa, T.; Majima, T.; Choi, W. *Appl. Catal., B*, **2009**, *91*, 355.

[19] Dozzi, M. V.; Chiarello, G. L.; Selli, E. *J. Adv. Oxid. Technol.*, **2010**, *13*, 305.

[20] Libanori, R.; Giraldi, T. R.; Longo, E.; Leite, E. R.; Ribeiro, C. *J. Sol-Gel Sci. Technol.*, **2009**, *49*, 95.

[21] Sharma, R.; Das, P. P.; Misra, M.; Mahajan, V.; Bock, J. P.; Trigwell, S.; Biris, A. S.; Mazumder, M. K. *Nanotechnology*, **2009**, *20*, 075704.

[22] Yu, J. G.; Wang, W. G.; Cheng, B. *Chem-Asian J.*, **2010**, *5*, 2499.

[23] Wang, X. D.; Caruso, R. A. *J. Mater. Chem.*, **2011**, *21*, 20.

[24] Xu, X. J.; Fang, X. S.; Zhai, T. Y.; Zeng, H. B.; Liu, B. D.; Hu, X. Y.; Bando, Y.; Golberg, D. *Small*, **2011**, *7*, 445.

[25] Zhang, S. S.; Peng, F.; Wang, H. J.; Yu, H.; Zhang, S. Q.; Yang, J. A.; Zhao,

H. J. *Catal. Commun.*, **2011**, *12*, 689.

[26] Zhang, Y. L.; Schultz, A. M.; Salvador, P. A.; Rohrer, G. S. *J. Mater. Chem.*, **2011**, *21*, 4168.

[27] Zhang, L. S.; Wong, K. H.; Chen, Z. G.; Yu, J. C.; Zhao, J. C.; Hu, C.; Chan, C. Y.; Wong, P. K. *Appl. Catal., A*, **2009**, *363*, 221.

[28] Ho, W. K.; Yu, J. C. *J. Mol. Catal. A: Chem.*, **2006**, *247*, 268.

[29] Li, G. S.; Zhang, D. Q.; Yu, J. C. *Phys. Chem. Chem. Phys.*, **2009**, *11*, 3775.

[30] Riha, S. C.; Parkinson, B. A.; Prieto, A. L. *J. Am. Chem. Soc.*, **2009**, *131*, 12054.

[31] Paier, J.; Asahi, R.; Nagoya, A.; Kresse, G. *Phys. Rev. B: Condens. Matter*, **2009**, *79*, 115126.

[32] Kumar, Y. B. K.; Babu, G. S.; Bhaskar, P. U.; Raja, V. S. *Sol. Energy Mater. Sol. Cells*, **2009**, *93*, 1230.

[33] Guo, Q. J.; Hillhouse, H. W.; Agrawal, R. *J. Am. Chem. Soc.*, **2009**, *131*, 11672.

[34] Tanaka, K.; Oonuki, M.; Moritake, N.; Uchiki, H. *Sol. Energy Mater. Sol. Cells*, **2009**, *93*, 583.

[35] Katagiri, H.; Jimbo, K.; Yamada, S.; Kamimura, T.; Maw, W. S.; Fukano, T.; Ito, T.; Motohiro, T. *Appl. Phys. Express*, **2008**, *1*, 041201.

[36] Yokoyama, D.; Minegishi, T.; Jimbo, K.; Hisatomi, T.; Ma, G. J.; Katayama, M.; Kubota, J.; Katagiri, H.; Domen, K. *Appl. Phys. Express*, **2010**, *3*, 101202.

[37] Ma, G. J.; Minegishi, T.; Yokoyama, D.; Kubota, J.; Domen, K. *Chem. Phys. Lett.*, **2011**, *501*, 619.

[38] Steinhagen, C.; Panthani, M. G.; Akhavan, V.; Goodfellow, B.; Koo, B.; Korgel, B. A. *J. Am. Chem. Soc.*, **2009**, *131*, 12554.

Chapter Four

Synthesis, Characterization and Potential Applications of Porous Upconversion Materials

4.1 Introduction

Upconversion fluorescent materials can emit visible (and even UV) light upon near-infrared (NIR) excitation via the sequential absorption of two or more low-energy photons.[1, 2] In the last decade, great progress has been made in the preparation of upconversion materials, which can emit visible light by absorbing two or more near-infrared (NIR) photons. This endows upconversion with many advantages, such as low background light, high sensitivity for detection, high photo-stability, reduced instrument cost and high light penetration depth.[3, 4] Such wonderful properties have already rendered upconversion materials very attractive uses in solid-state lasers,[5] NIR quantum counting devices,[6] 3D flat-panel displays,[7] biotechnology.[8, 9] To date, lanthanide-doped $NaYF_4$ ($NaYF_4$:Yb,Er or Yb,Tm) is the most efficient upconversion material, in which the sensitizer (Yb^{3+}) absorbs NIR excitation light and the activator (Er^{3+}, Tm^{3+}) emits the upconversion fluorescence.[10] Much effort has been made in the synthesis of lanthanide-doped $NaYF_4$ nanocrystals with different morphology, size, emission intensity and color.[11-15] Recently researchers have demonstrated the use of upconversion

nanophosphors ($NaYF_4$:Yb,Er) for in vitro imaging of cancer cells and in vivo imaging in tissues.[16-19] Generally the materials must be modified to make them biocompatible before applying on the cells. Thus surface modification of upconversion nanocrystals has attracted considerable interests.[20-22] In addition, the detailed mechanisms for upconversion process have been investigated.[1, 2] And the fluorescence resonance energy transfer (FRET) from upconversion materials to downconversion fluorescent materials and metal nanoparticles has been explored.[23-25]

It is well known that FRET is a highly distance-dependent process. Due to the relatively large surface area porous materials could facilitate the contact between donors and acceptors. More recently few researchers focused on the preparation of porous upconversion nanomaterials. Qu synthesized macroporous ZrO_2:Yb,Er upconversion nanomaterials using polystyrene spheres as the template.[26] Zhang got ordered mesostructured LaF_3:Yb,Er upconversion nanowire arrays after removing silica templates.[27] These hard template-assisted approaches are rather laborious. Thus it is very important to develop more facile methods to prepare porous upconversion materials.

Photosynthesis is a process that converts light to chemical energy by plants, which is vital for life on earth. It begins with solar energy absorption by chlorophylls which can only absorb the red and blue light.[28, 29] The whole solar energy spectrum includes infrared (IR, 47%), visible (46%), and ultra-violet (UV,

6%) light. Since UV, IR and a large part of visible-light are not utilized in the photosynthesis process, the theoretical maximum conversion efficiency of solar energy in natural photosynthesis is approximately 10%. The actual efficiency is only about 3~6% due to reflection and respiration. The efficiency becomes even lower during cloudy days and nights when the light distributes mainly within 800~1300 nm.[28, 29] Many methods for improving photosynthetic efficiency have been developed. For example, supplemental lighting of suitable wavelength (especially the red light) has be used to promote plant growth.[30] Another approach is to convert UV or unused visible light (such as green light) to red or blue light to enhance absorption by chlorophylls.[31] However, the utilization of infrared light which constitutes almost half of the solar spectrum is still a formidable task.

Herein we report a facile one-step method for the preparation of $NaYF_4$:Yb,Er nanoporous upconversion materials through an oriented self-assembly process with coordination of sodium dodecyl sulfate (SDS). The effects of SDS concentration and reaction time on the morphology and size of the products were investigated. Experimental results reveal that SDS plays an important role in controlling the crystal phases, morphologies and sizes of the $NaYF_4$:Yb,Er products. And the upconversion luminescent properties for the obtained porous crystals have been investigated. The FRET process from the obtained $NaYF_4$:Yb,Er porous particles to chlorophylls has been demonstrated, which is the

foundation for NIR-driven photosynthesis research. The FRET process from the obtained $NaYF_4$:Yb,Er porous particles to methylene blue molecules has also been investigated, indicating a novel approach for photodynamic therapy. The ability of the porous upconversion crystals to adsorb protein molecules was studied.

4.2 Experimental Section

All the chemicals used in the present work were of reagent grade and purchased from Sigma-Aldrich without further purification. Ultrapure Milli-Q water was used in all experiments.

4.2.1 Synthesis of $NaYF_4$:Yb,Er particles

In a typical procedure, $Y(NO_3)_3$ (0.264 mmol), $Yb(NO_3)_3$ (0.03 mmol) and $Er(NO_3)_3$ (0.006 mmol) were dissolved into sodium dodecyl sulfate (SDS) solution (5 mL) under vigorous stirring. Then NaF solution (10 mL, 0.36M) was dropped into the above solution. After stirring for 0.5 h, the mixed solution was transferred into a autoclave (20 mL) and heated to 160 °C for 3 h and naturally cooled down to room temperature. White precipitates were collected from the solution after centrifugation, then placed in distilled water (50 mL) and incubated for 24 h. The transparent supernatant was removed. Then the obtained precipitates

were washed with ethanol and water for three times, respectively, and dried in a vacuum at 80 °C for 48 h.

4.2.2 Extraction of chlorophylls

In order to get close to the natural system, the chlorophylls was just simply extracted without further separation. 100 g of spinach leaves were selected and ground. Then 50 ml ethanol was added. An hour later, the supernatant was centrifugated to obtain the original chlorophylls solution. Then the original chlorophylls solution was diluted for 2 or 5 times, respectively (denoted as ×1/2 and ×1/5 chlorophylls).

4.2.3 Investigation of energy transfer from upconversion materials to chlorophylls

5 mg of $NaYF_4$:Yb,Er particles was added into 1 mL of ethanol, followed by the addition of different volume of original chlorophylls. Here 0, 50, 100, 150, 200, 250, 300, 350, 400, 450, 500, 600, 700, 800, 900, 1000, 2000μL of chlorophylls was tried. And the corresponding upconversion fluorescence spectra were recorded. Then ×1/2 and ×1/5 chlorophylls was added into the $NaYF_4$:Yb,Er suspension, respectively. The other conditions were identical with the above experiments.

Control experiments: Pure ethanol was added into the $NaYF_4$:Yb,Er suspension, instead of chlorophylls. Here 0, 200, 400, 600, 800, 1000, 2000 μL of ethanol was tried.

4.2.4 Characterization

X-ray diffraction (XRD) patterns were carried out on a Bruker D8 Advance diffractometer with high-intensity Cu $K\alpha_1$ irradiation (λ=1.5406 Å). The general morphology of the products was characterized by a field-emission scanning electron microscope (FESEM, FEI, Quanta 400 FEG). TEM images were taken on a Philips CM-120 electron microscopy instrument. HRTEM images were obtained by employing a Tecnai F20 microscope (FEI, 200 kV).The Brunauer-Emmett-Teller (BET) surface area (SBET) and pore size distribution were determined by using a Micromeritics ASAP 2010 nitrogen adsorption apparatus. All the samples were degassed at 120 °C prior to BET measurements. Room temperature Upconversion fluorescence spectra were recorded on a Acton SpectraPro-300i monochromator integrated with an Princton Instruments thermoelectrically cooled CCD (TE/CCD-1024-E/1), which was cooled to -50 °C. A commercial IR laser working at 976.5 nm wavelength with tunable power was used for excitation. UV-vis spectra were recorded on a Varian Cary 500 Scan UV-visible system. Room-temperature fluorescence spectra of the pure chlorophylls were recorded on a Hitachi F-4500 fluorescence spectrophotometer.

4.3 Results and Discussion

4.3.1 Influence of Reaction Parameters on Particle Morphology and Structure

XRD patterns of the products obtained at different SDS concentrations are shown in Figure 4.1. Figure 4.1a corresponds to the case without SDS. According to the standard diffraction patterns (JCPDS Card No. 28-1192 for the hexagonal and 77-2042 for the cubic phase), the product prepared in the absence of SDS is a mixed phase composed of dominantly hexagonal and a small amount of cubic $NaYF_4$. The intensity ratio of hexagonal (110) to cubic (111) is 2.57. With increasing SDS concentration to 5 mM, the ratio decreases to 0.15 (Figure 4.1b), indicating that the predominant phase changes from hexagonal to cubic. At SDS concentrations of 10 mM or higher, pure cubic phase is obtained as shown in Figure 4.1c, d and e. It has been reported that cubic $NaYF_4$ is the kinetically stable product which is the main product at the early growth stage.[32-34] The long reaction time or high reaction temperature will cause the phase transformation from cubic to thermodynamically stable hexagonal phase. Apparently, SDS inhibits the phase transformation from cubic to hexagonal in our system.

In Figure 4.1c, d and e, the (111) diffraction peaks is used for the size estimation with Scherrer formula. The mean crystallite diameters are 28.3, 24.7

and 22.6 nm, respectively, indicating that the size of the product decreases with the increase of SDS concentration.

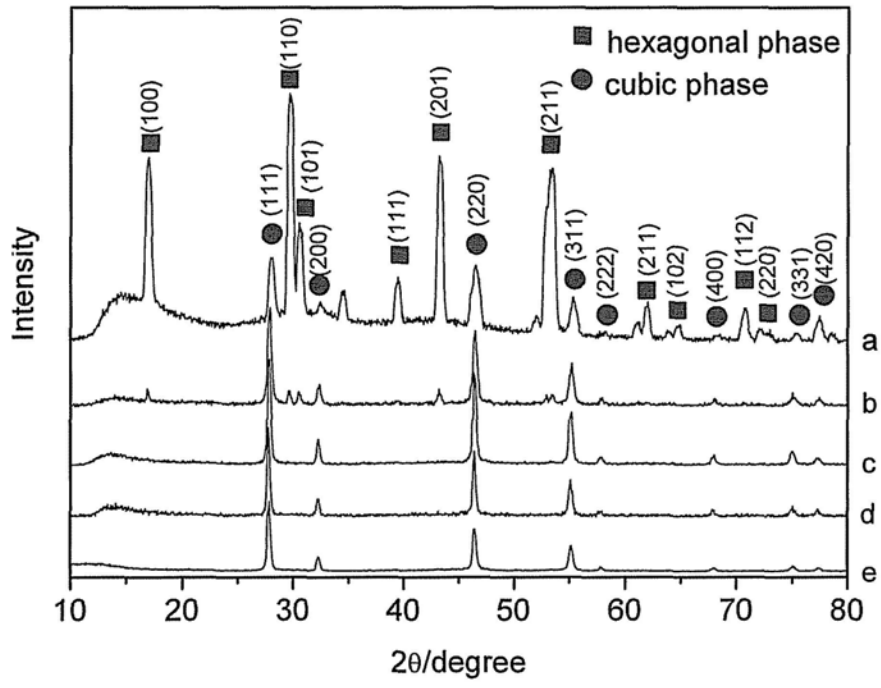

Figure 4.1 XRD patterns of $NaYF_4$: Yb,Er particles prepared at different SDS concentrations at 160 °C for 3 h: a) 0 mM, b) 5 mM, c)10 mM, d) 50 mM, e) 100 mM

The size and shape of the products are investigated by SEM and TEM. Figure 4.2 shows representative SEM images of the samples prepared at different SDS concentrations. For the case without SDS (Figure 4.2a, b), the product is composed of large microcrystals and many small particles with a diameter of 250 nm. As shown in the magnified image (Figure 4.2b), the surface of the small particles (cubic-like structure) is rather smooth. In the case with 5 mM SDS (Figure 4.2c, d), similar products are obtained except that the cubic-like particles show obvious porous structure. It can be observed from Figures 4.2e and f that increasing SDS to 10 mM causes the formation of pure porous cubic-like particles. Average diameter of the particles is about 250 nm. Figures 4.2g and h reveals that the products obtained at a high SDS concentration of 50 mM are uniform nanospheres with an average diameter of around 150 nm. It is clear that SDS plays a shape-controller role during the synthesis.

TEM images (Figure 4.3) provide more details about the porous structure. For the product prepared at 10mM of SDS (Figure 4.3a, b), the clear contrast difference in every individual particle represents the pores with size of about 20-30 nm. It is clear that every larger particle contains many primary nanoparticles with diameter of around 30 nm, which matches very well with the calculated result obtained from XRD measurements. It could be seen from Figure 4.3c that the $NaYF_4$: Yb, Er nanospheres prepared at 50mM of SDS are also

porous. However the pore size is smaller than 20 nm which is too small to be shown clearly in the SEM images.

According to XRD and morphology investigation, the microcrystals generated at low SDS concentrations correspond to the hexagonal phase, while small particles are cubic-phase structures.

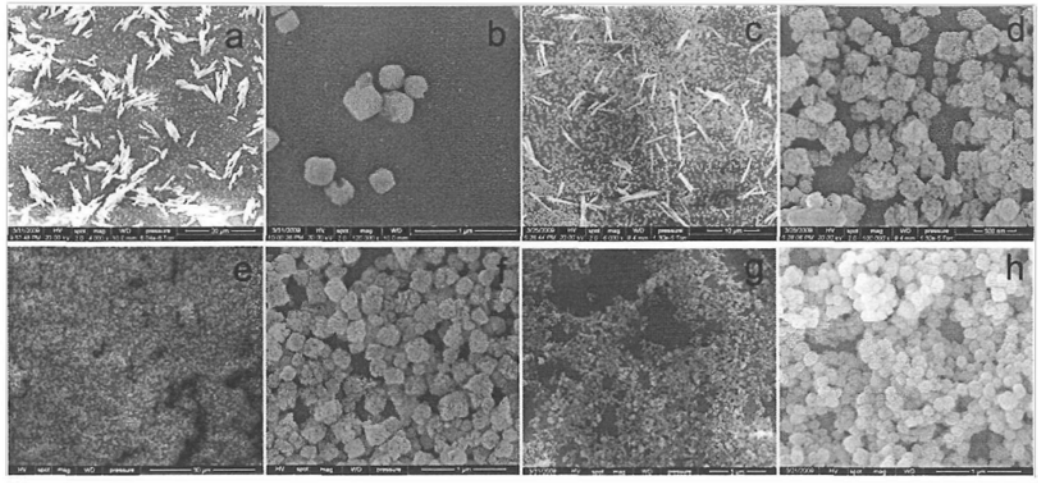

Figure 4.2 SEM images of the products obtained at different SDS concentrations: (a, b) 0 mM (c, d) 5 mM (e, f) 10 mM (g, h) 50 mM

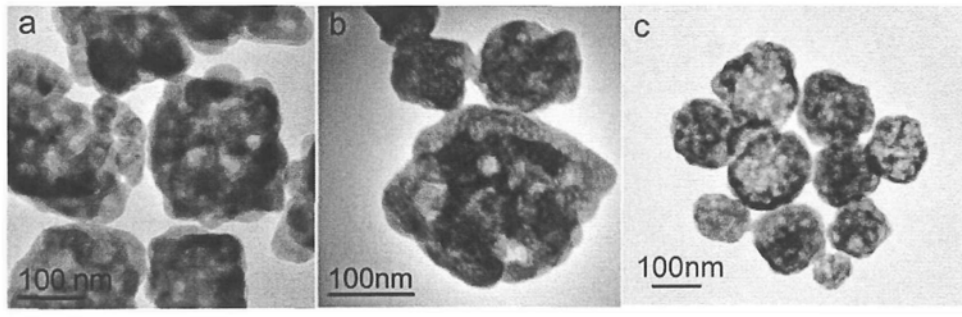

Figure 4.3 TEM images of $NaYF_4$:Yb,Er particles prepared at 160 °C for 3 h at different SDS concentrations: (a, b) 10 mM, (c) 50 mM.

HRTEM images provide further insight into the porous structure of the product. Figure 4.4a displays a representative TEM image of an individual particle. The selected area electron diffraction (SAED) pattern taken from the entire particle (the inset in Figure 4.4a) shows sharp diffraction spots indicating the formation of the single-crystalline structure with a high crystallinity. A representative HRTEM image from the selected area outlined by the white rectangle (part b) of the particle is shown in Figure 4.4b. According to the fast-Fourier transform (FFT) pattern, the HRTEM image is viewed from the [001] zone axis. The clear lattice fringes indicate high crystallinity and the measured lattice spacings of about 0.27 nm are from the {200} planes of the cubic phase $NaYF_4$ (JCPDS Card No. 77-2042). HRTEM images of different parts of the particle with the corresponding FFT patterns as the insets are shown in Figure 4.4c and d. FFT patterns selected from different areas are identical, further indicating the whole particle is a single crystal. The elemental composition of the formed product is confirmed by energy dispersive X-ray (EDX) microanalysis at the single-particle level (Figure 4.4e). It confirms the presence of Na, F, Y and the co-doped lanthanide Yb and Er.

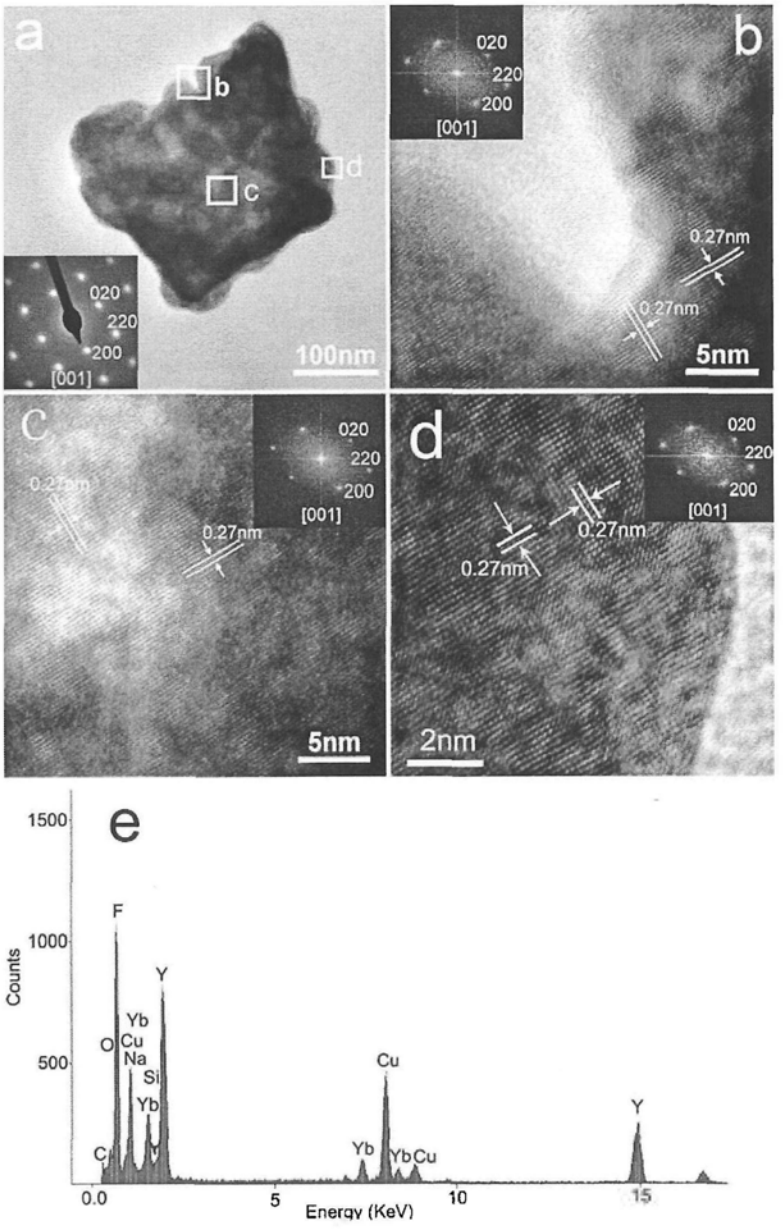

Figure 4.4 HRTEM images and EDX analysis of $NaYF_4$: Yb,Er particles prepared at 160 °C for 3 h (SDS=10 mM): (a) Low magnification TEM image. The inset is the electron diffraction pattern of the single particle. (b, c, d) HRTEM images from the areas outlined by the white rectangle in (a). The inset is the related fast-Fourier transforms. (e) EDX pattern of the particle

In order to investigate the formation process of the porous upconversion particles, products collected at different reaction times were subjected to SEM investigation. Figure 4.5 shows the corresponding SEM images of the products obtained at different growth stages. Before hydrothermal conditions, white gel-like product composed of many nanoparticles is obtained (Figures 4.5a, b). The diameter of the nanoparticles is smaller than 10 nm. XRD pattern (Figure 4.6a) indicates that these particles possess very low crystallinity. Porous structure is obtained at 3 h as described above. When the reaction time increased to 5 h (Figure 4.5c, d), fewer pores can be seen in the structure. This phenomenon is more obvious at the reaction time of 24 h (Figure 4.5e, f), in which nearly no pores can be seen in the particles. At this stage, there are also many microcrystals formed, which can be attributed to the formation of hexagonal phase (Figure 4.6b).

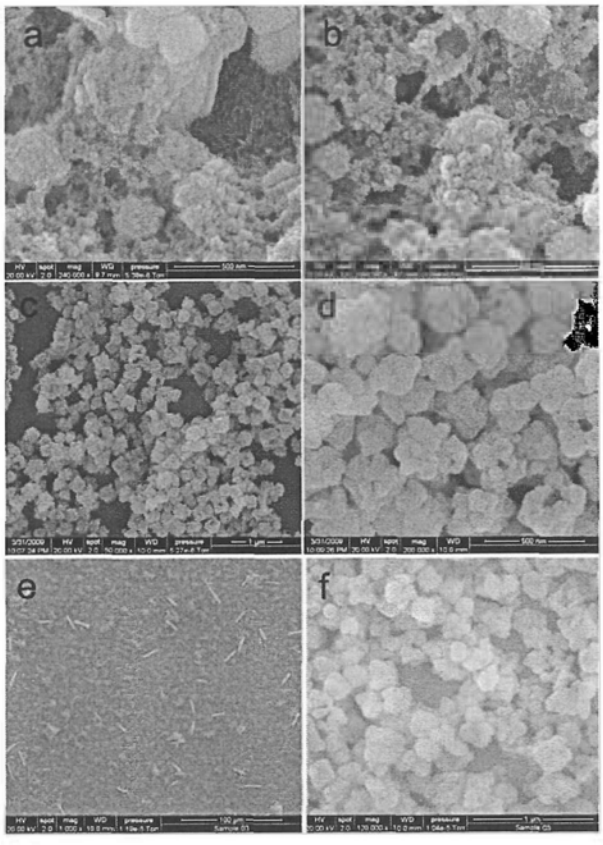

Figure 4.5 Time-dependent morphology evolution of the obtained $NaYF_4$:Yb,Er particles (160 °C, 10 mM SDS): (a, b) 0 h, (c, d) 5 h, (e, f) 24 h

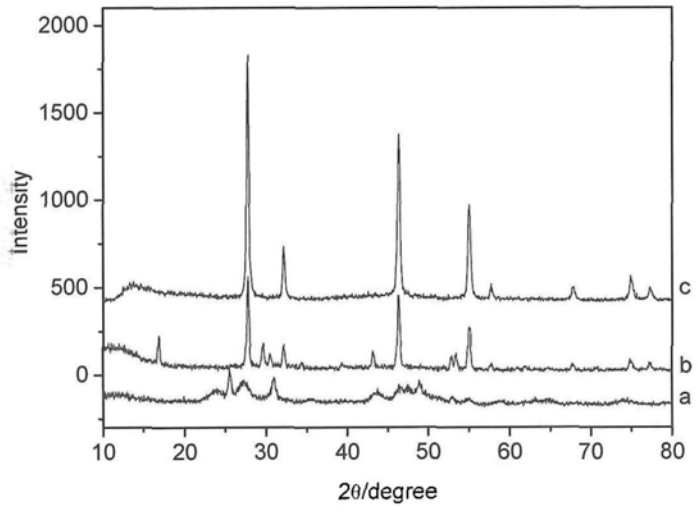

Figure 4.6 XRD patterns of the products obtained at different reaction times (160 °C SDS=10 mM) (a) 0 h (b) 24 h (c) 3 h

N_2 adsorption-desorption isotherm and the corresponding pore size distribution studies provide more information about the porous structure (Figure 4.7). In Figure 4.7a, the pore size distribution indicates most of the pores are in the range from 10 to 40 mm. Figure 4.7b shows a large amount of pores with the size lower than 10 mm. This is really consistent with the results from SEM and TEM measurements.

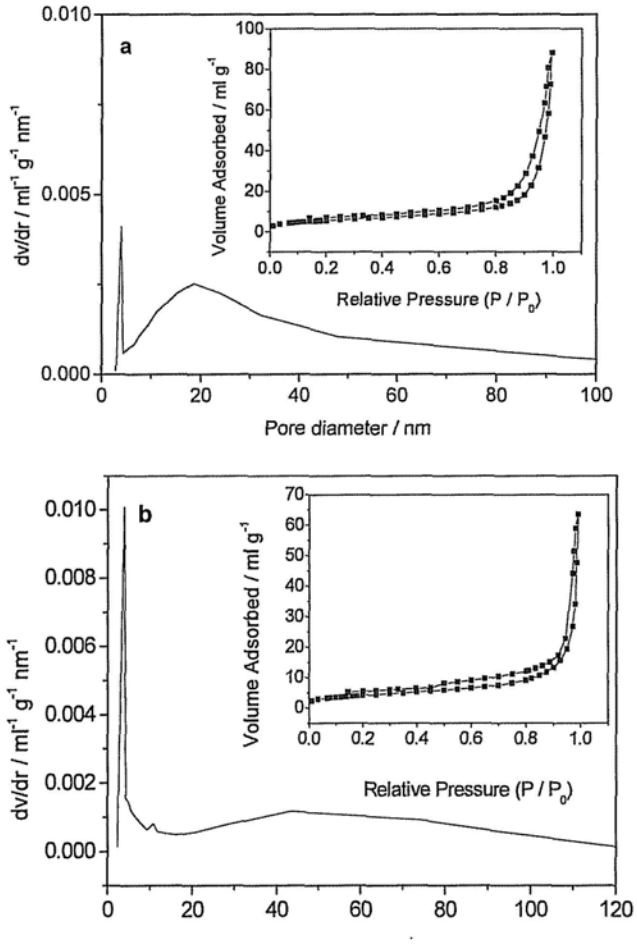

Figure 4.7 N_2 adsorption-desorption isotherm and the corresponding pore size distribution of the product obtained at different SDS concentration: (160 °C, 3h):

(a). 10 mM (b). 50 mM

4.3.2 Proposed Mechanism of Formation

On the basis of the above results, the possible growth mechanism of porous upconversion particles in the presence of SDS might be an oriented self-assembly process (Figure 4.8). Firstly, Y^{3+}, Yb^{3+}, Er^{3+} ions could be chelated by SDS molecules to form the complex. After adding NaF solution, $NaYF_4$:Yb,Er are nucleated and encapsulated with SDS molecules (Figure 4.5a, b). The obtained product is of gel-like structure with low crystallinity (Figure 4.6a). Also due to the efficient encapsulation, higher SDS concentration results in smaller size of the product (XRD calculation). In the subsequent heating process, the primary upconversion nanoparticles serve as the building blocks for the oriented self-assembly into larger particles with single crystalline structure, probably driven by Ostwald ripening.[35, 36] Based on the crystal growth tendency of the cubic phase, the preferred products have a cubic-like morphology when prepared under low SDS concentration. At higher SDS concentrations (SDS could not form micelles because of the high temperature and pressure under hydrothermal conditions), the efficient encapsulation can inhibit further growth of the nanoparticles. Thus they prefer to aggregate into a spherical shape, which is the most stable morphology because of the lowest surface area. The morphology evolution of the product from cubic-like structures to nanospheres caused by different SDS encapsulation efficiency is shown in Figure 4.2. During the oriented assembly process, many pores are generated among these particles due to the

irregular morphologies of the building blocks. It can be imaged that bigger building blocks will result in large pores, and vice versa. So the pore size obtained with bigger primary building blocks at low SDS concentration is larger than that with smaller ones at high concentration. The size distribution obtained from N_2 adsorption-desorption isotherms (Figure 4.7) agrees with the SEM and TEM measurements.

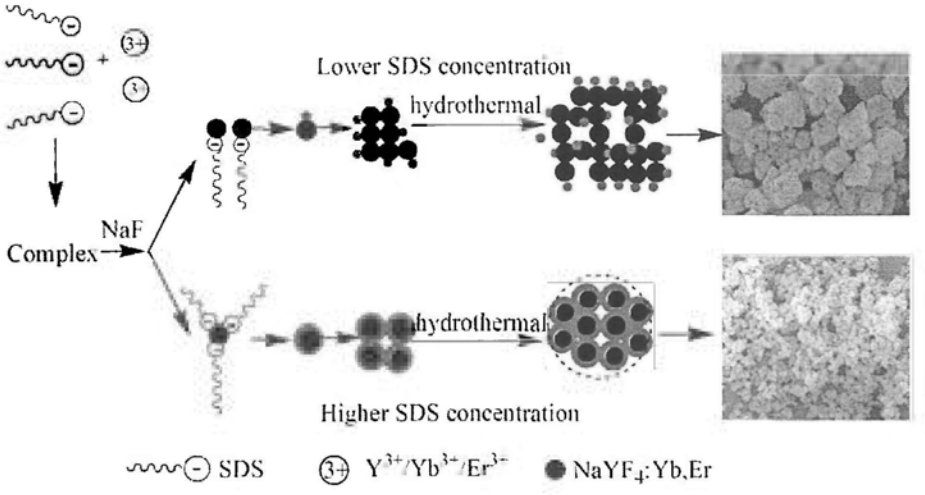

Figure 4.8 Schematic illustration for porous upconversion crystal growth in the presence of SDS

4.3.3 Optical Properties

Figure 4.9a presents the upconversion spectra of the porous $NaYF_4$:Yb,Er particles upon 976 nm NIR excitation. In the spectrum, the green emissions in the range from 510 to 560 nm are assigned to $^2H_{11/2}$, $^4S_{3/2} \rightarrow {}^4I_{15/2}$ transitions. The dominant red emission located between 640 and 700 nm corresponds to $^4F_{9/2} \rightarrow {}^4I_{15/2}$ of Er^{3+}.[11-15] As reported in the literature the intensity of the red emission is much stronger than the green emission.[37] It might be due to the cross-relaxation process between ($4F_{7/2} \rightarrow 4F_{9/2}$) and ($4I_{11/2} \rightarrow 4F_{9/2}$) resonant transitions at high Yb^{3+} concentrations. The luminescence is so strong that it could be clearly observed with naked eyes.

The fluorescence of the cubic phase product is stronger than expected. The main reason is that our product is highly crystalline without surface defects to quench the fluorescence. It is worth noting that the luminescence for the nanospheres obtained at high SDS concentrations is a little weaker than the cubic-like products (Figure 4.9b). It could be due to the smaller particle size.[38]

To understand the upconversion emission mechanism, the dependence of the upconversion luminescence intensity on pump power was investigated. As is well known, the emission intensity I_{uc} is proportional to the excitation intensity I_{IR}:

$I_{uc} \propto I^n_{IR}$,[39] where n is the number of pump photons involved in the upconversion process, which can be determined from the slope of logarithmic plot of the upconversion intensity vs the pump power. Thus the power dependent upconversion spectra were recorded to determine the number of photons responsible for the upconversion process (Figure 4.9c, d). The slopes for the red and green emissions are approximately equal to two, indicating two incident NIR photons are needed for each emitted photon.

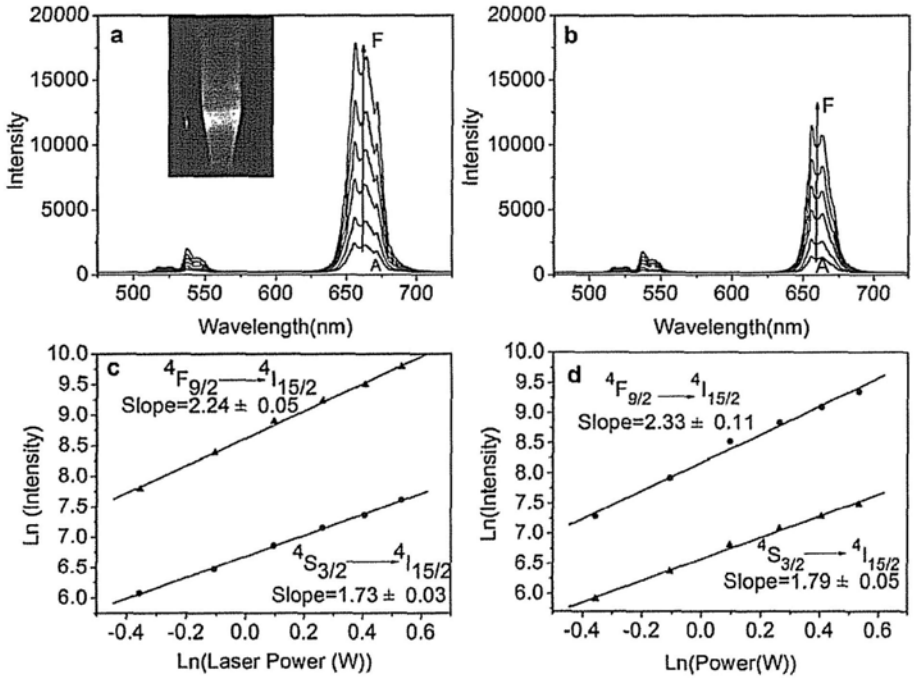

Figure 4.9 Pump power dependent spectra of the products obtained at 160 °C for 3 h (a, c) 10 mM SDS (b, d) 50 mM SDS The power used in Figure a, b is 700, 900, 1100, 1300, 1500 and 1700 mW, repectively, corresponding to curve A-F

4.3.4 Affinity behavior for the porous upconversion crystals to protein molecules

For biological application the used fluorescent nanomaterials must be readily absorbed by some biomolecules, or modified by some biocompatible molecules. Here we have investigated the affinity behavior of the obtained porous upconversion crystals with protein molecules. Here Bovine Serum Albumin (BSA), which has molecular weight of about 67kDa and molecular dimension of 5nm×7nm×7nm,[40] is used as an example.

Figure 4.10a displays FTIR spectra for the porous and nonporous upconversion particles after treatment with BSA. In protein molecules, the characteristic peaks originated from the peptide bonds (-CO-NH-) are amide I (C=O stretching), amide II (-N-H stretching) and amide III (C-N stretching vibration).[41-43] For native BSA the peaks centered at 1656, 1538, 1247cm^{-1} are assigned to amide I, II, III bands, respectively (Figure 4.10a-A). In Figure 4.10a-C, the characteristic peaks of BSA are also very strong, suggesting BSA molecules are absorbed on the porous structure. However, the nonporous structures show very low affinity with BSA according to the weak BSA signals in Figure 4.10a-B.

The quantity of BSA attached to particles is estimated by TGA (shown in Figure 4.10b). For pure upconversion particles the weight loss between room temperature and 450°C is less than 1%, which might be due to the removal of free and bond water in the sample. And the weight loss within 600-800°C might result from the structure changes of upconversion particles. After treatment with BSA the product shows a 8% weight loss in temperature range between 200 and 450°C.[44-46] The larger weight loss might be due to BSA molecules attached in the sample. Thus the amount of BSA attached could be estimated to be about 7%.

After surface modification with some nontoxic materials, such as inorganic layer, polymers, biomolecules, fluorescent materials can be used in biological systems for biosensor, bioimaging, etc. But it is a very common phenomenon that fluorescence was highly decreased or even totally quenched by the encapsulated materials. But in our work the upconversion efficiency is just slightly decreased according to the comparison between the product before and after BSA treatment as shown in Figure 4.10c.

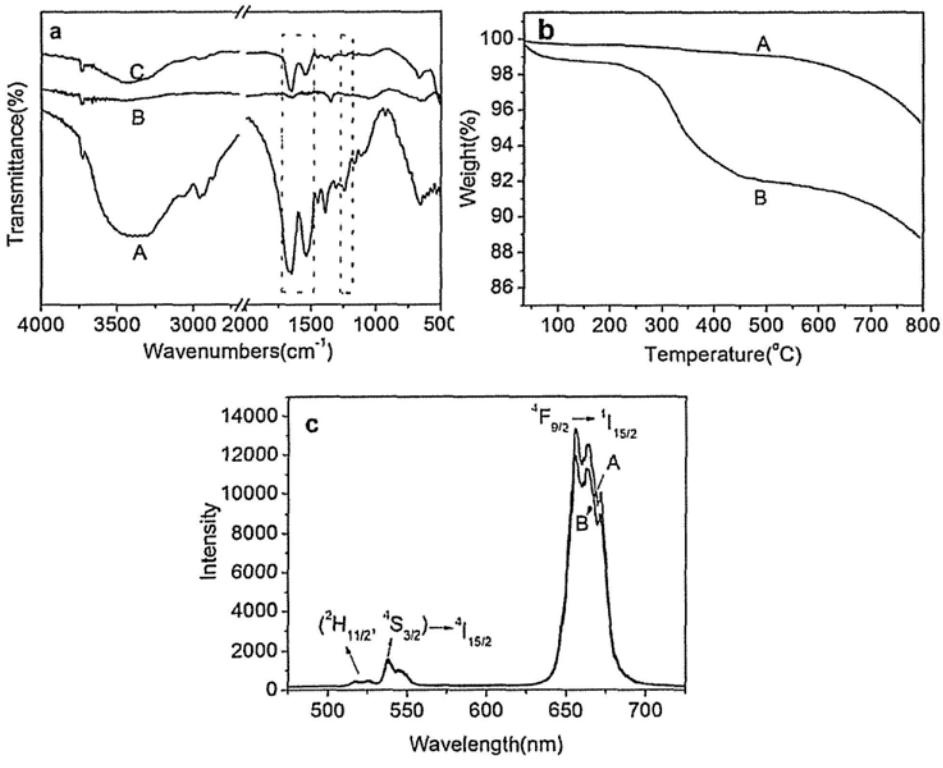

Figure 4.10 Affinity behavior for the porous upconversion crystals to protein molecules (BSA) (a) FTIR measurement A-pure BSA B-nonporous particles (0mM SDS) C-porous particles. (b) TGA and (c) upconversion spectra for the porous particles before (A) and after (B) BSA treatment. The porous products used in all measurements are prepared at 160°C, 3h (SDS 10mM)

4.3.5 Energy transfer from $NaYF_4$:Yb,Er to chlorophylls

The requirement for energy transfer is to make the donor emission band overlap with the absorption band of acceptor.[47, 48] Here $NaYF_4$:Yb,Er is the donor and the chlorophyll extracted from spinach leaves is the acceptor. Their emission and absorption spectra are shown in Figure 4.11. Figure 4.11a presents the upconversion spectrum of the porous $NaYF_4$:Yb,Er particles upon 976 nm NIR excitation. In the spectrum, there is a green emission peak in the range from 510 to 560 nm and a dominant red emission located between 640 and 700 nm.

In the absorption spectrum of the chlorophylls (Figure 4.11b), the band within 640~700nm is attributed to the Q bands of chlorophylls, arising from π-π^* transitions.[28, 29] It is obvious that the red emission peak of upconversion crystals matches perfectly with the red absorption band of chlorophylls. The large spectral overlap indicates the high efficiency of the FRET from the $NaYF_4$:Yb,Er donor to the chlorophylls acceptor.

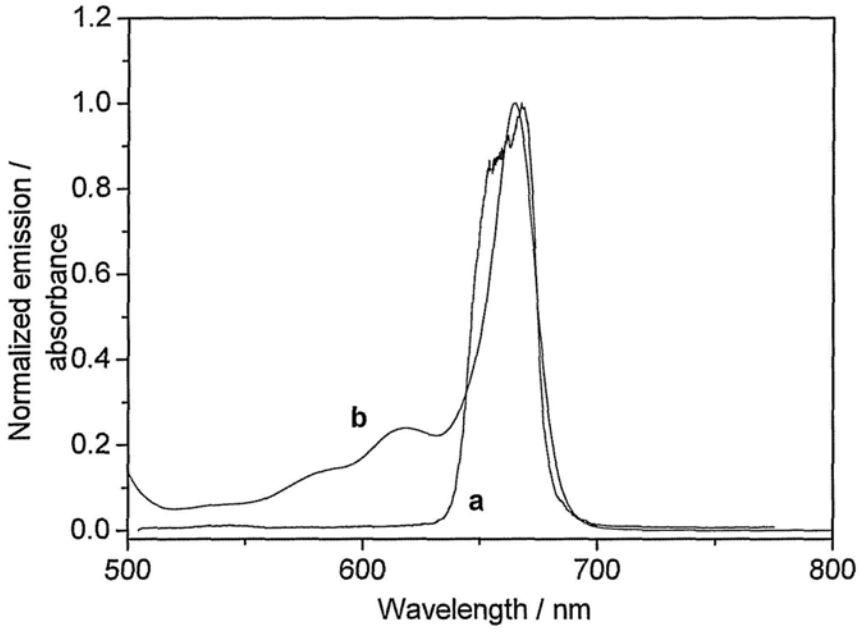

Figure 4.11 (a) Room temperature upconversion emission spectrum of $NaYF_4$:Yb, Er particles in ethanol (5 mg/mL) upon 976 nm NIR excitation and (b) absorption spectrum of chlorophylls.

To examine the FRET process, different amounts of chlorophylls were added into a 1 mL of 5mg/mL $NaYF_4$:Yb,Er ethanol suspension. The corresponding upconversion spectra were recorded upon 976 nm NIR excitation (Figure 4.12a). The red emission intensity decreases with the addition of chlorophylls, indicating that the chlorophylls absorbed the emitted energy by upconversion particles. Interestingly, such FRET from $NaYF_4$:Yb,Er to chlorophylls causes the formation of two new peaks centered at about 685 and 730 nm (See detailed spectra in Figure 4.12b), which are not caused by the pure chlorophylls (Figure 4.12d) and the pure $NaYF_4$:Yb,Er suspension under the NIR excitation. With the addition of

more chlorophylls, the first peak shifts gradually from about 685 nm to 700 nm while the second peak remains at 730 nm. The two peaks come from the fluorescence of chlorophyll molecules according to the literature. The decrease of the two chlorophylls fluorescence peaks with increasing chlorophylls concentration is attributable to the reabsorption (or self-absorption) process, in which the excessive chlorophyll molecules just reabsorb the energy emitted by the neighbouring molecules.[49] Thus the perfect spectral overlap, along with the decrease of the donor emission peak and the presence of acceptor fluorescence peak, demonstrates the FRET process. To further demonstrate the FRET process, chlorophylls with different concentrations were used, as shown in Figure 4.12c. It is clear that with the increase of concentration of chlorophylls, the efficiency of FRET increased.

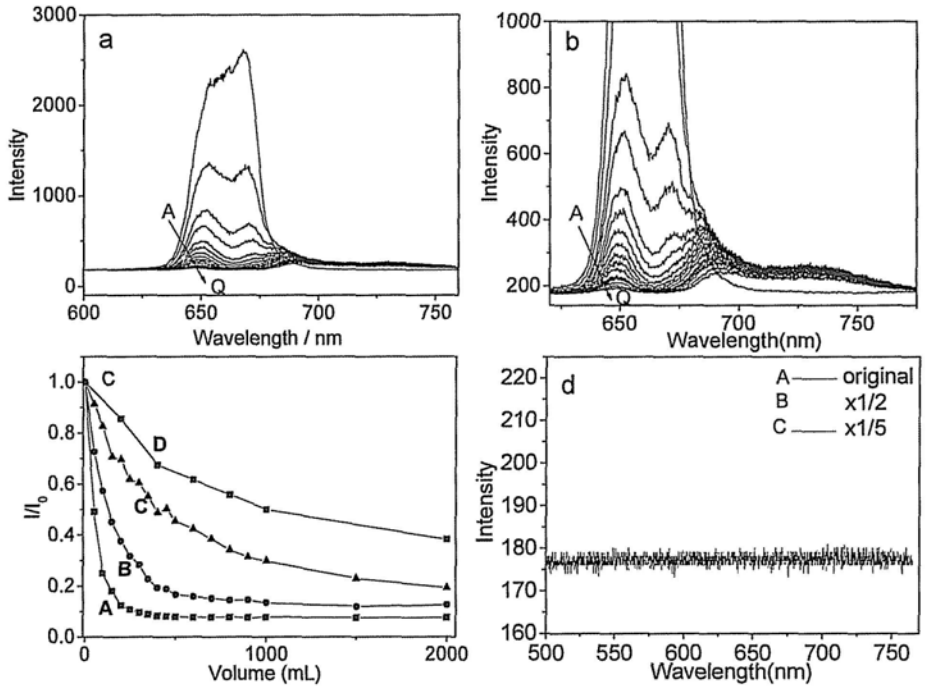

Figure 4.12 (a) Room temperature upconversion fluorescence spectra of the $NaYF_4$:Yb,Er ethanol suspension (1mL, 5mg/mL) with the addition of different volume of original chlorophylls. A-Q: 0, 50, 100, 150, 200, 250, 300, 350, 400, 450, 500, 600, 700, 800, 900, 1000, 2000 μL, respectively. (b) Magnified spectra of Figure 4.12a. (c) The first-order plots for the upconversion emission intensity located at 660 nm and the volume of substance added. A-D: original, ×1/2, ×1/5 chlorophylls and pure ethanol, respectively. I_0 is the intensity at 660nm of the original upconversion suspension. I is the intensity after adding corresponding substance. (d) Room temperature upconversion fluorescent spectra of A) the original chlorophylls solution, B) two-times dilution, C) five-times dilution.

The mechanism of the FRET from upconversion materials to chlorophyll molecules upon NIR excitation is shown in Figure 4.13. Firstly, the absorption of pump photons populates the $^2F_{5/2}$ level in Yb^{3+}. Then energy transfer from the excited Yb^{3+} to Er^{3+} populates the $^4I_{11/2}$ level and then to the $^4F_{7/2}$ level by absorbing the energy of another excited Yb^{3+}, or another 976 nm photon. A part of the $^4I_{11/2}$ excited ions relax nonradiatively to the $^4I_{13/2}$ level. The $^4F_{7/2}$ levels decay nonradiatively to $^2H_{11/2}$, $^4S_{3/2}$ and $^4F_{9/2}$ levels, then fall to the ground state, producing the green emissions centered at 520 nm, 560 nm and the red emission at 660 nm. The $^4F_{9/2}$ level may also be populated from the $^4I_{13/2}$ level of the Er^{3+} ion by the absorption of a 976 nm photon or energy transfer from another Yb^{3+} ion. Here, the $^4F_{9/2}$ level is the predominant excited state in this material as suggested by the strong red emission from the $^4F_{9/2}$-$^4I_{15/2}$ transition (660 nm). For chlorophyll molecules, the Q bands are located at about 663 nm. The chlorophyll molecules possess very strong absorption ability, which facilitates the FRET from the upconversion materials to chlorophyll molecules. The absorbed energy promotes the electrons of chlorophylls from the ground state to the excited states. According to the literature,[50] when the chlorophyll molecules are dissolved in the organic solvents, lower than 10% of the absorbed energy will be emitted by the fluorescence with the rest energy dissipating in the form of heat. So weak chlorophyll fluorescence peaks are observed in the spectra.

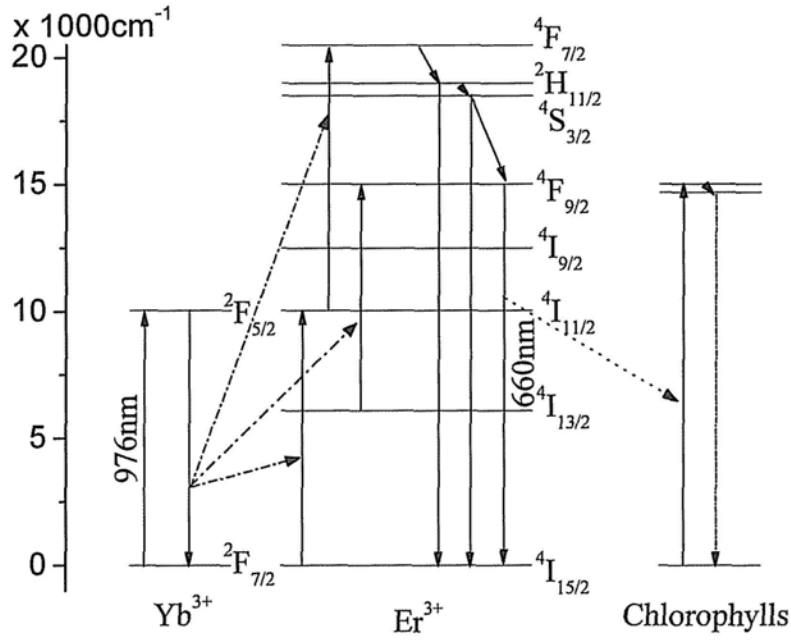

Figure 4.13 Schematic illustration of FRET mechanism from upconversion materials to chlorophylls upon 976 nm NIR irradiation.

4.3.6 Energy transfer from $NaYF_4$:Yb,Er to methylene blue (MB)

Recently a novel approach for photodynamic therapy (PDT) based on FRET from upconversion materials to photosensitizers has been developed.[51] The new method shows great potential to kill the cancer cells located at deep tissues because the NIR light centered at 976 nm, which can penetrate to deeper tissue than the red light used in conventional PDT, is used to activate upconversion particles to trigger the photoreaction. Due to the relatively large surface area porous structure could facilitate the contact between the donors and acceptors to enhance the efficiency of FRET which is a distance-dependent process. Thus the

FRET from the obtained $NaYF_4$:Yb,Er porous particles to photosensitizers has also been investigated.

To realize FRET there must be an appreciable overlap between the emission spectrum of the donor and the absorption spectrum of the acceptor. Here $NaYF_4$:Yb,Er is the donor and MB, an efficient second generation photosensitizer, is the acceptor. As shown in Figure 4.14a, MB shows a strong absorption band within 600-700 nm arising from π-π^* transitions, which possess a large overlap with the emission band of the obtained $NaYF_4$:Yb,Er porous particles, indicating that efficient FRET can occur. To further demonstrate the energy transfer process, different amounts of MB were added into a 1 mL of 5mg/mL $NaYF_4$:Yb,Er ethanol suspension. The corresponding upconversion spectra were recorded upon 976 nm NIR irradiation excitation (Figure 4.14b, c). It is obvious that the red emission intensity decrease with the increase of MB added, further indicating the FRET from $NaYF_4$:Yb,Er to MB.

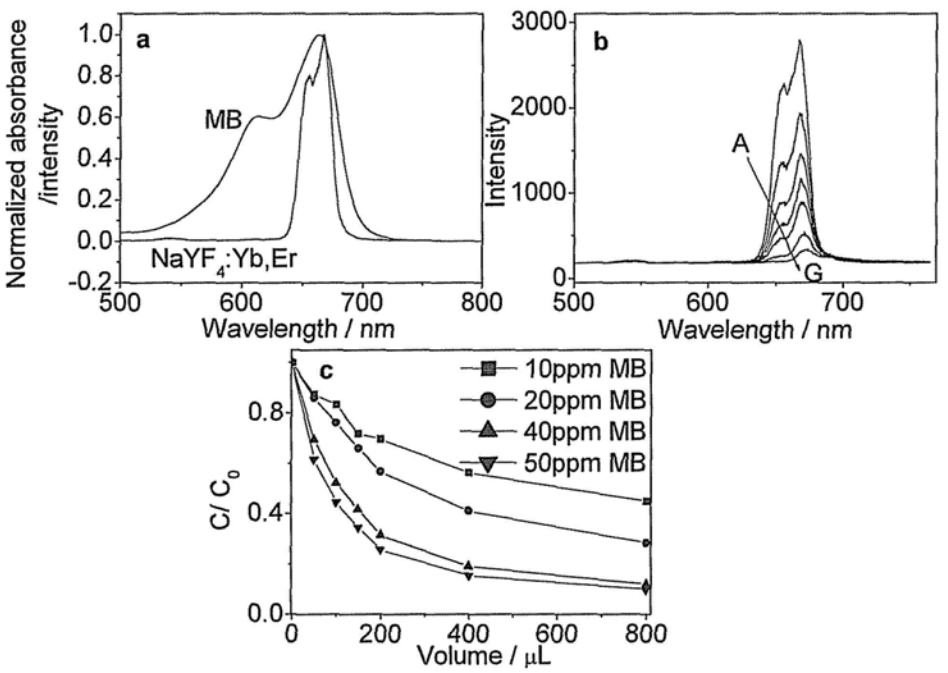

Figure 4.14 (a) Room temperature upconversion emission spectrum of $NaYF_4$:Yb, Er particles in ethanol (5 mg/mL) upon 976 nm NIR excitation and absorption spectrum of MB (40ppm). (b) Room temperature upconversion fluorescence spectra of the $NaYF_4$:Yb,Er ethanol suspension (1mL, 5mg/mL) with the addition of different volume of MB (40ppm). A-G: 0, 50, 100, 150, 200, 400, 800 μL, respectively. (c) The first-order plots for the upconversion emission intensity located at 660 nm and the volume of MB added.

4.4 Conclusions

In conclusion, a facile method has been developed to prepare porous $NaYF_4$:Yb,Er upconversion single crystals with strong red emission peaks upon NIR excitation. SDS plays an important in controlling the crystalline phase,

morphology and pore size of the obtained products. The porous structure facilitates the contact between upconversion particles and chlorophylls, resulting in the highly efficient FRET. This study suggests a possibility to realize NIR-driven photosynthesis to increase photosynthesis efficiency and deal with the growing global energy issue.

4.5 References

[1] Auzel, F. *Chem. Rev.*, **2004**, *104*, 139.

[2] Wang, F.; Liu, X. G. *Chem. Soc. Rev.*, **2009**, *38*, 976.

[3] Qian, H. S.; Zhang, Y. *Langmuir*, **2008**, *24*, 12123.

[4] Suyver, J. F.; Aebischer, A.; Biner, D.; Gerner, P.; Grimm, J.; Heer, S.; Kramer, K. W.; Reinhard, C.; Gudel, H. U. *Opt. Mater.*, **2005**, *27*, 1111.

[5] Rumbles, G. *Nature*, **2001**, *409*, 572.

[6] Chivian, J. S.; Case, W. E.; Eden, D. D. *Appl. Phys. Lett.*, **1979**, *35*, 124.

[7] Downing, E.; Hesselink, L.; Ralston, J.; Macfarlane, R. *Science*, **1996**, *273*, 1185.

[8] van de Rijke, F.; Zijlmans, H.; Li, S.; Vail, T.; Raap, A. K.; Niedbala, R. S.; Tanke, H. J. *Nat. Biotechnol.*, **2001**, *19*, 273.

[9] Xiong, L. Q.; Chen, Z. G.; Yu, M. X.; Li, F. Y.; Liu, C.; Huang, C. H. *Biomaterials*, **2009**, *30*, 5592.

[10] Kramer, K. W.; Biner, D.; Frei, G.; Gudel, H. U.; Hehlen, M. P.; Luthi, S. R. *Chem. Mater.*, **2004**, *16*, 1244.

[11] Bednarkiewicz, A.; Nyk, M.; Samoc, M.; Strek, W. *J. Phys. Chem. C*, **2010**, *114*, 17535.

[12] Chen, G. Y.; Ohulchanskyy, T. Y.; Kumar, R.; Agren, H.; Prasad, P. N. *ACS Nano*, **2010**, *4*, 3163.

[13] Niu, W. B.; Wu, S. L.; Zhang, S. F.; Li, L. *Chem. Commun.*, **2010**, *46*, 3908.

[14] Shan, J. N.; Uddi, M.; Yao, N.; Ju, Y. G. *Adv. Funct. Mater.*, **2010**, *20*, 3530.

[15] Zhang, H.; Li, Y. J.; Lin, Y. C.; Huang, Y.; Duan, X. F. *Nanoscale*, **2011**, *3*, 963.

[16] Chen, J.; Guo, C. R.; Wang, M.; Huang, L.; Wang, L. P.; Mi, C. C.; Li, J.; Fang, X. X.; Mao, C. B.; Xu, S. K. *J. Mater. Chem.*, **2011**, *21*, 2632.

[17] Guo, H.; Li, Z. Q.; Qian, H. S.; Hu, Y.; Muhammad, I. N. *Nanotechnology*, **2010**, *21*.

[18] Mi, C. C.; Zhang, J. P.; Gao, H. Y.; Wu, X. L.; Wang, M.; Wu, Y. F.; Di, Y. Q.; Xu, Z. R.; Mao, C. B.; Xu, S. K. *Nanoscale*, **2010**, *2*, 1141.

[19] Wang, M.; Mi, C. C.; Wang, W. X.; Liu, C. H.; Wu, Y. F.; Xu, Z. R.; Mao, C. B.; Xu, S. K. *ACS Nano*, **2009**, *3*, 1580.

[20] Li, Z. Q.; Zhang, Y. *Angew. Chem. Int. Ed.*, **2006**, *45*, 7732.

[21] Schafer, H.; Ptacek, P.; Zerzouf, O.; Haase, M. *Adv. Funct. Mater.*, **2008**, *18*, 2913.

[22] Sivakumar, S.; Diamente, P. R.; van Veggel, F. C. *Chem. Eur. J.*, **2006**, *12*, 5878.

[23] Li, Z. Q.; Zhang, Y.; Jiang, S. *Adv. Mater.*, **2008**, *20*, 4765.

[24] Wang, L. Y.; Yan, R. X.; Hao, Z. Y.; Wang, L.; Zeng, J. H.; Bao, H.; Wang, X.; Peng, Q.; Li, Y. D. *Angew. Chem. Int. Ed.*, **2005**, *44*, 6054.

[25] Wang, L. Y.; Li, Y. D. *Chem. Commun.*, **2006**, 2557.

[26] Qu, X. S.; Song, H. W.; Bai, X.; Pan, G. H.; Dong, B.; Zhao, H. F.; Wang, F.; Qin, R. F. *Inorg. Chem.*, **2008**, *47*, 9654.

[27] Zhang, F.; Wan, Y.; Shi, Y. F.; Tu, B.; Zhao, D. Y. *Chem. Mater.*, **2008**, *20*, 3778.

[28] Miyamoto, K. *Renewable biological systems for alternative sustainable energy production* Food and Agriculture Organization of the United Nations. Rome, 1997 pp. 1.

[29] Scheer, H. *Chlorophylls and Bacteriochlorophylls: Biochemistry, Biophysics, Functions and Applications*, Springer. Dordrecht, 2006 pp. 7.

[30] Demers, D. A.; Dorais, M.; Wien, C. H.; Gosselin, A. *Sci. Hortic.*, **1998**, *74*, 295.

[31] Grimstad, S. O. *Sci. Hortic.*, **1987**, *32*, 297.

[32] Liang, X.; Wang, X.; Zhuang, J.; Peng, Q.; Li, Y. D. *Adv. Funct. Mater.*, **2007**, *17*, 2757.

[33] Yi, G. S.; Chow, G. M. *Adv. Funct. Mater.*, **2006**, *16*, 2324.

[34] Zhuang, J. L.; Wang, J.; Yang, X. F.; Williams, I. D.; Zhang, W.; Zhang, Q. Y.; Feng, Z. M.; Yang, Z. M.; Liang, C. L.; Wu, M. M.; Su, Q. *Chem. Mater.*, **2009**, *21*, 160.

[35] Hu, X. L.; Yu, J. C. *Adv. Funct. Mater.*, **2008**, *18*, 880.

[36] Zhu, Y. F.; Zhao, W. R.; Chen, H. R.; Shi, J. L. *J. Phys. Chem. C*, **2007**, *111*, 5281.

[37] Sun, Y. J.; Chen, Y.; Tian, L. J.; Yu, Y.; Kong, X. G.; Zhao, J. W.; Zhang, H. *Nanotechnology*, **2007**, *18*.

[38] Chen, G. Y.; Somesfalean, G.; Zhang, Z. G.; Sun, Q.; Wang, E. P. *Opt. Lett.*, **2007**, *32*, 87.

[39] Lezhnina, M. M.; Justel, T.; Katker, H.; Wiechert, D. U.; Kynast, U. H. *Adv. Funct. Mater.*, **2006**, *16*, 935.

[40] Hong, Y. L.; Fan, H. S.; Zhang, X. D. *J. Phys. Chem. B*, **2009**, *113*, 5837.

[41] Falini, G.; Foresti, E.; Lesci, I. G.; Lunelli, B.; Sabatino, P.; Roveri, N. *Chem. Eur. J.*, **2006**, *12*, 1968.

[42] Li, D.; Teoh, W. Y.; Selomulya, C.; Woodward, R. C.; Amal, R.; Rosche, B. *Chem. Mater.*, **2006**, *18*, 6403.

[43] Li, S. K.; Shen, Y. H.; Xie, A. J.; Yu, X. R.; Qiu, L. G.; Zhang, L.; Zhang, Q. F. *Green Chemistry*, **2007**, *9*, 852.

[44] Abdelmoez, W.; Yoshida, H. *Macromolecules*, **2007**, *40*, 9371.

[45] Lin, J. J.; Wei, J. C.; Tsai, W. C. *J. Phys. Chem. B*, **2007**, *111*, 10275.

[46] Xie, J. P.; Zheng, Y. G.; Ying, J. Y. *J. Am. Chem. Soc.*, **2009**, *131*, 888.

[47] Chi, C. W.; Lao, Y. H.; Li, Y. S.; Chen, L. C. *Biosens. Bioelectron.*, **2011**, *26*, 3346.

[48] Gopich, I. V.; Szabo, A. *J. Phys. Chem. B*, **2011**, *114*, 15221.

[49] Zandomeneghi, M.; Carbonaro, L.; Caffarata, C. *J. Agric. Food. Chem.*, **2005**, *53*, 759.

[50] Livingston, R.; Watson, W. F.; Mcardle, J. *J. Am. Chem. Soc.*, **1949**, *71*, 1542.

[51] Qian, H. S.; Guo, H. C.; Ho, P. C. L.; Mahendran, R.; Zhang, Y. *Small*, **2009**, *5*, 2285.

Chapter Five

$NaYF_4$:Yb,Tm/CdS Composite as a Novel Near-Infrared-Driven Photocatalyst

5.1 Introduction

Photocatalysis is an environmentally friendly technique to eliminate toxic organic substances in air and water. The process is initiated by the irradiation of semiconductor materials with a suitable light source. The subsequently formed free radicals with strong oxidizing ability could mineralize organic pollutants to CO_2 and H_2O[1]. Photocatalysis has attracted much attention in recent years because it allows the utilization of clean, safe, and renewable solar energy to solve environmental problems.

Fujishima and Honda discovered the photocatalytic splitting of water on titanium dioxide (TiO_2) photoanodes under ultraviolet (UV) light in 1972[2]. Since then TiO_2 has been widely studied as an efficient photocatalyst for its appropriate electronic band structure, biological and chemical inertness, strong oxidizing power and long-term stability[3]. However, this photocatalyst has a relatively large band gap that requires UV light for activation. Much effort has been focused on improving the photocatalytic efficiency by understanding the effects of particle size, morphology, crystal structure, surface area on the reaction mechanism[4-8].

Various approaches have been developed to extend the response of photocatalysts into the visible light region. These include doping metallic (Pt[9], Fe[10], Ag[11], Cr[12]) and nonmetallic (C[13], N[14], F[15], S[16]) elements in conventional photocatalysts to decrease the band gap to accommodate the visible light photon energy, and the use of some low band gap semiconductors including CdS[17, 18], WO_3[19, 20], $BiVO_4$[21], Bi_2WO_6[22], and polymeric semiconductors[23]. Another promising system is the coupled semiconductor such as TiO_2/CdS[24, 25], in which CdS absorbs visible light and transfers the photoexcited electrons to TiO_2 to induce photoreactions.

Near infrared (NIR) photocatalysis involving YF_3: Yb,Tm/TiO_2 core/shell nanoparticles has been reported recently[26]. The upconversion YF_3: Yb,Tm particles absorb NIR light and emit a very weak UV light which excites TiO_2 for photocatalysis. NIR to UV conversion is obviously a difficult process, and it would be much easier to convert NIR to visible-light[27-31]. It is widely accepted that the hexagonal phase of $NaYF_4$ is a better host material for up-converting NIR to visible light than the nonlinear crystals[27-32]. For example, the efficiency for $NaYF_4$:Yb,Tm is $3.4*10^{-2}cm^2/W$ while that for potassium dihydrogen phosphate (KDP) is only in the order of 10^{-11} [32]. To take advantage of the much stronger visible-light emission, it would be a good idea to replace TiO_2 with a narrower bandgap CdS.

Herein, we describe an efficient approach to construct a novel near infrared photocatalyst by combining a low energy band gap semiconductor CdS with an upconversion material $NaYF_4$: Yb,Tm. Particles of CdS and $NaYF_4$:Yb, Tm are pretreated with thioglycolic acid and mercaptoethanol. The reaction between these two organic molecules causes the formation of $NaYF_4$: Yb,Tm/CdS composite. Results from scanning electron microscopy (SEM), transmission electron microscopy (TEM), energy-dispersive X-ray spectroscopy (EDX) and powder X-ray diffraction (XRD) measurements demonstrate that CdS nanoparticles are uniformly assembled on the surface of $NaYF_4$: Yb,Tm microrods. Energy transfer from $NaYF_4$: Yb,Tm to CdS is confirmed by the upconversion and fluorescence decay properties. Hydroxyl radicals are generated upon NIR irradiation on the composite material. The NIR photocatalytic activity of the $NaYF_4$: Yb,Tm/CdS composite is investigated by degrading Rhodamine B and methylene blue. A mechanism for NIR-driven photocatalysis is proposed.

5.2 Experimental Section

5.2.1 Chemicals

All the chemicals were used as received without further purification.

5.2.2 Synthesis of mercaptoethanol functionalized upconversion microrods

Pure $NaYF_4$: Yb,Tm microrods were synthesized via an ethylenediamine tetraacetic acid disodium salt (EDTA) assisted-hydrothermal method[33]. The molar ratio of lanthanide ions in the product, Y/ Yb /Tm, is 79.5:20:0.5. Then 400 mg of the prepared $NaYF_4$: Yb,Tm microcrystals were dispersed in 20ml deionized water containing 0.2 mL mercaptoethanol. After stirring for 3h, the product was separated and washed.

5.2.3 Synthesis of thioglycolic acid functionalized CdS nanoparticles

Pure CdS nanoparticles are prepared by a hydrothermal reaction[34]. Then 70 mg of CdS nanoparticles were treated with 10 ml deionized water containing 0.1 mL thioglycolic acid, stirred for 3h, then centrifuged and washed.

5.2.4 Preparation of $NaYF_4$: Yb,Tm/CdS composite

The $NaYF_4$: Yb,Tm and CdS precursors were mixed in 20ml deionized water, then heated to 160°C for 3h. Then the yellow precipitates of $NaYF_4$: Yb,Tm/CdS were collected from the suspension by centrifugation (2000 rpm, 5 min) and washed with deionized water for several times. For comparison pure $NaYF_4$:

Yb,Tm and CdS precursors which were not modified were mixed together, then treated the same conditions as described above.

5.2.5 Detection of photogenerated OH radicals

Terephthalic acid ($4*10^{-4}$ M) was dissolved in NaOH ($2*10^{-3}$ M) solution. In a typical process, 20 mg $NaYF_4$: Yb,Tm/CdS mixed with 10 mL of terephthalic acid solution. Then the mixture was irradiated with a NIR laser (λ=976nm). At every 30 min, 1.2 mL of the suspensions were collected, then centrifuged. Then 1ml of the solution was diluted four times for the PL measurement. The hydroxyterephthalate anion formed was monitored by fluorescence analysis with a excitation wavelength of 320 nm. In the control experiments, pure CdS and $NaYF_4$: Yb,Tm were analyzed under identical conditions.

5.2.6 Photocatalytic activity measurements

The photocatalytic activities of the $NaYF_4$: Yb,Tm/CdS were measured by the degradation of Rhodamine B in an aqueous solution. 20 mg of photocatalyst was suspended in a 10 ml aqueous solution of Rhodamine B (10ppm). Prior to irradiation, the suspension was stirred in the dark for 24 hours to establish an adsorption/desorption equilibrium between the photocatalyst and Rhodamine B. Then the mixture was first irradiated with a NIR laser (λ=976nm, power=2W, beam diameter=1cm) for different hours. At 30 min intervals, 0.6 mL of the

suspensions were collected, then centrifuged. Then 0.5 ml of the solution was diluted eight times for the following measurement. The concentration of Rhodamine B was measured by a UV-Visible spectrophotometer and the absorption peak at 550nm was monitored. The photocatalytic activity has also been demonstrated by using methylene blue as degradation probe. And the conditions are same as the degradation of Rhodamine B. Visible light photocatalytic activity was done by dispersing 40 mg photocatalyst into 20ml of aqueous solution containing 50 ppm Rhodamine B. The light source is a commercial 300W tungsten halogen spotlight surrounded with a filter that restricted the illumination to the 400-660 nm range.

5.2.7 Measurement of cadmium concentrations by ICP-AES:

Standard cadmium solutions: Four standard solutions were prepared. The concentrations of Cd^{2+} were 0.5, 1, 2, and 4mg/L. Pure DI water was used as blank.

Sample solutions: Two identical slurry solutions were prepared by suspending 20 mg of the composite photocatalyst in 10 ml of 10 ppm Rhodamine B. The solutions were stirred in the dark for 24 hours to establish an adsorption/desorption equilibrium between the photocatalyst and Rhodamine B. One solution was exposed to NIR irradiation for 3 hr while the other was not.

Then the suspensions were centrifuged at 2000 rpm. The supernatants were collected for ICP-AES measurements.

5.2.8 Characterization:

The general morphology of the products was characterized by a field-emission scanning electron microscope (FESEM, FEI, Quanta 400 FEG) equipped with an energy-dispersive spectroscopy instrument. TEM, HRTEM and EDX line scan profiles were carried out on a Tecnai F20 microscope (FEI, 200 kV) coupled with an energy-dispersive X-ray (EDX) spectrometer. X-ray diffraction (XRD) patterns were recorded using a Bruker D8 Advance diffractometer with high-intensity Cu $K\alpha_1$ irradiation (λ=1.5406 Å). Room temperature upconversion fluorescence spectra were recorded on a Hitachi F-4500 fluorescence spectrophotometer equipped with a commercial 976 nm IR laser with tunable power. In lifetime measurements, a 980nm laser line from Optical Parametric Oscillator (OPO) (Opotek MagicPRISM) was used for excitation, which was pumped by the third harmonics, 355nm line of a Nd:YAG laser (Quantel Brilliant B). The pulse-width of laser was 4ns and the photo-detector was using a thermoelectrically cooled GaAs photomultiplier tube (PMT) (Hamamatsu R636-10) with 3ns response time. A 600MHz oscilloscope (Agilent Infiniium 54830B) was used to record the decay-time spectrum by using an average of 512 times. A 10X amplifier was used

to record the signal from the $NaYF_4$:Yb,Tm/CdS composite. UV-vis spectra were recorded on a Varian Cary 500 Scan UV-visible system.

5.3 Results and Discussion

Figure 5.1 shows the synthesis process for the NIR photocatalyst. CdS, a well-known low band gap semiconductor (about 2.5 eV)[35, 36], is coupled to the hexagonal phase (β-phase) of $NaYF_4$: Yb,Tm microcrystals. The large microcrystals are known to have much higher upconversion efficiency than its nano-counterparters[37]. CdS nanoparticles are pretreated with thioglycolic acid molecules ($SHCH_2COOH$). The SH groups are for self stabilization, and the COOH groups functionalize the surface. The surfaces of (β-phase) $NaYF_4$: Yb,Tm microcrystals are activated by the treatment with mercaptoethanol molecules ($SHCH_2CH_2OH$). The strong interaction between the –SH groups and lanthanide ions would leave many OH groups on the surface of the microcrystals. The subsequent reaction between mercaptoethanol and thioglycolic acid forms a stable $NaYF_4$: Yb,Tm/CdS composite.

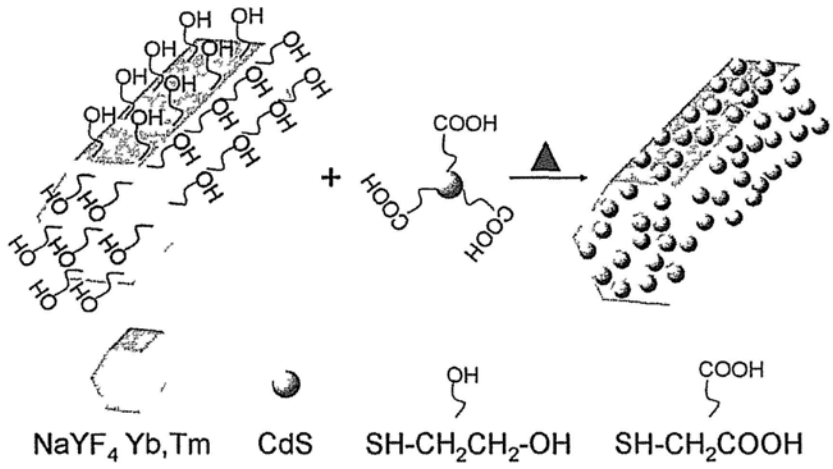

▲ ~SCH_2CH_2-OH + HOOC-CH_2S~ ⟶ ~SCH_2CH_2-OOC-CH_2S~

Figure 5.1 Strategy for the preparation of $NaYF_4$: Yb,Tm/CdS composite.

5.3.1 Morphology investigations

The size and morphology of the resulting materials were examined by SEM and TEM. Figure 5.2a displays a representative SEM image of the pure $NaYF_4$: Yb,Tm microcrystals. The microrod crystals are of a length roughly equal to 6μm and diameter of 1μm. As shown in the magnified SEM image (Figure 5.2b) and the TEM image (Figure 5.2c), the surfaces of the microrods are rather smooth. However, the surfaces become rougher after the deposition of CdS (Figure 5.2d). Figures 5.2e and f present the enlarged views of the single microrods. Clearly, CdS nanoparticles of 50 to 80 nm are uniformly assembled on the surface of the $NaYF_4$: Yb,Tm microrods. In the TEM images (Figure 5.2g), the apparent microscopy contrast further confirms the presence of CdS nanoparticles on the surface of $NaYF_4$: Yb,Tm microrods. High-resolution TEM images (Figure 5.2h, i)

provide further insight into the microstructure of the coated nanoparticles. The clear lattice fringes indicate high crystallinity and the measured lattice spacings match very well with the planes of hexagonal phase CdS (JCPDS no. 75-1545). As seen from Figure 5.2j and k, the color of pure $NaYF_4$: Yb,Tm is white, while the composite becomes yellow.

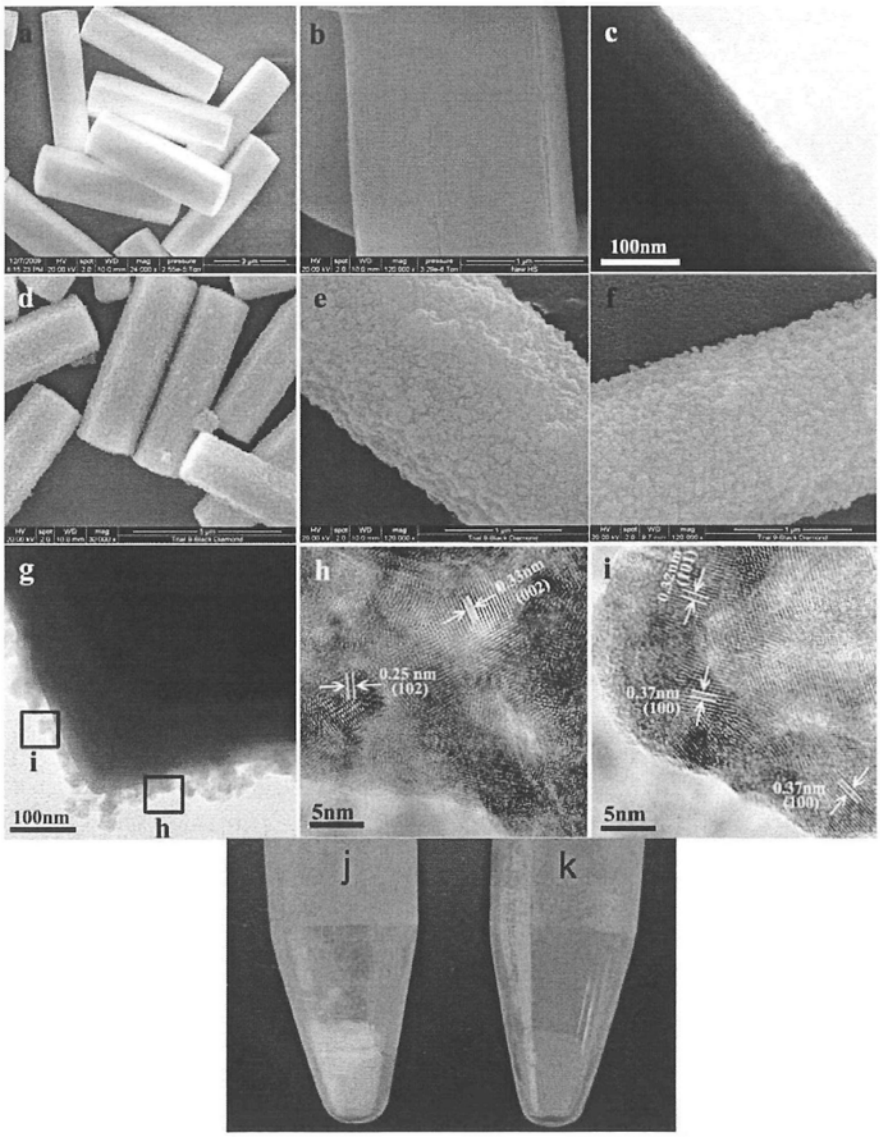

Figure 5.2 SEM (a, b, d, e, f), TEM (c, g, h, i) images and pictures (j, k) of the products. (a-c): pure $NaYF_4$: Yb,Tm (d-i): $NaYF_4$: Yb,Tm/CdS composite. Figure h and i are the corresponding high-resolution TEM images from the areas outlined by the rectangles marked in (g). Pictures show the colors of (j) pure $NaYF_4$: Yb,Tm and (k) $NaYF_4$: Yb,Tm/CdS

To find out whether CdS could be coupled to $NaYF_4$ by physical adsorption, control experiments were carried out in the absence of chemical modifiers. As shown in Figure 5.3, CdS does not adsorb well onto $NaYF_4$ without surface functionalization. The strong coupling between CdS and $NaYF_4$ is probably due to the formation of chemical bonds between thioglycolic acid and mercaptoethanol.

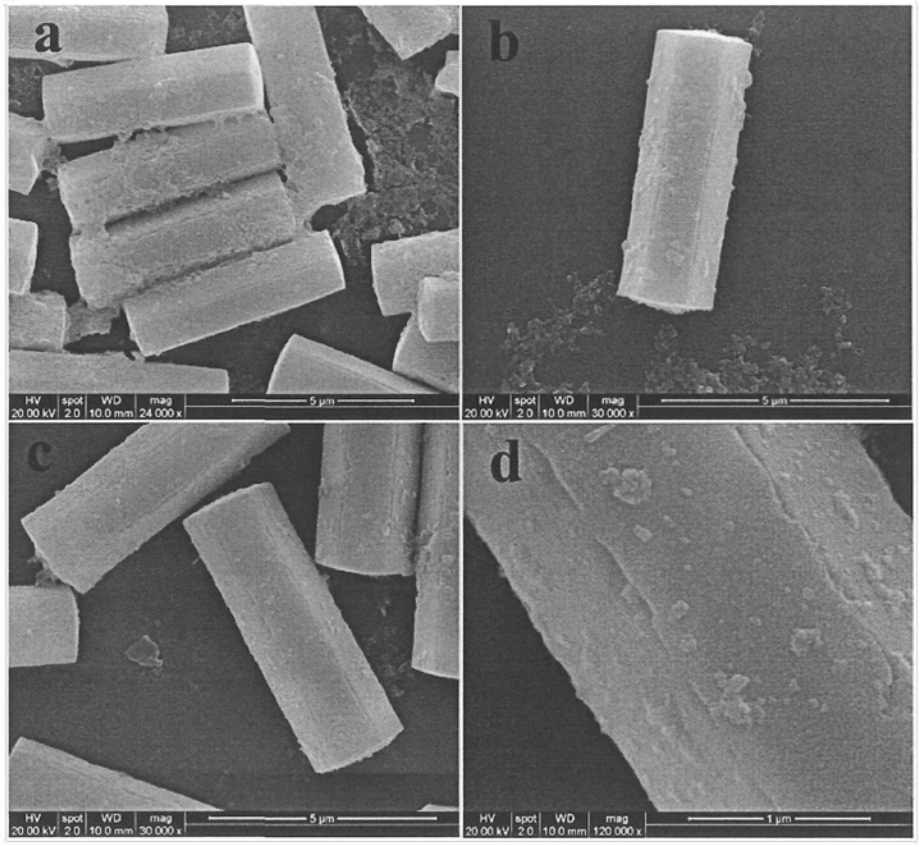

Figure 5.3 SEM images of the products obtained from control experiments without surface modification

5.3.2 Composition Studies

EDX elemental line scanning was performed to further determine the composition of composite, especially the particles on the surface. Figure 5.4a shows the line scan profiles, recorded along the black line presented in Figure 5.4b. The scanning starts from point A, where both the signal from $NaYF_4$: Yb,Tm and CdS are detected. The atomic ratio of Y/Cd is 17:0.4. It can be clearly seen from Figure 5.4a that with the scanning going outside, the signal of Y drops, while Cd and S increase. At the interface (point B), Y/Cd decreases to 22:10. Following point B is a sharp decrease for Y. But Cd and S gradually grow to the maximum value at point C, where Y/Cd is 2:28. This a clear evidence for the strong coupling of CdS nanoparticles on the $NaYF_4$: Yb,Tm microcrystals.

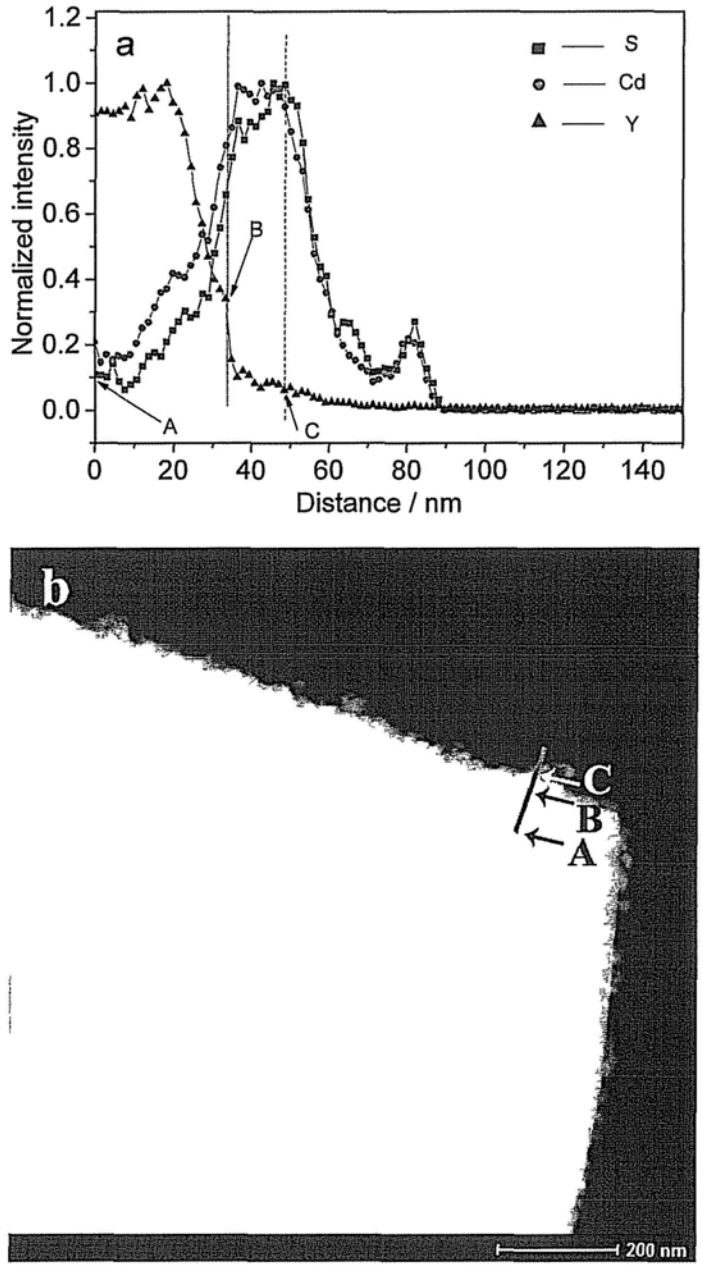

Figure 5.4 EDX line scan profiles (a) and TEM (b) image of the $NaYF_4$: Yb,Tm/CdS composite. Points A, B and C in (a) are corresponding to the same points shown in (b). In Figure (a), Y, Cd, and S data are plotted as blue triangles, red dots, and black rectangles, respectively.

A typical XRD pattern provides further crystallinity and phase information for the composite. As shown in Figure 5.5, in addition to the reflections of hexagonal phase $NaYF_4$ (JCPDS no. 28-1192), several weak peaks of hexagonal phase CdS (JCPDS no. 75-1545) are observed at 26.5°, 28.1°, 36.4° and 48.1°.

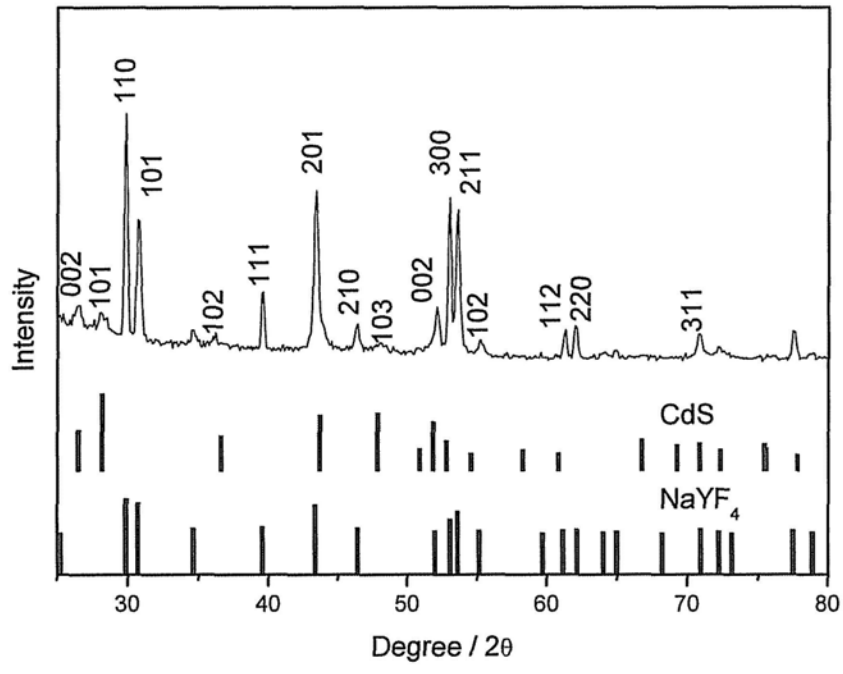

Figure 5.5 XRD pattern of the prepared $NaYF_4$: Yb,Tm/ CdS composite

5.3.3 Optical properties

NIR photocatalysis depends on the energy transfer from $NaYF_4$: Yb,Tm to CdS. The requirement for an efficient energy transfer is to make the donor emission band overlap with the absorption band of acceptor[38, 39]. Here $NaYF_4$: Yb,Tm is the donor and CdS is the acceptor. The upconversion fluorescence spectrum of $NaYF_4$: Yb,Tm and the absorption spectrum of CdS are presented in Figure 5.6a. $NaYF_4$: Yb,Tm could absorb NIR photons because the Yb^{3+} ion has a large absorption cross section from 970 to 1000 nm[40, 41]. After absorbing two or more NIR photons, $NaYF_4$: Yb,Tm emits visible and UV light. As shown in Figure 5.6a-A, five emission peaks appear upon NIR irradiation. The predominate blue emission peaks at 450 and 476 nm are assigned to the $^1D_2 \rightarrow {}^3F_4$, $^1G_4 \rightarrow {}^3H_6$ transitions of Tm^{3+}[42-46]. The two UV emissions at 350 and 361 nm are due to the $^3P_0 \rightarrow {}^3F_4$ and $^1D_2 \rightarrow {}^3H_6$ transitions, respectively[42-46]. The weakest red emission at 645nm is from the $^1G_4 \rightarrow {}^3F_4$ transition[42-46]. As a semiconductor with low energy gap, CdS exhibits a broad absorption band from 200 to 550 nm. It is very clear that the absorption band of CdS overlaps very well with the blue emission peak of upconversion particles. The large spectral overlap indicates that the upconversion blue emission can be strongly quenched by energy transfer.

To examine the energy transfer process, the upconversion emission spectra of the upconversion/CdS composite were recorded upon 976 nm NIR excitation (Figure 5.6b). The intensity of UV and blue emission peaks are greatly reduced

after the combination of CdS, indicating significant energy transfer. However, it can be clearly observed from Figure 5.6c that due to the small overlap with the absorption spectrum of CdS, the red emission peak of $NaYF_4$: Yb,Tm only decreases slightly. The fluorescence intensity ratio of I_{blue}/I_{red} for the composite is 11.9, which is much smaller than the value of 41.3 for the pure $NaYF_4$: Yb,Tm. Since the two spectra were recorded under identical conditions and the Tm content was the same, the decrease in I_{blue}/I_{red} strongly suggests an energy transfer from $NaYF_4$: Yb,Tm to CdS.

A comparison between the lifetimes of the donor alone and the donor-acceptor pairs could provide direct evidence on the energy transfer. The life time of the emission at 476nm for $NaYF_4$:Yb,Tm and $NaYF_4$:Yb,Tm/CdS were recorded (Figure 5.6d). As the addition of CdS quenched the 476 nm emission, a 10X amplifier was used when measuring the $NaYF_4$:Yb,Tm/CdS sample. This caused a shorter rising time (about 0.4ms, Curve B) than the pure $NaYF_4$:Yb,Tm (about 0.7ms, Curve A). It should be noted that the signal amplification only affects the rise up time but has no effect on the decay time measurements. The decay profiles are fit with monoexponential model. The average decay times are 788, and 359μs for the pure $NaYF_4$: Yb,Tm and $NaYF_4$: Yb,Tm/CdS, respectively. The decrease in lifetime further confirms the energy transfer. The efficiency of energy transfer can be calculated from the following equation[47]:

$$E=1-\tau_{DA}/\tau_{D}$$

where τ_{DA} and τ_D are the lifetime of $NaYF_4$: Yb,Tm with and without CdS, respectively. The observed energy transfer efficiency of the blue emissions is 54.4%.

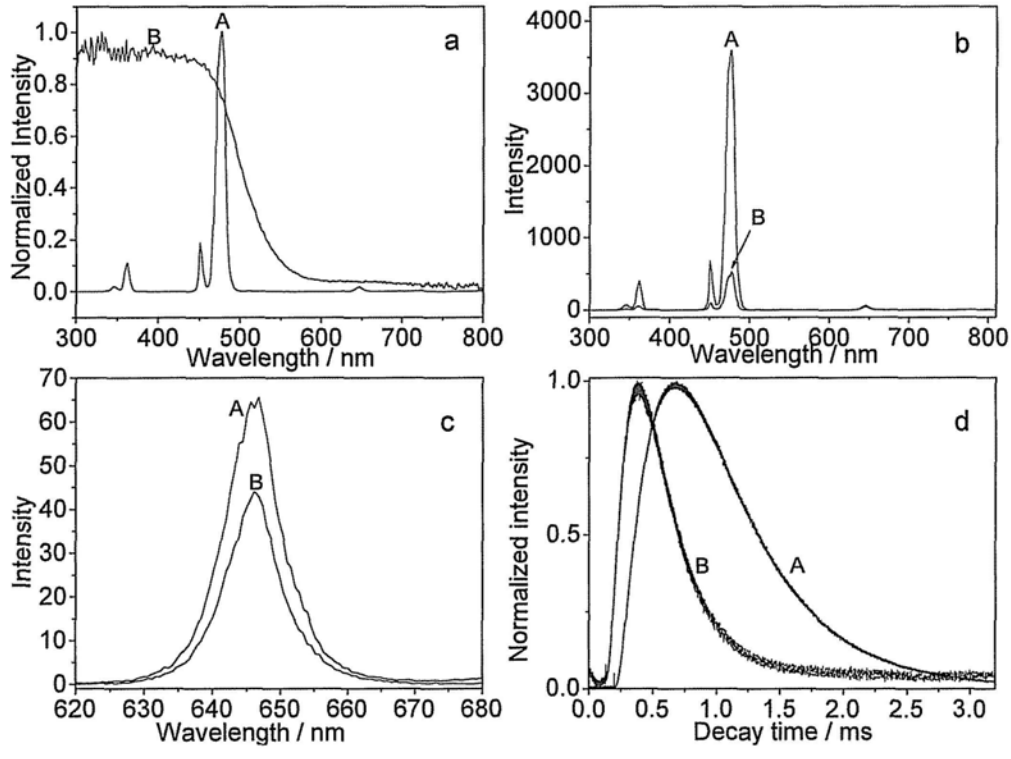

Figure 5.6 (a) (A)-Upconversion emission spectrum of $NaYF_4$: Yb,Tm and (B)-absorption spectrum of CdS. (b, c) Upconversion emission spectra of (A)-$NaYF_4$: Yb,Tm and (B)-$NaYF_4$: Yb,Tm/CdS. (c) is the magnified spectrum of (b). (d) Time-resolved fluorescence decay curves of Tm^{3+} (λ_{em}= 476 nm) of (A)-$NaYF_4$: Yb,Tm and (B)-$NaYF_4$: Yb,Tm/CdS. All the upconversion emission spectra were recorded upon 976 nm NIR excitation.

5.3.4 OH free radical monitoring

Photocatalysis generates hydroxyl radicals which are responsible for the degradation of pollutant molecules. Herein we applied a universally used method, photoluminescence technique[48-50], to monitor the formation of hydroxyl radicals upon NIR irradiation on the $NaYF_4$: Yb,Tm/CdS composite. Terephthalic acid is a traditional fluorescent probe[48-50]. As shown in Figure 5.7a, the nonfluorescent terephthalic acid captures hydroxyl radicals to produce the highly fluorescent 2-hydroxyterephthalic acid with an emission peak at 420nm upon excitation wavelength of 320nm. Therefore, hydroxyl radicals can be monitored by the fluorescence intensity changes. The measurement results are shown in Figure 5.7b. The fluorescence intensity increases nearly linearly with irradiation time, which is similar to the previous observation[48-50]. This is a clear indication of OH radicals formation. For comparison, we carried out the control experiments involving pure CdS or $NaYF_4$: Yb,Tm. No capability of producing OH radicals is observed from Figure 5.7c. And the amount of generated OH radicals is also dependent on the concentration of photocatalyst.

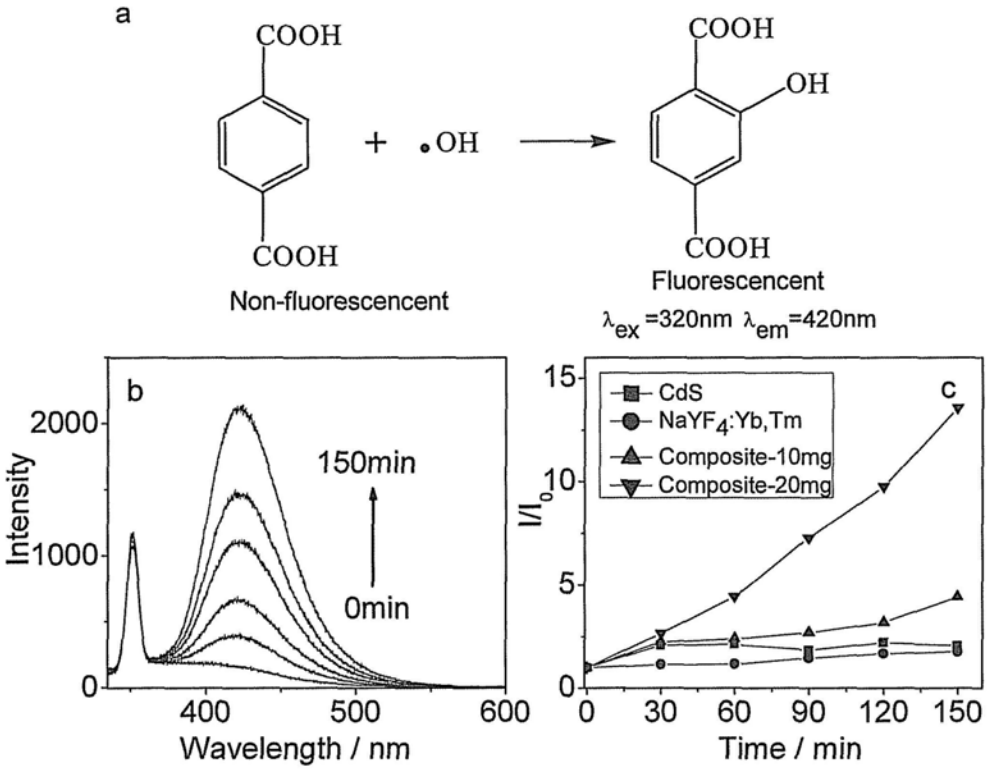

Figure 5.7 (a) Reaction between the formed OH radicals and probe molecules, terephthalic acid. (b) Time-dependent fluorescence spectra of the terephthalic acid solution ($4*10^{-4}$M) containing 20 mg of $NaYF_4$: Yb,Tm/CdS composite upon NIR irradiation. (c) Fluorescence intensity of the emission peak at 420nm as a function of NIR irradiation time.

5.3.5 Photocatalytic properties

The NIR-driven photocatalytic activity of the $NaYF_4$: Yb,Tm/CdS composite was measured by the degradation of Rhodamine B in an aqueous solution. Prior to the photoirradiation, all the samples were suspended in the Rhodamine B aqueous solution for one day to establish the adsorption/desorption equilibrium of dye on the sample surface, then pretreated with NIR for one hour. It can be seen from Figure 5.8a that the absorbance of Rhodamine B gradually decreases with the NIR irradiation, suggesting the occurrence of photocatalysis. In the control experiments, no photocatalytic activity could be observed as shown in Figure 5.8b. To further demonstrate the photoactivity, NIR driven photocatalytic degradation of methylene blue has also been performed as shown in Figure 5.8c and d. Since CdS is a good visible light photocatalyst, the composite also show high photoactivity under visible light (Figure 5.9).

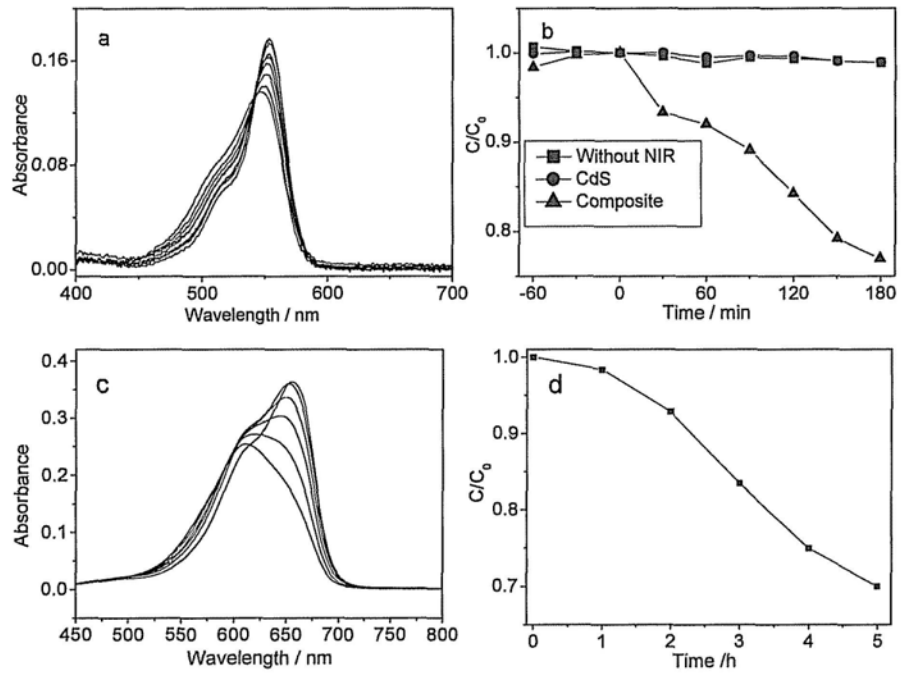

Figure 5.8 Time-dependent absorption spectra of Rhodamine B (a) and methylene blue (c) solution containing $NaYF_4$: Yb,Tm/CdS composite upon NIR irradiation. Rhodamine B (b) and methylene blue (d) reduction in UV-vis absorption spectra at 550 nm as a function of NIR irradiation time for different samples.

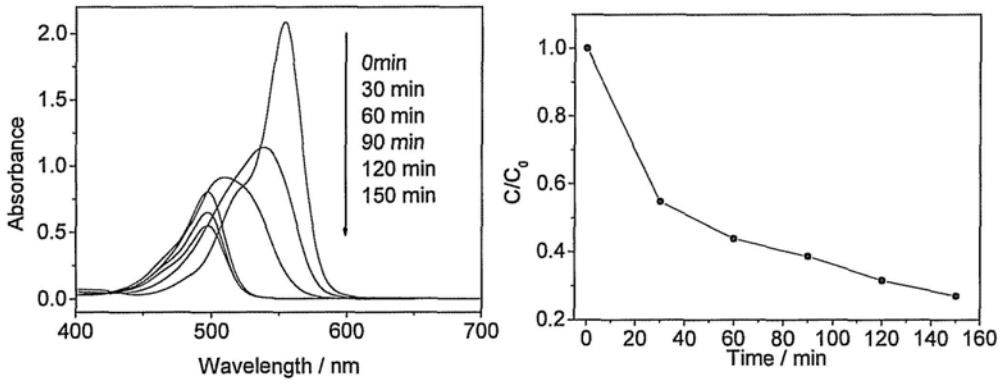

Figure 5.9 (a) Time-dependent absorption spectra of a 50 ppm Rhodamine B solution containing NaYF4: Yb, Tm/CdS composite upon visible-light irradiation. (b) Photocatalytic degradation of Rhodamine B as a function of visible-light irradiation time.

It has been reported that under strong UV or visible light irradiation CdS could be oxidized by photogenerated holes to release Cd^{2+} ions[51]. The photostability of the $NaYF_4$:Yb,Tm/CdS composite was investigated. The CdS nanoparticles were intact after exposing to NIR for three hours (Figure 5.10). The concentration of Cd^{2+} ions in the solution was also measured by ICP-AES before and after photocatalysis. As shown in Table 5.1, there is no evident increase of Cd^{2+} ions after photocatalysis. The good photostability is not surprising because of the very mild visible-light intensity in this NIR-induced system. Moreover, the modification with thioglycolic acid could provide a protective effect [49, 52, 53].

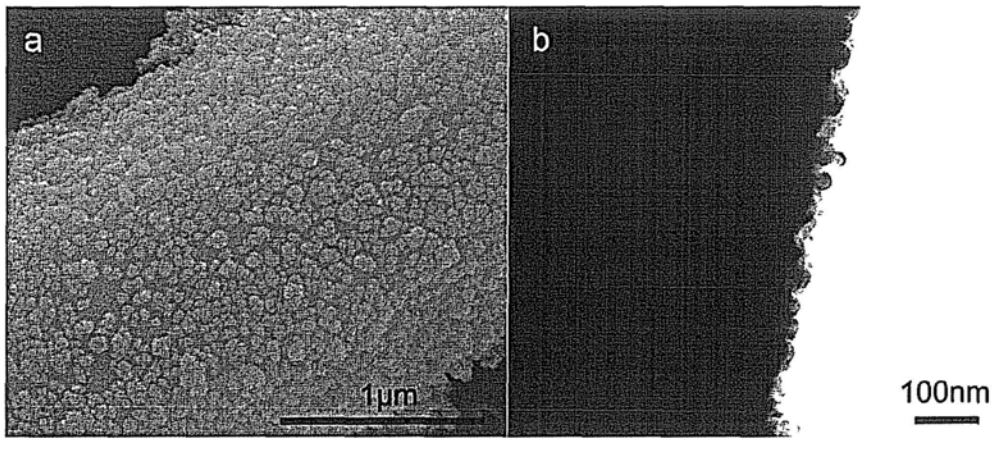

Figure 5.10 SEM (a) and TEM (b) images of the $NaYF_4$: Yb,Tm/CdS composite after NIR photocatalysis (3h)

	Concentration/ppm	Peak intensity
Standard solutions	0.5	11512.3
	1	27454.3
	2	59924.6
	4	120968.5
Before photocatalysis	2.80	83993.7
After photocatalysis	3.23	97636.2

Table 5.1 ICP measurements of the standard solutions and the sample solutions before and after NIR photocatalysis.

5.3.6 Mechanism

The mechanism for the NIR driven-photocatalysis is shown in Figure 5.11. The absorption of pump photons populates the $^2F_{5/2}$ level in Yb^{3+}. A Tm^{3+} ion is excited to the $^3H_5$ level by the energy transferred from the excited Yb^{3+}, and then relaxes nonradiatively to the $^3F_4$ level. Energy transfer from another Yb^{3+} ion to the Tm^{3+} causes the formation of a $^3F_2$ level. Subsequently, the Tm^{3+} relaxes to the $^3H_4$ level and then is excited to the $^1G_4$ level by absorbing energy from another excited Yb^{3+}. The sequential energy absorption from two excited Yb^{3+} ions promotes Tm^{3+} to $^1D_2$ and $^3P_2$. Then the excited Tm^{3+} ions fall to lower energy levels. $^1D_2 \rightarrow {}^3F_4$, $^1G_4 \rightarrow {}^3H_6$, $^3P_0 \rightarrow {}^3F_4$, $^1D_2 \rightarrow {}^3H_6$ and $^1G_4 \rightarrow {}^3F_4$ transitions produce the blue emissions at 450 nm, 470 nm, UV emissions at 350 nm, 361 nm and red

emission at 645 nm, respectively[42-46]. Here the $^1G_4$ level is the predominant excited state in this material as suggested by the strongest blue emission. For CdS[54], the energy gap from valence band (VB) to conduction band (CB) is about 2.5eV which is lower than the emitted blue and UV photon energy. As well known, semiconductors could be excited by the photons with an energy equivalent to or higher than the band gap energy, which causes the formation of photoelectrons and holes. According to the SEM images, $NaYF_4$: Yb,Tm and CdS are very close to each other. These allow energy transfer from $NaYF_4$: Yb,Tm to CdS. Then the excited CdS triggers photocatalysis.

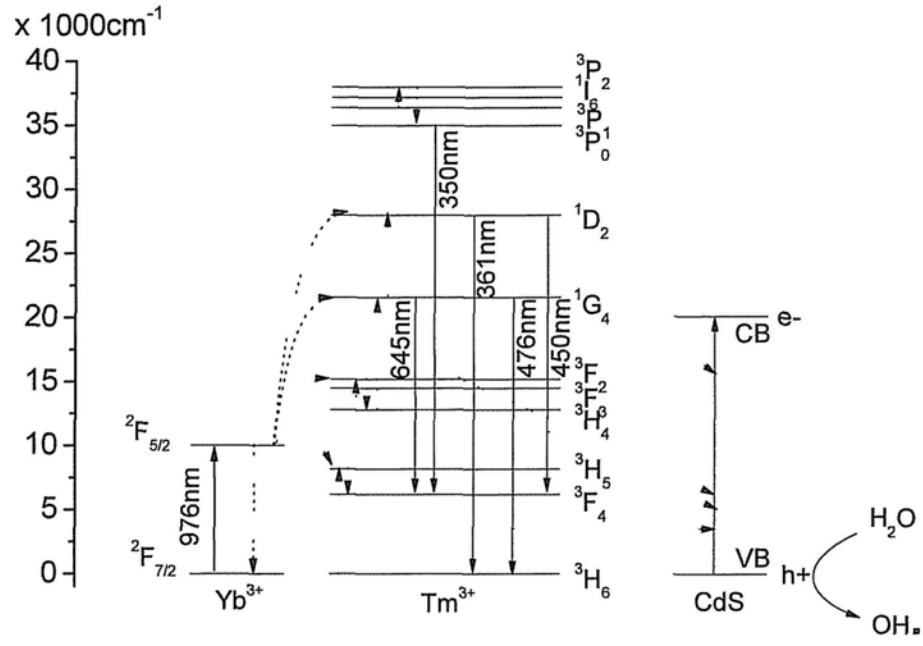

Figure 5.11 Schematic illustration of energy transfer mechanism from $NaYF_4$: Yb,Tm to CdS upon 976 nm NIR irradiation.

5.4 Conclusions

In summary, we have explored a simple, efficient method to synthesize a novel NIR photocatalyst, the $NaYF_4$: Yb,Tm/CdS composite. The morphology and composition of the resulting photocatalyst were investigated. The energy transfer from $NaYF_4$: Yb,Tm to CdS upon NIR irradiation was confirmed. The NIR-driven photocatalysis was realized by degrading Rhodamine B and methylene blue. This study suggests a promising system to study NIR photocatalysis, which may have profound implication on the future utilization of solar energy.

5. 5 References

[1] Fox, M. A.; Dulay, M. T. *Chem. Rev.*, **1993**, *93*, 341.

[2] Fujishima, A.; Honda, K. *Nature*, **1972**, *238*, 37.

[3] Hoffmann, M. R.; Martin, S. T.; Choi, W. Y.; Bahnemann, D. W. *Chem. Rev.*, **1995**, *95*, 69.

[4] Chen, Y.; Dionysiou, D. D. *Appl. Catal., B*, **2006**, *69*, 24.

[5] Guillard, C.; Beaugiraud, B.; Dutriez, C.; Herrmann, J.-M.; Jaffrezic, H.; Jaffrezic-Renault, N.; Lacroix, M. *Appl. Catal., B*, **2002**, *39*, 331.

[6] Lin, H.; Huang, C. P.; Li, W.; Ni, C.; Shah, S. I.; Tseng, Y.-H. *Appl. Catal., B*, **2006**, *68*, 1.

[7] Yamazoe, S.; Hitomi, Y.; Shishido, T.; Tanaka, T. *Appl. Catal., B*, **2008**, *82*, 67.

[8] Chen, X.; Mao, S. S. *Chem. Rev.*, **2007**, *107*, 2891.

[9] Ishibai, Y.; Sato, J.; Nishikawa, T.; Miyagishi, S. *Appl. Catal., B*, **2008**, *79*, 117.

[10] Yang, X.; Cao, C.; Erickson, L.; Hohn, K.; Maghirang, R.; Klabunde, K. *Appl. Catal., B*, **2009**, *91*, 657.

[11] Iliev, V.; Tomova, D.; Bilyarska, L.; Eliyas, A.; Petrov, L. *Appl. Catal., B*, **2006**, *63*, 266.

[12] Kim, T. W.; Hur, S. G.; Hwang, S. J.; Park, H.; Choi, W.; Choy, J. H. *Adv. Funct. Mater.*, **2007**, *17*, 307.

[13] Park, Y.; Kim, W.; Park, H.; Tachikawa, T.; Majima, T.; Choi, W. *Appl. Catal., B*, **2009**, *91*, 355.

[14] Higashimoto, S.; Azuma, M. *Appl. Catal., B*, **2009**, *89*, 557.

[15] Ho, W.; Yu, J. C.; Lee, S. *Chem. Commun.*, **2006**, 1115.

[16] Yu, J. C.; Ho, W. K.; Yu, J. G.; Yip, H.; Wong, P. K.; Zhao, J. C. *Environ. Sci. Technol.*, **2005**, *39*, 1175.

[17] Huang, Y. Y.; Sun, F. Q.; Wang, H. J.; He, Y.; Li, L. S.; Huang, Z. X.; Wu, Q. S.; Yu, J. C. *J. Mater. Chem.*, **2009**, *19*, 6901.

[18] Radhakrishnan, C.; Lo, M. K. F.; Warrier, M. V.; Garcia-Garibay, M. A.; Monbouquette, H. G. *Langmuir*, **2006**, *22*, 5018.

[19] Sayama, K.; Hayashi, H.; Arai, T.; Yanagida, M.; Gunji, T.; Sugihara, H. *Appl. Catal., B*, **2010**, *94*, 150.

[20] Morales, W.; Cason, M.; Aina, O.; de Tacconi, N. R.; Rajeshwar, K. *J. Am. Chem. Soc.*, **2008**, *130*, 6318.

[21] Li, G. S.; Zhang, D. Q.; Yu, J. C. *Chem. Mater.*, **2008**, *20*, 3983.

[22] Zhao, X.; Xu, T.; Yao, W.; Zhang, C.; Zhu, Y. *Appl. Catal., B*, **2007**, *72*, 92.

[23] Wang, X. C.; Maeda, K.; Thomas, A.; Takanabe, K.; Xin, G.; Carlsson, J. M.; Domen, K.; Antonietti, M. *Nat. Mater*, **2009**, *8*, 76.

[24] Bai, J.; Li, J.; Liu, Y.; Zhou, B.; Cai, W. *Appl. Catal., B*, **2010**, *95*, 408.

[25] Li, G. S.; Zhang, D. Q.; Yu, J. C. *Environ. Sci. Technol.*, **2009**, *43*, 7079.

[26] Qin, W. P.; Zhang, D. S.; Zhao, D.; Wang, L. L.; Zheng, K. Z. *Chem. Commun.*, **2010**, 2304.

[27] Heer, S.; Kompe, K.; Gudel, H. U.; Haase, M. *Adv. Mater.*, **2004**, *16*, 2102.

[28] Il Park, Y.; Kim, J. H.; Lee, K. T.; Jeon, K. S.; Bin Na, H.; Yu, J. H.; Kim, H. M.; Lee, N.; Choi, S. H.; Baik, S. I.; Kim, H.; Park, S. P.; Park, B. J.; Kim, Y. W.; Lee, S. H.; Yoon, S. Y.; Song, I. C.; Moon, W. K.; Suh, Y. D.; Hyeon, T. *Adv. Mater.*, **2009**, *21*, 4467.

[29] Budijono, S. J.; Shan, J. N.; Yao, N.; Miura, Y.; Hoye, T.; Austin, R. H.; Ju, Y. G.; Prud'homme, R. K. *Chem. Mater.*, **2010**, *22*, 311.

[30] Kramer, K. W.; Biner, D.; Frei, G.; Gudel, H. U.; Hehlen, M. P.; Luthi, S. R. *Chem. Mater.*, **2004**, *16*, 1244.

[31] Wei, Y.; Lu, F. Q.; Zhang, X. R.; Chen, D. P. *Chem. Mater.*, **2006**, *18*, 5733.

[32] Auzel, F. *Chem. Rev.*, **2004**, *104*, 139.

[33] Sun, Y. J.; Chen, Y.; Tian, L. J.; Yu, Y.; Kong, X. G.; Zhao, J. W.; Zhang, H. *Nanotechnology*, **2007**, *18*, 275609.

[34] Lin, G. F.; Zheng, J. W.; Xu, R. *J. Phys. Chem. C*, **2008**, *112*, 7363.

[35] Zhai, T. Y.; Fang, X. S.; Bando, Y.; Dierre, B.; Liu, B. D.; Zeng, H. B.; Xu, X. J.; Huang, Y.; Yuan, X. L.; Sekiguchi, T.; Golberg, D. *Adv. Funct. Mater.*, **2009**, *19*, 2423.

[36] Lin, Y. F.; Song, J.; Ding, Y.; Lu, S. Y.; Wang, Z. L. *Adv. Mater.*, **2008**, *20*, 3127.

[37] Shan, J. N.; Ju, Y. G. *Nanotechnology*, **2009**, *20*, 275603.

[38] Kameta, N.; Masuda, M.; Minamikawa, H.; Mishima, Y.; Yamashita, I.; Shimizu, T. *Chem. Mater.*, **2007**, *19*, 3553.

[39] Oar, M. A.; Serin, J. A.; Dichtel, W. R.; Frechet, J. M. J. *Chem. Mater.*, **2005**, *17*, 2267.

[40] Boulon, G.; Collombet, A.; Brenier, A.; Cohen-Adad, M. T.; Yoshikawa, A.; Lebbou, K.; Lee, J. H.; Fukuda, T. *Adv. Funct. Mater.*, **2001**, *11*, 263.

[41] Martin-Rodriguez, R.; Valiente, R.; Polizzi, S.; Bettinelli, M.; Speghini, A.; Piccinelli, F. *J. Phys. Chem. C*, **2009**, *113*, 12195.

[42] Yi, G. S.; Chow, G. M. *Adv. Funct. Mater.*, **2006**, *16*, 2324.

[43] Wang, L. Y.; Li, Y. D. *Chem. Mater.*, **2007**, *19*, 727.

[44] Zhang, F.; Shi, Y. F.; Sun, X. H.; Zhao, D. Y.; Stucky, G. D. *Chem. Mater.*, **2009**, *21*, 5237.

[45] Yang, J.; Zhang, C. M.; Peng, C.; Li, C. X.; Wang, L. L.; Chai, R. T.; Lin, J. *Chem. Eur. J.*, **2009**, *15*, 4649.

[46] Li, Z. Q.; Zhang, Y. *Nanotechnology*, **2008**, *19*, 345606.

[47] Lu, H.; Schops, O.; Woggon, U.; Niemeyer, C. M. *J. Am. Chem. Soc.*, **2008**, *130*, 4815.

[48] Ishibashi, K.; Fujishima, A.; Watanabe, T.; Hashimoto, K. *Electrochem. Commun.*, **2000**, *2*, 207.

[49] Rajendran, V.; Lehnig, M.; Niemeyer, C. M. *J. Mater. Chem.*, **2009**, *19*, 6348.

[50] Bohne, C.; Faulhaber, K.; Giese, B.; Hafner, A.; Hofmann, A.; Ihmels, H.; Kohler, A. K.; Pera, S.; Schneider, F.; Sheepwash, M. A. L. *J. Am. Chem. Soc.*, **2005**, *127*, 76.

[51] Meissner, D.; Memming, R.; Kastening, B. *J. Phys. Chem.*, **1988**, *92*, 3476.

[52] Rajh, T.; Ostafin, A. E.; Micic, O. I.; Tiede, D. M.; Thurnauer, M. C. *J. Phys. Chem.*, **1996**, *100*, 4538.

[53] Bae, W.; Mehra, R. K. *J. Inorg. Biochem.*, **1998**, *70*, 125.

[54] Little, R. B.; El-Sayed, M. A.; Bryant, G. W.; Burke, S. *J. Chem. Phys.*, **2001**, *114*, 1813.

Chapter Six

Conclusions

In this thesis, visible light photocatalysis was studied in the first two chapters. Then the preparation and applications of upconversion materials in NIR photocatalysis was discussed.

The enhancement of TNAs-based visible light photocatalytic activity was realized by the incorporating CdS and gold nanoparticles. The mechanism is discussed. It is due to the enhanced light absorption ability of CdS caused by the electromagnetic field enhancement effect of gold nanoparticles.

Then a novel visible light photocatalyst composed of Cu_2ZnSnS_4 and TiO_2 was prepared. As a small band gap semiconductor, Cu_2ZnSnS_4 could efficiently absorb visible light. After excitation, the photogenerated electrons in the conduction bands of Cu_2ZnSnS_4 were injected into those of TiO_2. Thus the composite exhibited high photocatalytic activity under visible light irradiation.

Due to the unique optical property to convert NIR to visible light, upconversion materials show great potential in NIR photocatalysis. Firstly, the preparation of upconversion materials was studied. A facile self-assembly method to prepare nanoporous $NaYF_4$:Yb,Er upconversion single crystals was developed. And the upconversion optical properties were investigated. Then several potentials of the porous upconversion materials were proposed.

Then NIR photocatalysis was demonstrated by using $NaYF_4$: Yb, Tm/CdS composite. $NaYF_4$: Yb,Tm/CdS composite was prepared by a surface modification method. Energy transfer from $NaYF_4$: Yb,Tm to CdS was confirmed by the upconversion and fluorescence decay properties. Then NIR-driven photocatalysis was investigated by degrading Rhodamine B and methylene blue. A mechanism for NIR-driven photocatalysis was proposed.

List of Publications

[1] **C. H. Li**, F. Wang, J. A. Zhu, J. C. Yu "$NaYF_4$: Yb,Tm/CdS composite as a novel near-infrared-driven photocatalyst", *Appl. Catal., B*, **2010**, *100*, 433.

[2] **C. H. Li**, X. F. Yang, J. C. Yu, T. A. Ming, J. F. Wang "Porous upconversion materials-assisted near infrared energy harvesting by chlorophylls", *Chem. Commun.*, **2011**, *47*, 3511.

[3] **C. H. Li**, F. Wang, J. C. Yu "Semiconductor/biomolecular composites for solar energy applications", *Energy Environ. Sci.*, **2011**, *4*, 100.

[4] **C. H. Li**, F. Wang, L. Zhang, Y. C. Li "Synthesis, Characterization and Potential Applications of Porous Upconversion Materials", *J. Mater. Chem.* Invited Paper

[5] **C. H. Li**, Y. H. Shen, A. J. Xie, J. A. Wang, Q. F. Zhang, S. K. Li "A novel method to realize the transition from silver nanowires to nanoplates based on the degradation of DNA", *J. Nanopart. Res.*, **2010**, *12*, 2679.

[6] F. Wang, **C. H. Li**, L. D. Sun, H. S. Wu, T. A. Ming, J. F. Wang, J. C. Yu, C. H. Yan "Heteroepitaxial Growth of High-Index-Faceted Palladium Nanoshells and Their Catalytic Performance", *J. Am. Chem. Soc.*, **2011**, *133*, 1106.